Een optische studie van verdampende brandstofverstuivingen
voor middelsnellopende motoren

An Optical Study of Evaporating Fuel Sprays for Medium Speed Engines

Roel Verschaeren

Promotoren: prof. dr. ir. S. Verhelst, ing. K. Christianen
Proefschrift ingediend tot het behalen van de graad van
Doctor in de ingenieurswetenschappen: werktuigkunde-elektrotechniek

UNIVERSITEIT
GENT

Vakgroep Mechanica van Stroming, Warmte en Verbranding
Voorzitter: prof. dr. ir. P. De Baets
Faculteit Ingenieurswetenschappen en Architectuur
Academiejaar 2018 - 2019

ISBN 978-94-6355-233-2
NUR 977, 969
Wettelijk depot: D/2019/10.500/41

Supervisors

Prof. Sebastian Verhelst - Ghent University
Ing. Koen Christianen - Anglo Belgian Corporation

Members of the examination board

Chairman:
Prof. Filip de Turck - Ghent University

Reading committee:
Prof. Öivind Andersson - Lund University
Prof. Rik Baert - Fontys Hogeschool Automotive
Dr. Louis Sileghem - Ghent University
Prof. Marc Vantorre - Ghent University

Dankwoord

Om dit boek af te werken heb ik kunnen rekenen op morele en praktische steun van een heleboel mensen die ik hier nog eens wil bedanken.

Ik had het geluk om zowel voor de universiteit Gent als voor Anglo Belgian Corporation te werken, een ideale balans van aan de universiteit in detail een probleem te kunnen onderzoeken en bij ABC een realiteit waarbij op eerder korte termijn goede oplossingen moeten gevonden worden.

Prof. Sebastian Verhelst en Ir. Lieven Vervaeke wil ik bedanken om mij, een computerwetenschapper, te vertrouwen in mijn wens om een andere richting in te slaan. Door dit vertrouwen hebben jullie het mogelijk gemaakt om een deel van mijn professionele dromen te realiseren. Ook Koen Christianen wil ik bedanken om de taak van Lieven in het midden van het project over te nemen. Hoewel hij het project niet gestart had, heeft hij er mee voor gezorgd dat ik me gewaardeerd voelde bij ABC.

De collega's bij ABC wil ik danken voor hun hartelijke ontvangst, elke keer wanneer ik binnenkwam. Bedankt voor jullie professionele metingen, die onmisbaar waren voor de validatie van de motorsimulatiecode. Uiteraard moet ik ook iedereen bedanken die met onze persoonlijke koffiezet, koffie heeft gezet.

De collega's van de universiteit wil ik bedanken voor hun steun wanneer er een experiment misging. Ik kon mijn frustraties delen en het betekende veel om dit te kunnen vertellen en dat er geluisterd werd.

Als special guest in dit dankwoord, wil ik graag Jan Van de Vyver bedanken. Jij zorgde mee voor de nodige inspanning. Naast jouw doctoraat heb je waarschijnlijk de helft van mijn voormalig appartement en huis gebouwd, anders had ik het einde niet gehaald. Ik hoop dat ik mijn 'schuld' binnenkort mag komen aflossen.

Als laatste wil ik graag mijn vrouw en kindjes: Jelleke, Amber, Linde en Korneel bedanken. Vooral de laatste maanden heb ik met een pasgeboren Korneel toch meer en meer aan mijn doctoraat kunnen schrijven en dat komt vooral omdat Jelleke zoveel voor de kindjes heeft gezorgd. Als ik thuis kwam kreeg ik een liefdevolle knuffel van Linde, en een zoen van Amber. Bedankt alle vier om verschillende moeilijke dagen ogenblikkelijk perfect te maken! Bedankt Jelleke, mijn liefje, om me zo te steunen!

Gent, mei 2019

Roel Verschaeren

Table of Contents

Nomenclature

Acronyms

AHRR apparent heat release rate

CFD computational fluid dynamics

CR common rail

ECN Engine Combustion Network

EGR exhaust gas recirculation

EOI end of injection

FWHM full width at half maximum

GUCCI Ghent University Combustion Chamber I

GUI graphical user interface

HC hydrocarbon

HRR heat release rate

IMO International Maritime Organization

IPCC Intergovernmental Panel on Climate Change

L/D length over diameter

LEL Lower Explosion Limit

LLNL Lawrence Livermore National Laboratory

LOC Limiting Oxygen Concentration

LTC low temperature combustion

NO$_x$ oxides of nitrogen

PID-controller proportional integral derivative controller

PLN pump line nozzle

PM particulate matter

PWM pulse width modulation

SO$_x$ oxides of sulfur

SOI start of injection

TDC top dead center

TPA Three Pressure Analysis

UEL Upper Explosion Limit

WHO World Health Organization

List of publications

Publications in peer reviewed international journals

Publications directly related to the Ph.D. manuscript

1. Verschaeren R, Verhelst S. (2018) Increasing exhaust temperature to enable after-treatment operation on a two-stage turbo-charged medium speed marine diesel engine. Energy. 147, 681-687

Other journal publications

1. Verschaeren, R., Schaepdryver, W., Serruys, T., Bastiaen, M., Vervaeke, L., Verhelst, S. (2014). Experimental study of NOx reduction on a medium speed heavy duty diesel engine by the application of EGR (exhaust gas recirculation) and Miller timing. Energy, 76, 614–621.

Related publications in proceedings of international conferences

1. Galle, J., Van De Maele, C., Defruyt, S., Verhelst, S., Verschaeren, R. (2013). Evaluation of some important boundary conditions for spray measurements in a constant volume combustion chamber. In: SAE 2013 World Congres, Detroit, MI, USA. SAE Technical Paper no. 2013-01-1610

2. Galle, Jonas, Verschaeren, R., Verhelst, S. (2015). The behavior of a simplified spray model for different diesel and Bio-Diesel surrogates. In: SAE 2015 World Congress, Detroit, MI, USA. SAE Technical Paper no. 2015-01-0950

3. Verschaeren, R., Verhelst, S., Vervaeke, L. (2014). Modeling of a heavy duty diesel engine to ease complex optimization decisions. Journées d'etudes of the Belgian Section of the combustion Institute, 2014.

Nederlandse samenvatting –Summary in Dutch–

Wetenschappers hebben aangetoond dat alleen broeikasgassen, uitgestoten door menselijk toedoen, met een hoge zekerheid een verklaring kunnen zijn voor de gemeten toenemende globale temperatuur. Op lange termijn zal een verdere toename van de temperatuur meer extreme weerfenomenen veroorzaken, zoals bijvoorbeeld hittegolven. Ook de regenval zal wijzigen, met grotere hoeveelheden regen op korte tijd met daartussen lange droge periodes, met overstromingen en droogtes tot gevolg. Onze maatschappij wordt zich meer bewust van het feit dat giftige stoffen die tijdens een verbrandingsproces ongewild vrijkomen een effect hebben op onze gezondheid. Dit zorgt ervoor dat de emissielimieten voor deze giftige stoffen strenger en strenger worden.

De verbrandingsmotor is vandaag verantwoordelijk voor een groot deel van de uitstoot van broeikasgassen en van giftige gassen en deze technologie is de meest belangrijke aandrijving voor transport op de weg en over water. Terwijl een structurele verandering de hoeveelheid personenvervoer gedeeltelijk zou kunnen verminderen of verplaatsen (bv. thuiswerk) geldt dit niet voor de scheepvaart, waar wordt verwacht dat de hoeveelheid verscheepte goederen alleen maar zal toenemen.

Alternatieve aandrijfsystemen, zonder verbrandingsmotor, worden ontwikkeld om de uitstoot van broeikasgassen en giftige gassen van de transportsector te verminderen maar deze systemen kunnen enkel werken wanneer er voldoende energie beschikbaar is. In veel landen is het onmogelijk om genoeg lokale hernieuwbare energie op te wekken om zo het totale energieverbruik van dat land af te dekken. Dit

wil zeggen dat sommige landen, ook in de verre toekomst, energie zullen moeten importeren. Dit kan bijvoorbeeld via een brandstof die hernieuwbaar geproduceerd wordt in een land waar hernieuwbare energie eenvoudiger toegankelijk is. Omdat huidige grote scheepsmotoren een hoog rendement hebben, zeer betrouwbaar zijn en omdat ze zeer flexibel verschillende brandstoffen kunnen verbranden zonder extra verlieslatende tussenstappen kan de verbrandingsmotor als technologie een duurzame oplossing zijn, op voorwaarde dat deze in de toekomst op een hernieuwbare brandstof draait.

De emissielimieten voor giftige stoffen die door motoren uitgestoten worden, dalen meer en meer om de luchtkwaliteit te verbeteren. Huidige limieten voor scheepsmotoren bereiken grenzen die kunnen vergeleken worden met de limieten voor wegtransport en het is een grote uitdaging om de scheepsmotoren aan deze limieten te laten voldoen. Scheepsmotoren verschillen immers grondig van motoren voor wegtransport, de cilinder is bijvoorbeeld veel groter, de verbranding duurt veel langer en het brandstofinjectiesysteem is veel groter en gebruikt oudere maar meer robuuste technologie omdat de betrouwbaarheid voor deze motoren zeer belangrijk is.

Om onder deze emissielimieten te blijven, werd een bestaande commercieel beschikbare motorsimulatiecode toegepast en gekalibreerd om de motor te optimaliseren. Er werd gevonden dat deze niet in staat was om de verbranding in de cilinder volledig juist te voorspellen: er bestaat een afwijking tussen lage en hoge motorbelastingen. Dit model wordt gebruikt om kleinere motoren te simuleren, en bijgevolg werden niet alle fysische processen correct gemodelleerd.

Om deze modellen te verbeteren, moet het verbrandingsproces voor scheepsmotoren onderzocht worden. Onderzoek op kleine motoren zorgt voor kennis over het verbrandingsproces in normale motorwerking. In de literatuur is niet beschreven hoe de verschillen tussen een scheepsmotor en een kleine motor het verbrandingsproces zouden kunnen beïnvloeden. Op dit moment is het voldoende om een normaal verbrandingsproces te gebruiken in een scheepsmotor om te voldoen aan huidige emissieregels, maar het is duidelijk dat in de toekomst een nieuwe technologie nodig zal zijn. Voor wegtransport worden nieuwe verbrandingsmethodes zoals lagetemperatuurverbranding onderzocht. Deze methode verdunt het lucht-brandstof mengsel, zodat de temperatuur tijdens de verbranding beperkt wordt. De limieten van het huidige brandstofinjectiesysteem in een scheepsmotor, wanneer die met een lagetemperatuurverbranding zou werken, zijn niet gekend.

Het onderzochte verbrandingsproces in een scheepsmotor start met vloeibare brandstof op hoge druk in het injectiesysteem. Deze brandstof wordt verneveld in de cilinder en door warmteoverdracht van het hete

gas in de cilinder naar de brandstof kan deze brandstof verdampen. Na enige vertraging, het ontstekingsuitstel, begint dan uiteindelijk de verbranding. Om dit proces te bestuderen voor het injectiesysteem van een scheepsmotor werd een optisch toegankelijke verbrandingskamer met een constant volume, de Ghent University Combustion Chamber I (GUCCI), verder ontwikkeld. De omgevingscondities van het gas in de kamer kunnen met de hulp van dit werk nauwkeurig en herhaalbaar ingesteld en gecontroleerd worden. Door de instelwaardes van de omgevingscondities te variëren kan het verstuivingsproces voor huidige en mogelijk nieuwe motorcondities bestudeerd worden.

Verschillende parameters van de verstuiving zijn via twee optische technieken met een hogesnelheidscamera opgenomen in de opstelling. De eerste techniek is de schlieren-techniek: die maakt het mogelijk om de dampvormige fase van de verstuiving te visualiseren. De tweede techniek wordt gebruik om de vloeibare fase zichtbaar te maken: de Mie-techniek. Voor elk experiment wordt een reeks afbeeldingen bewaard die met een software-programma verwerkt worden tot damp- en vloeistof-lengtes voor verschillende momenten na de start van de injectie.

Verschillende metingen werden uitgevoerd, waarbij de omgevingscondities gevarieerd werden voor twee verschillende injectoren. De dichtheid van het gasmengsel werd gevarieerd tussen $7.6\,\mathrm{kg/m^3}$ en $22.5\,\mathrm{kg/m^3}$, de temperatuur tussen $700\,\mathrm{K}$ en $1000\,\mathrm{K}$ en de zuurstofconcentratie tussen $21\,\%$ en $13\,\%$. Deze condities zijn representatief voor huidige motorcondities en voor een mogelijke lagetemperatuur-conditie met een hoge verdunningsfactor.

De damp- en vloeistof-lengtes werden dan vergeleken voor deze variërende omgevingscondities en de gevonden trends kwamen overeen met trends die beschreven zijn in de literatuur voor kleinere motoren, behalve voor de hoogste gasdichtheid. Daar was de gemeten vloeistoflengte hoger dan kon verwacht worden uit literatuur.

Om deze afwijkingen beter te begrijpen werd een 1-D simulatie-model voor de verstuiving, gebaseerd op literatuur, gebruikt. Om de berekeningen te vereenvoudigen waren verschillende veronderstellingen nodig die reeds werden gevalideerd voor kleinere motoren, maar nog niet voor het injectiesysteem van scheepsmotoren.

Met hulp van de resultaten van de optische metingen werd het simulatiemodel gevalideerd voor variërende omgevingscondities.

Een gevoeligheidsanalyse kon de oorzaak van de hoge vloeistoflengte identificeren als een combinatie van de volgende drie mogelijkheden: een onevenwicht tussen het opgelegde massadebiet en de snelheid aan de injectorgaatjes of een fysisch proces dat niet juist gemodelleerd werd.

Het injectiesysteem van een scheepsmotor beperkt de toepassing

van nieuwe verbrandingsmethodes dus niet fundamenteel door het injectieproces, maar eerder door een gebrek aan flexibiliteit. De injectietiming in grote motoren ligt typisch mechanisch vast en kan dus niet gewijzigd worden terwijl de motor draait. Van onderzoek op kleine motoren is bekend dat deze flexibiliteit nodig is om de verbranding te controleren bv. wanneer de buitentemperatuur wijzigt of tijdens een koude-start. Wanneer deze flexibiliteit toegevoegd wordt, zou het mogelijk zijn om met grote injectoren nieuwe verbrandingsmethodes toe te passen.

English summary

Scientists have shown that the human-caused emission of greenhouse gases is currently the only way to explain the measured global temperature increase with high certainty. An additional global temperature increase will, in the long term, result in more extreme weather such as heat waves, but also in shifted rainfall patterns causing droughts and floods. In the short term, pollutants, generated during a combustion process, have an adverse effect on human health and increasing public awareness causes the amount of allowed toxic emissions to become more and more regulated.

The internal combustion engine is currently responsible for a large fraction of the total emission of toxic products and greenhouse gases and it is the dominant technology to power the transportation sector in both road and marine applications. Structural changes could partially avoid or shift transport activities for road transport, but for shipping it is expected that demand will be growing.

While alternative propulsion systems, without internal combustion, are being developed to reduce the emission of both toxic and greenhouse gases of the transportation sector, a severe bottleneck for these alternatives appears: local renewable energy supply is not sufficient to provide for all local energy consumption. This means that, for several countries, energy still will have to be imported somehow in the long term, e.g. by a fuel that is produced in a renewable way on a remote location with abundant renewable energy. Because large marine engines currently have a high efficiency, are very reliable, and could use a variety of renewable fuels directly which avoids additional energy conversion losses, we believe that the internal combustion engine is a sustainable solution for the long term.

Maximum toxic emissions from a medium-speed marine engine are becoming more and more regulated to improve air quality, reaching levels on par with emission legislation for automotive engines. This poses significant challenges for marine engine design as marine engines differ from automotive engines in several ways: combustion chambers are much bigger, combustion duration is longer, injection technology differs and reliability is a much more important concern.

To remain below these and future emission limits, an existing commercial engine simulation code was applied to optimize the engine. It was found that it was unable to predict the combustion process perfectly. A deviation between low and high engine loads was observed. This model is used to simulated automotive engines. This causes a deviation in the modeling of the physical processes.

To improve these models, the combustion process should be studied for marine applications. Research on smaller engines results in a good knowledge of the conventional combustion process in automotive engines. It is not well documented in available literature how the specific differences between a marine engine and an automotive engine would cause a different combustion process. Currently, marine engines are still able to use a conventional combustion and comply with emission legislation, but it is clear that a new technology will need introduction in the future. New combustion strategies, such as low temperature combustion, are under investigation for automotive engines. These new combustion strategies typically rely on diluting the reacting mixture, in that way reducing the combustion temperature. The limits of the current injection system in a marine engine with regard to implementing a low temperature combustion strategy are unknown.

The combustion process starts with the liquid fuel in the injection system that is atomized into the combustion chamber. Heat transfer from the ambient gas to the fuel results in its evaporation and after a certain time, i.e. the ignition delay, fuel starts to react. To study this process an existing optically accessible constant volume combustion chamber, the Ghent University Combustion Chamber I (GUCCI), was further developed. It is now possible to vary the ambient conditions in a repeatable and accurate way to obtain specific ambient boundary conditions. This allows the study of the injection process in ambient conditions representative for current and possible future engine operation.

Two high speed optical measurement techniques were used on the combustion chamber to characterize the evaporation of the spray: a schlieren technique to visualize spray vapor boundaries and a Mie scattering technique to visualize liquid spray penetration. After obtaining a sequence of images a software algorithm was employed to detect spray vapor and liquid penetration.

A database of spray measurements was collected for a range of ambient boundary conditions for two different injectors. The effect of an ambient density and temperature variation on spray vapor and liquid penetration was studied within current and possible future boundary conditions. Ambient density was varied between 7.6 $\mathrm{kg/m^3}$ and 22.5 $\mathrm{kg/m^3}$, ambient temperature was varied between 700 K and 1000 K and finally oxygen concentration was varied between 21 % and 13 %.

These are representative for the ambient conditions for conventional combustion and for a possible low temperature combustion strategy in a marine engine.

The obtained vapor and liquid penetrations were compared for the different tested ambient conditions and trends equivalent to results for on-road applications were found for all but one ambient condition. Liquid penetration for the highest ambient density was higher than could be expected from available literature.

To better understand these differences, an in-house 1-D spray simulation model, based on literature, was employed to describe the spray penetration and evaporation process in more detail. To simplify the calculations, assumptions had to be made which were confirmed for on-road applications, but not yet for large marine applications.

This new simulation model was then validated with the spray measurement results for the ambient density and temperature variation. Simulated vapor and liquid penetration agreed well with measurements for an ambient temperature variation and for the low and medium ambient density. However, for the highest density, the steady state liquid penetration was too low.

A sensitivity analysis showed that the cause of this deviation could be attributed to a combination of three possibilities: an imbalance of the nozzle mass flow rate and the momentum flux or a physical process that is not yet captured in the model.

Finally, it is found that the marine injection system does not fundamentally limit obtaining a low temperature combustion strategy by the injection process, but rather by lack of flexibility. The injection timing of a marine injection system, employed in this work, is fixed mechanically over the whole operating range of the engine and cannot be adjusted during engine operation. From on-road applications it is known that this flexibility is necessary during low temperature combustion operation to control combustion timing continuously and account for ambient temperature variations or during a cold-start of the engine. Once the flexibility of a marine injection system can be improved, it would be possible to try implementing new combustion schemes on these large engines.

1

Death of the Internal Combustion Engine?

"If you can't explain it to a six year old, you don't understand it yourself."

- Albert Einstein -

1.1 Everything electric?

The large and growing human population has an ever increasing influence on its living areas. Only one or two generations are left to avoid extreme effects of global warming on human life. Global warming is caused by the emission of *greenhouse gases*, mainly related to energy conversion, e.g. domestic heating, transportation, ….

Another, but related problem, is the quality of the air that we all breathe. Energy conversion processes typically require combustion to extract chemical energy and provide useful work. *Toxic products* originate from incomplete combustion, e.g. hydrocarbon (HC), CO and particulate matter (PM) or from unwanted oxidation such as oxides of nitrogen (NO_x). People become increasingly aware that these toxic emissions influence their health.

In this section, the global warming problem is described and uncoupled from air quality where necessary. This PhD work focuses on the transportation sector and for this sector the effect on energy consumption by a complete conversion to electric mobility is then evaluated.

1.1.1 Global warming

Human-induced global warming in 2018 reached approximately $(1.0 \pm 0.2)\,°C$ above pre-industrial levels according to the Intergovernmental Panel on Climate Change (IPCC) [1]: this organization of the United Nations consists out of hundreds of experts over the world who provide a scientific view of climate change and its impact on nature, society and economy. Currently, global warming is found to continue at a pace of $(0.2 \pm 0.1)\,°C$ per decade.

Global warming will shift rainfall patterns, cause rising sea levels, increase ocean acidity and increase the occurence of extreme events such as floods, droughts and heat waves [1]. To avoid an extreme change, that would make our world a difficult place to live in, global warming should be limited.

A strong correlation of cumulative CO_2 emission and global surface temperature change is found in [2] where information was compiled from several scientific works. Substantial anthropogenic CO_2 emission reduction, to net zero, is necessary to avoid further global warming. The remaining carbon budget is defined as the total cumulative emission of CO_2 from today until the time of zero global emission for global warming to remain within a certain limit.

The remaining budget is currently (2018) about 420 Gt CO_2 for a two-thirds chance of limiting warming to 1.5 °C, while the total amount of

emitted CO_2 in 2017 was around (42 ± 3) Gt per year. At the current pace, ten years are left to reach net zero CO_2 emission.

Transport accounted for 28 % of global final energy demand in 2014 and 92 % of this transportation energy demand is met by oil products [3]. CO_2 emission reduction of the transport sector can be achieved by several means: by technology such as energy efficiency improvements and/or fuel switching or by structural changes that avoid or shift transport activities. While the latter can be important for light-duty vehicles, it is expected that demand growth of shipping and aviation is going to be higher than for light-duty applications, which limits the possibilities to avoid transportation [3].

1.1.2 Air quality

Global warming and air quality are a different issue. Currently, they are both caused by combustion of fuels, but it is important to uncouple these from each other. The most important greenhouse gas, CO_2, is harmless for human health in its current concentration. On the other hand, other pollutants are generated during combustion with an effect on human health that depends on the exposure duration and concentration.

Some pollutants are both toxic, as will be described further below, and contribute to global warming. E.g. black carbon is emitted in a variety of combustion processes. It influences cloud processes, absorbs solar radiation and alters the melting of snow and ice. Black carbon is found to be the second most important climate-warming agent in [4], with CO_2 the most important one. Reducing black carbon can thus both improve air quality and slow global warming.

Parallel to the IPCC, which studies global warming, the World Health Organization (WHO) works on air pollution and its effect on health: it claims air pollution is currently the single largest environmental risk to human health globally. It estimates that more than six million premature deaths were caused by air pollution in 2012 [5]. The burden and associated costs of diseases due to bad air quality is increasingly being recognized by governments as a major public health concern.

Air quality guidelines are developed by the WHO to help policy makers setting standards and goals for air quality management. These guidelines provide evidence-based recommendations to protect global population from adverse health effects. The difference between guidelines and standards is strongly emphasized in their reports, it is up to local authorities to consider economic, social and cultural factors when using the guidelines for setting standards.

1.1.3 A possible path to zero fossil fuels

Current public opinion seems biased towards a complete electric solution as a transportation system, powered by renewable electricity alone. However, roadmap studies from oil companies and governmental and intergovernmental organizations show a vastly different scenario: a large fraction of the required energy will still be provided by fossil sources in the future (U.S. Energy Information Administration [7], the International Energy Agency [3], Statoil [8], BP [6]). A renewable transition could happen faster with more demanding and challenging policy (e.g. efforts to limit global warming to 1.5 °C) but even then oil, coal and gas will remain important up to at least 2050 [8], possibly with carbon capture and storage to limit net carbon emission.

Even with a more challenging policy, some practical problems arise, inherent to electrification. Technology can still vastly improve energy efficiency of transportation and when electricity is generated efficiently, electrifying vehicles can be such an example. Electric motors convert between 90 and 95 % of the input energy into useful work, while the efficiency of an internal combustion engine is limited to about 47 % [9]. Of course, only considering this last energy conversion step is an unacceptable simplification of reality. An electric vehicle is more efficient but it requires a higher valued energy source.

A calculation example helps to explain the emerging difficulties: Belgian personal transportation resulted in 84.1×10^9 km driven in 2017 [10]. When the Belgian fleet would be completely electrified and by assuming

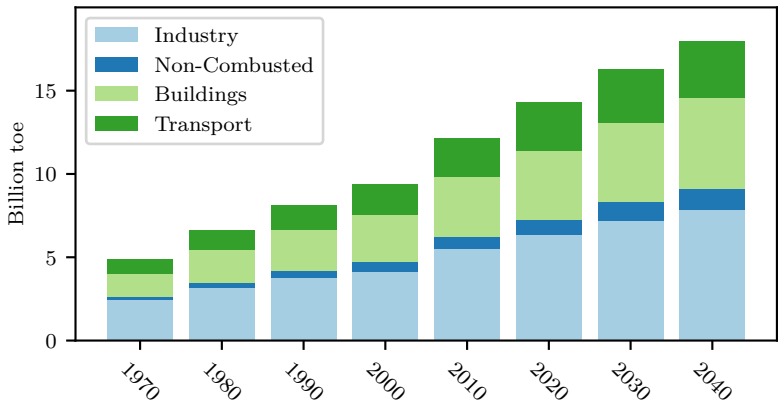

Figure 1.1: Predicted energy end use according to BP [6] under business as usual energy transition.

an average energy consumption of an electric vehicle of 0.2 kW h/km [11] an additional electricity consumption of

$$84.1 \times 10^9 \,\text{km} \times 0.2 \,\frac{\text{kW h}}{\text{km}} = 16\,820 \,\text{GWh}$$

results.

To put this into perspective: this approximately requires two additional nuclear power plants of 1000 MW, or more than 300 windmills added (assuming they continuously run full load) in the North Sea on the Thornton bank where currently 54 windmills are operational. This order of magnitude calculation neglects that we also need to reduce carbon emissions of the rest of the electricity production capacity, that industry still needs fuels and that heating buildings will also still require energy (illustrated in Figure 1.1).

All consumption and renewable energy sources considered, it is unlikely that direct generation of Belgian energy needs is possible by local renewable sources. This is partially caused by a high population density and low available area, but the same was observed from an analysis of the complete energy landscape for the United Kingdom [12].

To close the energy balance on the grid, gas or liquid fueled power plants can be employed, but this reduces the efficiency of an electric vehicle by the efficiency of the power plant. Furthermore, a seasonal imbalance exists: energy demand for heating increases in winter while typically there is a limited availability of renewable energy. On the other hand, in summer, plenty of renewable energy is available but heating demand is lower.

A possible view on energy for transportation is shown in Figure 1.2. The electric grid is shown centrally, with current energy flows from fossil and nuclear power plants currently providing the bulk of the energy (black dashed lines). A possible and technically feasible scenario is shown with green thick arrows to denote a strong increase in capacity. A strong increase in renewable capacity (wind and solar) provides energy for transportation, but because of limited energy availability in winter and because other sectors require energy as well, fuel will still need to be imported. In summer, excess electricity could be converted into a long term storage fuel. A hybrid fleet can directly use liquid fuel when renewable electricity production is limited.

It has to be acknowledged though that renewable energy will, at least partially, have to be imported even when massive investments are done in local renewable energy production. This is indicated by the thin green arrow from electricity to liquid fuels and a thick arrow directly back to the hybrid fleet in Figure 1.2. To finally reduce total CO_2 emission,

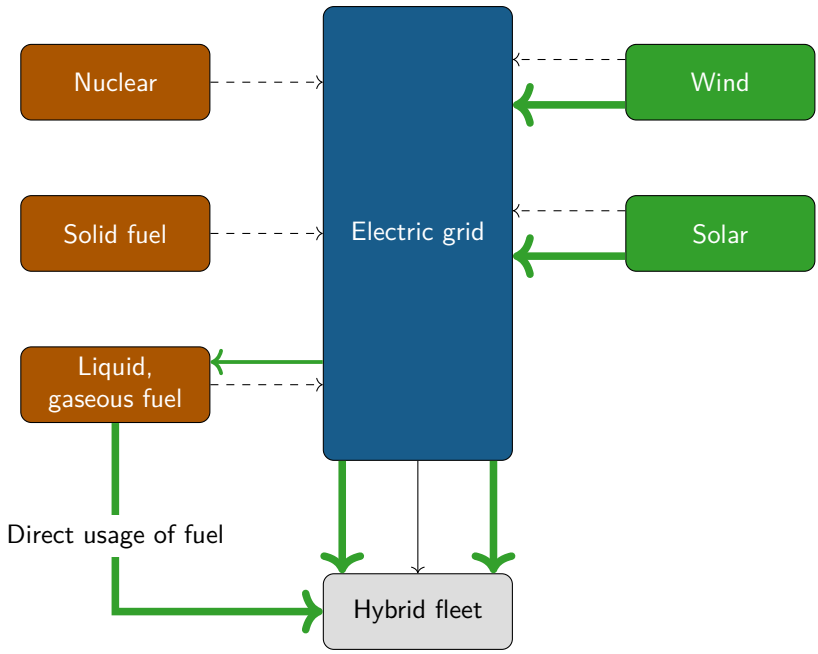

Figure 1.2: A possible view on the energy landscape in 2050*, applied on transportation: business as usual indicated with dashed lines. Electrification requires additional production capacity: an ideal scenario is shown with green thick arrows meaning a strong increase in energy flow compared to the past. To solve seasonal variation in energy demand, some conversion to long term storage (e.g. liquid fuel) is added.*

liquid fuels can be gradually replaced by less carbon intensive fuels [13]. Alcohol fuels are an example of this [14], given that they are produced in a renewable way.

1.2 Marine versus road transport

Transportation over water is energy efficient because of two reasons: engine efficiency is higher, e.g. 54.96% for the MAN engines in the Maersk Triple E container ships comparing to 47% peak efficiency for on-road heavy duty transportation [9], and large quantities of cargo can be transported in a single ship, which reduces the required specific energy to move one unit of cargo. However, while efficiency is high, toxic emissions remain high.

Marine transportation can roughly be divided into two categories regarding toxic emission legislation: sea-going vessels and vessels that

stay close to land, either by using waterways or by following coastal lines, here called waterway transportation. The guidelines from the WHO resulted in different interpretations, as the risks for these two categories are very different. Emission limits for sea-going vessels are higher than waterway transportation because less people are at risk. Currently, emission limits for in-land waterway transportation are reaching values on par with on-road transportation.

To compare the emission reduction progress between on-road and marine applications, a compilation of emission limits for road transport, e.g. trucks, personal transport and inland waterway transport is shown in Figure 1.3. Emissions for personal transport are expressed as a function of driven km, while emissions for trucks and inland waterway transport are expressed as a function of provided work in kWh, shown on the respective

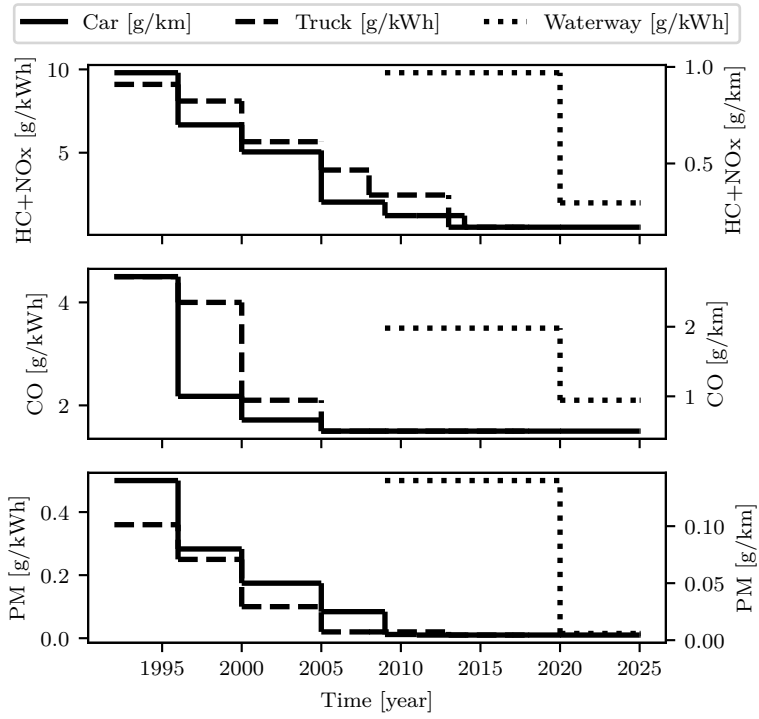

Figure 1.3: Progress of emission limits for cars, heavy duty trucks (in g/km*) and inland waterway transportation (in* g/kWh*). The plot is compiled out of data from the European emission legislation [15–17].*

right and left axes. These can thus not be compared directly, especially because test cycles differ as well, but the figure can be used to compare relative emission reductions.

Since the 1990s, both truck and car emission limits have dropped enormously by small steps in different iterations. On the other hand, toxic emissions of inland waterway transport have been largely neglected, until recently. Tightening emission regulations in 2020 will, in one step, reduce emission levels to values that are comparable to the latest on-road emission limits.

While the previous explanation focused on the European emission legislation and only discussed inland waterway transport, awareness about toxic combustion products results in similar emission limits in the U.S., with even stronger emission control areas near some harbors. Similar emission limits exist for other applications of these engines such as railway transportation and emergency generator sets. Sea-going vessels that operate in international waters have to comply with International Maritime Organization (IMO) regulations. Currently, limits for NO_x, oxides of sulfur (SO_x) and PM depend on emission control areas with stricter limits close to coastal areas.

1.3 Study of marine combustion engines

Given the high amount of total required energy it is simply impossible to rely on local renewable electricity alone. The remaining energy need has to be fulfilled with another energy carrier. In the short term a fossil fuel, which in the long term should be more and more replaced by an imported renewable, less carbon-intensive fuel that can be produced on the most beneficial location.

It is possible to produce renewable electricity from imported renewable fuels in large power plants and use this electricity to charge batteries in a full electric mobility solution, but this reduces total efficiency with the power plant and electricity transportation losses. The fuel could also be used directly in a transportation application, with the added advantage that expensive batteries are then unnecessary and a vehicle or ship can be refueled in a conventional way. Of course, the conversion from fuel to propulsion should be high to compete with battery electric energy storage.

While fuel-cell technology is theoretically more efficient (converting fuel in electricity for an electric drive) than an internal combustion engine, the actual efficiency depends on the employed fuel and drops in reality to around 50 % for hydrogen fuel and to 40 % for methane [18]. Additional challenges with fuel cells relate to lifetime, production cost and suitable

fuel supply as more complex fuels, such as ethanol, reduce system efficiency even more [19]. An internal combustion engine has a very high fuel flexibility, a high lifetime and uses abundantly available materials with a comparable efficiency to e.g. fuel cell technology. Because of these reasons, an internal combustion engine will have a place in society for a long time in the future.

Increasing public awareness about air quality and its effects on health causes all emission limits to become more and more stringent for all applications, including the ones that have escaped strict emission limits until now. Combustion of fuel can only be allowed when complying with these limits and this remains a problem for marine engines.

In this work the combustion process in engines that are used in international shipping, inland waterway transportation, railway transportation and for emergency power generation is studied. High formation rates of PM and NO_x are inherent to the direct fuel injection process which has been studied for on-road applications in detail (as will be explained in Chapter 2) but limited data exists for marine engines which limits the understanding of combustion in heavy duty marine engines.

While ambient gas conditions between heavy duty marine and heavy duty truck applications are comparable, injection equipment differs a lot. Injection equipment differs not only in size, but also by employed technology: pump line nozzle (PLN) instead of common rail. Recent investigations regarding the evaporation and combustion behavior with a PLN injection system in variable gas conditions are limited (explained in Chapter 2).

1.4 Goal

From the above explanation, it is clear that society will need a renewable energy carrier in the future (see Figure 1.2). Considering the high efficiency, reliability and fuel flexibility of a marine engine, this energy carrier could then be used in this engine to produce mechanical work. However, emission limits for heavy duty marine engines are becoming stricter and stricter. Adjusting the combustion process to reduce harmful emissions poses significant challenges to manufacturers. Solutions for automotive applications are available, but knowledge regarding marine engines is limited (further explained in Chapter 2). To improve the understanding of emission formation in marine applications, the source of these emissions should be studied. The goal of this PhD is therefore twofold:

1. A specialized test rig, the GUCCI, is developed further to allow an optical study of the injection process in well defined and repeatable experimental conditions (explained in Chapter 3). Based on engine measurements, several representative experimental conditions are determined and for these conditions the recording of a measurement database is started for a medium speed marine injection system (explained in Chapter 4).

2. The test rig currently does not allow a direct optical measurement of temperature and fuel concentration which is why a 1D spray simulation model is used in Chapter 5 to estimate local conditions in the combustion chamber for the investigated injection system. These local conditions are then used to explain the deviation of emission production from a 1D engine simulation code and engine measurements. Finally, an application to an advanced combustion method to reduce emissions is discussed.

2

Engine emission reduction

"You cannot escape the responsibility of tomorrow by evading it today."

- Abraham Lincoln -

In this chapter, the spray measurements, that are the core of this work, are motivated. It starts with a general introduction on reducing engine emissions. Because engine experiments are expensive, an attempt is then made to validate an engine simulation code for optimization purposes. Some important differences are found during the validation and in the third Section of the Chapter the possible reasons for this are discussed. It is found that the marine injection differs in multiple ways from well known automotive injections and in the final part of this Chapter the literature regarding injection and spray development is summarized.

2.1 Introduction

Engine design and development is focused on lowering all emissions: toxic emissions such as NO_x, HC, CO and soot but also greenhouse gases (mainly CO_2) should be decreased. Toxic emissions can be reduced by a number of technologies of which some will be introduced shortly. The margin for efficiency improvement is limited, as explained in the second part.

2.1.1 Toxic emissions

A conventional diesel type combustion excels in high efficiency but also emits high amounts of soot and NO_x which can be explained by the combustion process. Meeting current automotive emission regulations has required the development of a thorough understanding of in-cylinder processes.

Formation of NO_x is strongly temperature dependent while total soot formation depends mostly on equivalence ratio: when there is enough oxygen total soot production is limited [21] as the soot formation rate decreases with increasing oxygen concentration. This is shown in Figure 2.1: the diagram shows contour plots of the NO_x and soot production rates as a function of Φ (equivalence ratio) and T (temperature). The path of conventional diesel combustion is shown on the diagram, starting at a high equivalence ratio and low temperature at the nozzle. As fuel mixes with air, the equivalence ratio drops and temperature increases by partial combustion (producing soot). Finally, maximum temperature and a high oxygen concentration are reached in the diffusion flame (producing NO_x).

To reduce cylinder-out toxic emissions, several techniques can be applied that affect the gas temperature and the equivalence ratio. They rely on diluting the combustion to decrease combustion temperature and equivalence ratio [22], thus avoiding the zones with high formation rates of soot and NO_x. Mixture dilution can be achieved by exhaust gas recirculation (EGR) [23–25] or by using excess air [25].

2.1.2 Greenhouse gases

By adjusting the combustion process, toxic emission can be largely reduced in the future while only limited possibilities for greenhouse gas emission reduction exist.

Neglecting the combustion duration, the thermodynamic cycle in an internal combustion engine can be idealized as an Otto cycle with a

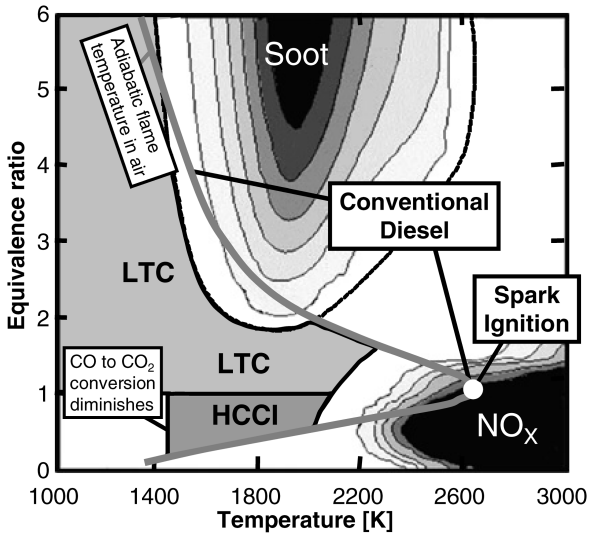

Figure 2.1: Φ-T diagram showing soot and NOx formation regions. Taken from [22].

constant volume combustion. The theoretical efficiency of this cycle increases with compression ratio, but with a decreasing improvement at higher compression ratios. On the other hand, higher compression ratios will result in higher peak pressures and higher friction losses.

While net gains in engine efficiency are certainly possible, it is necessary to reach 100% reduction of greenhouse gas emission at a certain point in time to limit global warming. Only a change in fuel can provide the necessary CO_2 emission reduction of an internal combustion engine in the long term.

Two fuel change examples are methane and methanol [14]. The usage of biogas and bio-methanol has the potential to reduce climate impact. As there is almost no chemical difference (except for impurities) between fossil and bio-derived equivalents of these fuels, engine adjustment could theoretically already start now without the availability of large amounts of biofuels. From a life cycle analysis that compared natural gas, biogas, methanol and bio-methanol, the improvement relative to heavy fuel oil regarding CO_2 emission was limited when using fossil derived alternative fuels [27], but climate impact can be reduced by switching to bio-derived equivalents.

Most heavy duty marine engines use compression ignition, so direct application of fuels with a high octane number (i.e. they do not auto-ignite easily) requires engine adaptations to run on these fuels. The

easiest solution is a dual-fuel fumigation approach [14, 28]. Fuel is then introduced into the engine's intake ports and premixed with air in the cylinder, with ignition being provided by a small injection of diesel fuel that auto-ignites and creates an ignition source for the whole mixture. The timing and quantity of the pilot injection is critical for the efficiency and emissions of the dual fuel engine. Using these fuels still requires research regarding the interaction between the pilot injection and the fuel-air mixture combustion. While this is not considered explicitly in this work, the results might be used to start this investigation.

2.2 Engine simulation

To obtain the best balance between engine efficiency, i.e. low fuel consumption, and engine emissions, the engine performance should be mapped over a wide parameter range. Depending on the engine configuration, the parameters include the EGR rate, the valve settings, the turbo configuration, fuel injection configuration, ... Because of this large parameter space, this work would be very time-, and fuel-consuming when performing experiments on an engine test-bench. This is where an engine simulation code can step in. Optimization with the help of a simulation code has the potential to reduce costs and shorten development time. Of course, the simulation code should be first validated against engine experiments and this is discussed in the following Section.

2.2.1 Simulation of gas dynamics and combustion

In an engine simulation code the complete engine can be split up in two main parts: **gas dynamics** and **combustion**, separated by valve closure.

The gas dynamics simulation finds a solution to the continuity equations formulated in one dimension and exists out of several parts, e.g.: the inlet and outlet manifold, the turbine and compressor, connecting pipes, after-cooler, valves and so on. In this work, this simulation is done by a commercial code: GT-Power. A more detailed explanation about gas dynamics simulation is given in Appendix B. The gas dynamics part of the simulation code was validated against the measurements with a very good agreement.

The gas dynamics simulation provides boundary conditions for the in-cylinder processes when the valves are closed: it determines total mass and species fractions in the cylinder and initial gas temperature. From the moment the valves close, the combustion model starts from these initial conditions together with a fuel injection profile to calculate heat

release rate and emissions that are produced during the combustion. In the following, the calculated heat release rate will be compared to the measured heat release rate.

2.2.2 DI-Pulse simulation model

The latest diesel combustion model available in GT-Power is named DI-Pulse: it predicts the combustion rate and emissions for direct-injection diesel engines with single as well as multi-pulse injection events. The basic approach of the model is to track a fuel pulse when it is injected. The fuel pulse evaporates, mixes with surrounding gas and burns. This is proprietary software and not all implementation details are available; in the description below the model is treated like a black box, more information is available in the manual [29] and in Appendix B.

In the DI-Pulse model four calibration constants are used to calibrate the heat release rate: an ambient gas entrainment $\mathbf{C_{ent}}$ constant, an ignition delay $\mathbf{C_{ign}}$ constant, a premixed combustion rate $\mathbf{C_{pm}}$ constant and one for the diffusion combustion rate $\mathbf{C_{df}}$. The prescribed procedure is to measure a wide set of engine setpoints that span the complete operating range regarding load, speed and so on. These measurements are then processed with a Three Pressure Analysis (TPA) technique which, based on the measurements, essentially results in cylinder conditions at inlet valve closure and a heat release rate for every operating point. More details about TPA are given in Appendix B.

The calibration of DI-Pulse then consists of matching the predicted heat release rate (HRR) with the 'measured' HRR from the TPA technique. During the calibration of DI-Pulse, the cylinder conditions at inlet valve closure of the measurement are imposed as the start condition for the simulation to avoid inconsistencies. The error between the measurement and the DI-Pulse simulation is then defined as the sum of squares of the difference between the measured and simulated heat release rate. One set of calibration constants are searched for all the measured operating points by minimizing the sum of the errors for all points.

2.2.3 DI-Pulse results

After calibration, results are compared between measurement and simulation. Three operating points are shown in Figure 2.2: 1000 rpm 100 % load, 630 rpm 25 % load and 1000 rpm 25 % load. These are engine load points in medium speed engine applications that are chosen from the emission test cycle (E2 and E3 from ISO8178), respectively full engine load, 25 % propeller-law load and 25 % constant speed load. On the left-hand side of the figures the cylinder pressure is shown as a function of

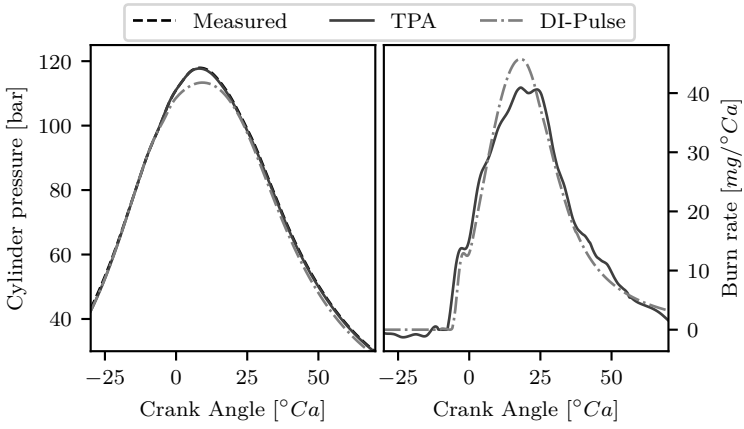

(a) 1000rpm 100%

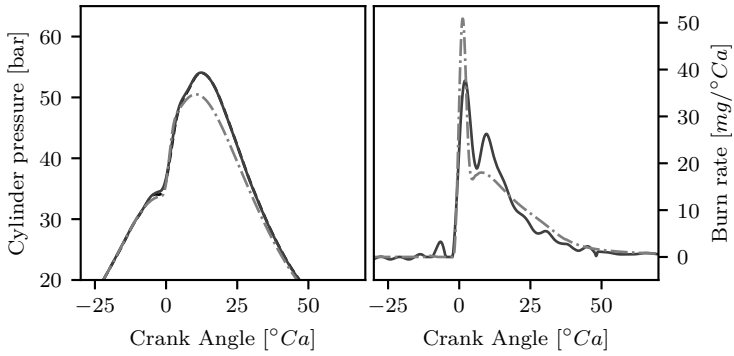

(b) 630rpm 25%

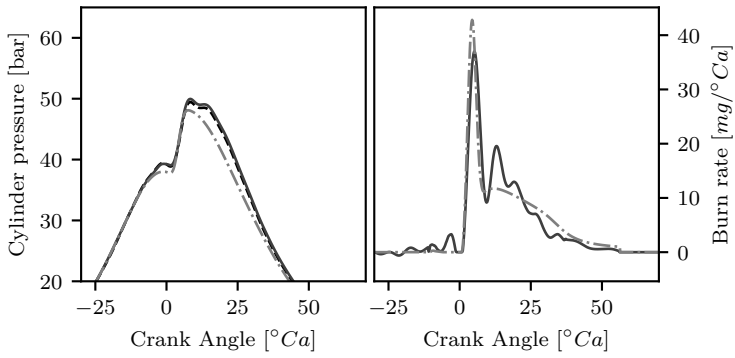

(c) 1000rpm 25%

Figure 2.2: DI-Pulse simulation code compared to the measurements. Pressure (left) and burn-rate (right) as a function of crank angle. Load point according to emission test cycle E2 and E3 from ISO8187.

crank angle: the measured pressure, the pressure from the TPA and the pressure that results from the DI-Pulse combustion model are compared. The measured pressure and pressure that results from the TPA procedure are indistinguishable which means that the cylinder charge and resulting HRR are correct for the different operating points.

On the right-hand side the ideal burn rate is compared to the predicted burn-rate by DI-Pulse. Although the burn-rates agree reasonably with the ideal one, there is still a difference in peak cylinder pressure. For high load cases, this can be explained by a slightly too long ignition delay. The predicted burn-rate is slightly delayed, which results in a delayed pressure increase and a lower peak cylinder pressure. For low load cases, the ignition delay time is right but the premixed combustion rate is too high, which means that cylinder pressure increases initially very quickly. During the diffusion combustion the cylinder pressure starts to deviate more for low loads. Predicted diffusion combustion at low load happens too slowly, and at high loads the opposite happens: diffusion combustion is too fast.

NO_x emissions were calculated by using the extended Zeldovich mechanism, but exact implementation details are hidden in the software. Experimental NO_x emissions are compared to DI-Pulse simulated NO_x emissions, shown in Figure 2.3, on the left hand side engine speed varies according to the propeller law to vary the engine load and on the right hand side engine speed is kept constant. NO_x emissions that result from the simulation are double the measured emissions. To allow a comparison of trends, emissions from the simulation (in ppm) are divided by two to present the results. This was proposed in the GT-Power manual. Two simulation results are shown: a single cylinder simulation and a

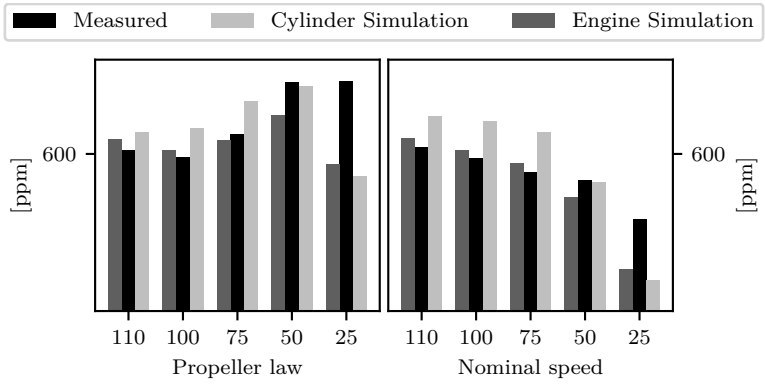

Figure 2.3: NOx emission for several load setpoints on E2 and E3 emission test cycle from ISO8187. Emission values from the simulations were halved to present results.

simulation of an engine with the whole intake and exhaust system.

The engine simulation shows a better agreement to the measurements than the single cylinder simulation, except for the lowest load where simulation and measurement always show a big difference. Because of a large valve overlap and a positive pressure difference between the inlet and outlet manifold, exhaust gases are diluted by fresh intake air which reduces ppm levels. This explains lower ppm levels at higher loads because exhaust gases are diluted more at higher loads.

The increasing NO_x emission trend with decreasing load with the propeller law is predicted well with the DI-Pulse model with the full engine model. Similarly, the decreasing NO_x emission trend with decreasing load at constant engine speed is also captured by the model, except for the lowest load.

Some conclusions can be drawn here: while general trends are predicted well by the model, it is impossible to trace the source of emissions as no detailed information from the combustion model is available. A high overall emission multiplier (0.5) is necessary to match simulated NO_x emission to measured NO_x emission and finally there exists a strong load-dependent deviation in NO_x emission prediction.

To better understand the deviation in heat release rate and emission prediction, insight in the combustion process for this type of engine is necessary.

2.3 Combustion in marine engines

To identify the differences between a marine engine and engines for road applications typical engine specifications can be compared in Table 2.1. Time and length scales in the combustion chamber of a marine engine are vastly different: they differ by an order of magnitude. Nominal engine speeds in marine applications vary from 1000 rpm to as low as 500 rpm at full load, which means that combustion duration takes five to 25 times as long compared to on-road applications. The same is valid for the size of the combustion chamber, e.g. the cylinder bore varies from 200 mm to over 400 mm, again significantly bigger (three to six times) than on-road applications. Secondly, the employed fuel injection system differs by technology. A PLN injection system is still widespread in marine engines. For road applications, a common rail (CR) system is now the only employed fuel injection system.

The combustion differences between marine and on-road applications can be split up in two main categories: ambient conditions at top dead center (TDC) caused by the difference in size and speeds and the difference

Table 2.1: Comparison of the investigated engine to more commonly known engine types.

	Medium Speed	HD Road	Road
Bore	200 mm - 400 mm	110 mm - 150 mm	70 mm - 90 mm
Stroke	300 mm - 450 mm	140 mm - 180 mm	70 mm - 90 mm
Cylinder displacement	30 l - 50 l	1 l - 2 l	0.3 l - 0.5 l
Cylinder power	200 kW - 700 kW	35 kW - 70 kW	10 kW - 30 kW
Max speed	1000 rpm	2400 rpm	4500 rpm
Injection system	PLN and some CR	CR	CR

in injection equipment. The small differences in ambient conditions at TDC are described first. Injection equipment shows bigger differences and these will be discussed in the second part.

2.3.1 Ambient gas conditions

Ambient gas conditions of a typical medium speed marine engine with a power of around 200 kW/cylinder are shown in Figure 2.4 as a function of crank-angle. These results were generated with the calibrated engine simulation code (see Appendix B). A conventional start of injection range is shown by gray dashed lines. On the left-hand side density and temperature in the cylinder is shown as a function of crank-angle for varying engine load, together with the typical start of injection (SOI) range: currently conditions vary from 10 kg/m^3 and 750 K to 40 kg/m^3 and 900 K at SOI without EGR.

These conditions are similar to on-road heavy duty engines: typical conditions were determined by the Engine Combustion Network (ECN). The ECN is a group of research institutions that investigates the spray development and combustion for on-road applications [30]. They define a "Spray A" condition to represent a relatively low temperature combustion condition, relevant to truck diesel engines that use a moderate amount of EGR (900 K, 22.8 kg/m^3, 15 % O_2).

The influence of EGR rate on ambient gas conditions is shown on the right-hand side of Figure 2.4 for 50 % engine load. EGR rate was increased to 30 and 60 % while maintaining a constant air-fuel ratio by

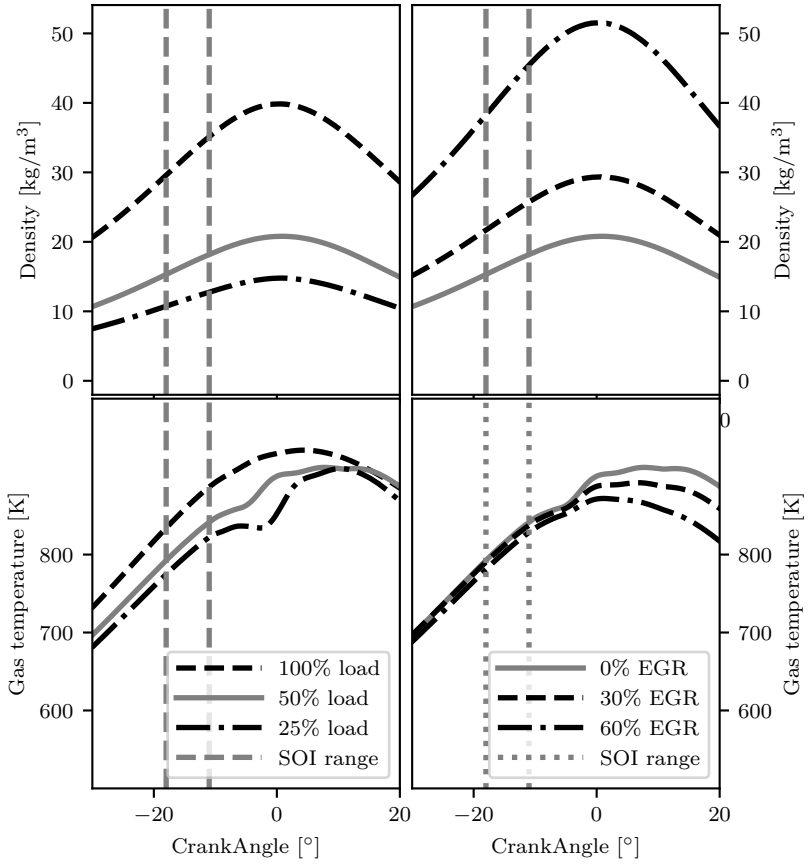

Figure 2.4: Cylinder density and temperature as a function of crankangle for varying load (left) and EGR rate (right).

increasing the manifold pressure. From these simulations, the 30 % EGR rate case has a similar ambient condition as defined in "Spray A".

Because of the small differences in ambient gas conditions compared to on-road heavy duty, our experiments will be based on the ECN parametric variation to allow comparison with literature. The exact conditions are described in Chapter 4 and are shown in Table 4.1: an evaporating measurement set varies target density and SOI temperature. Target density is chosen slightly lower compared to ECN to protect the test bench and target temperature is chosen at 850 K instead of 900 K because the typical obtained SOI temperature during simulation was found to be 850 K.

Ambient gas conditions at TDC determine development of the fuel spray out of the injector after fuel is atomized close to the nozzle hole. Initial velocity decreases because of momentum transfer from the ambient gas to the fuel and ambient gas entrainment increases the fuel's temperature leading to its evaporation and combustion. Gas density, heat capacity and temperature determine the speed of these respective processes and will thus influence the resulting penetration speed, liquid length and ignition delay. This is further explained in Section 2.4.

2.3.2 Injection differences with on-road applications

While CR direct injection is virtually the only system used for on-road transportation, this is not the case for marine applications. The advantages regarding injection timing and pressure flexibility of a CR system cannot be ignored, but for marine application there are still concerns regarding reliability and complexity of the system. Maintenance intervals of large engines are long and when an essential component breaks in a remote location limited options exist to repair it immediately. This is why conventional PLN injection systems are still widespread in shipping.

In a marine engine every cylinder is equipped with a PLN system that exists out of a camshaft driven high pressure pump connected to a mechanical fuel injector by a high pressure line. Injection pressure increases from the residual pressure until peak injection pressure during every cycle and the injector opens when pressure reaches the start of injection pressure. At low engine speed and low fueling rates, the maximum attained pressure in the pump is low which limits the start of injection pressure to relatively low values.

On the other hand, in a CR system the pressure buildup is separated from the injection. A high pressure pump fills a common rail up to a target pressure. The injector is opened at the desired time with an electronic actuator. This essentially removes the speed and load dependence of injection pressure that is present in a PLN injection system.

Another difference lies in the manner of lifting the needle in the injector. Both systems rely on a force balance on the needle: a spring provides a force to close the needle. Part of the needle is subject to the injection pressure and this is where a CR and PLN system start to differ. A cutaway view of the bottom of a common rail injector is shown in Figure 2.5. Rail pressure is provided at the top right (48) and reaches the bottom of the needle through several channels. A small passage (59) builds the same pressure above the needle and combined with the spring force the needle remains closed. When the common rail injector is electronically activated (either by actuating a solenoid or a piezo-

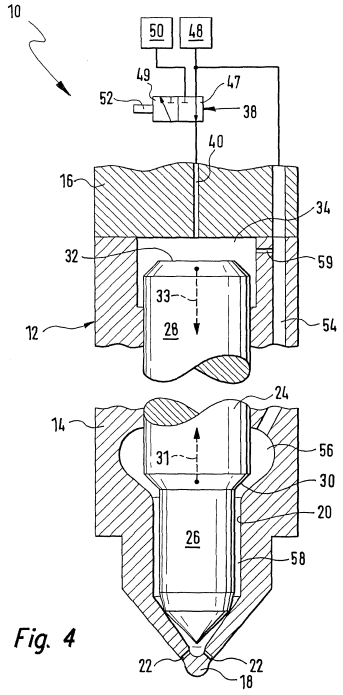

Figure 2.5: Cutaway view of the bottom of a common rail injector. Taken from [32].

element), the passage on top (40) is opened which releases the pressure above the needle. The force balance shifts and the needle lifts.

A PLN system works similarly, but without the top passages. Now, when the force exerted by injection pressure equals the spring force, the needle starts to lift. Because of this lift, the volume under the needle (sac volume) starts filling up and injection pressure shows some decrease during initial lift. This decrease might reduce the lifting speed, the net effect depends on the sac volume and flow resistances inside the injector body. Something similar may happen in the CR system though. When pressure above the needle does not decrease fast, e.g. due to the limited motion of the piezo-element, the lifting speed of the needle will also be lower. The lifting speed is important, because it influences hole cavitation.

In [35] a truck sized PLN injection system was compared to a common rail diesel injection system (nozzle hole diameter 200 µm). The authors observed a slow common rail needle lift opening compared to PLN

and throttling over the needle seat in the early phase of the injection process. In current CR injectors, slow needle lift is avoided by hydraulic amplification of the stroke of the piezo-element [36, 37].

It is important to see that lifting speed is determined by the force balance on the needle and that this is affected by the design of the injector. A CR injector has the distinct advantage that full injection pressure is available at the start of injection and higher needle velocities are therefore possible. This does however not imply that needle lift on PLN systems is slow: when properly designed with small sac volumes, needle lifts will also be quick. The biggest disadvantages of a PLN system are that only one injection is possible for every cycle, that injection timing is fixed mechanically for the whole operating range and that injection pressure depends on fueling rate and engine speed.

Finally, the size difference is illustrated in Figure 2.6: note that part of the common rail injection (left) consists of the actuator while the PLN injector is only the hydraulic part, adding a actuating coil would double the size of the injector. The hole diameter is much larger and because of this L/D ratio decreases. It is not fully understood and documented how these different dimensions and injection equipment affect nozzle flow which in turn partly determines downstream spray characteristics. Additionally, the effect of this larger combustion chamber and longer possible combustion duration on emission formation is not investigated in literature in detail for the case of this type of injectors.

For the remainder of this chapter, the available literature regarding spray development is discussed. These results are mostly obtained for road-applications.

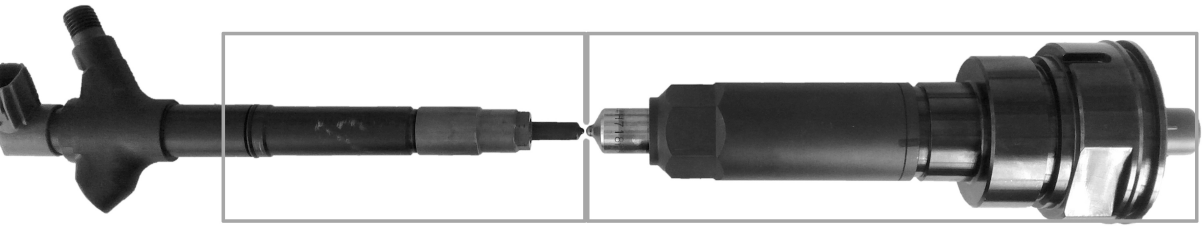

Figure 2.6: Mechanical injector from marine application compared to a common rail injector from automotive application. The mechanical part is indicated with the squares.

2.4 Combustion of direct fuel injection

The process of spray combustion can be divided into three parts: fuel flow in the injector, atomization and evaporation of the liquid fuel and finally ignition and combustion. These processes are highly coupled and by performing optical experiments, one strives to understand these processes better over a range of boundary conditions.

Multiple optical techniques have been developed to study different aspects of the spray: vapor and liquid penetration are visualized separately to study the atomization and evaporation rate. Natural luminosity, chemiluminescence (light that originates from radicals at a specific wavelength) or laser induced fluorescence (similar to chemiluminescence but chemical elements are now excited by a laser pulse) are used to study ignition and combustion processes.

First, fuel flow in the nozzle is discussed as this influences the atomization and initial velocity of droplets to a great extent. Then the main influencing parameters on atomization and evaporation are discussed and finally the ignition process of the evaporated fuel and ambient gas mixture is described to identify regions in the spray with high and low emission formation risks.

2.4.1 Nozzle flow

Nozzle flow is affected in different ways by the injection system. The shape of the nozzle hole in particular has an important influence on the onset of spray atomization when the spray exits the nozzle hole. Because of the small nozzle holes and relatively high pressure differences, cavitation is likely to occur and this affects downstream spray characteristics.

Fuel is accelerated in the nozzle because of the large pressure difference between the nozzle and the outlet. When the nozzle hole has sufficiently sharp inlet edges, the flow changes direction quickly and inertia forces cause an additional pressure reduction: flow separates from the hole walls and a recirculation zone is formed. When pressure in the recirculation zone drops below the vapor pressure of the liquid, cavitation bubbles appear. Depending on the chamber pressure, injection pressure and geometry of the nozzle, these cavitation bubbles collapse close to the inlet of the nozzle hole or the recirculation zone develops further into the nozzle. Cavitation bubbles are then transported further in the nozzle hole. As the pressure difference increases for a given injection pressure, cavitation was found to develop over the whole nozzle length, as was observed by using upscaled transparent nozzles during optical measurements [38, 39].

Theoretical mass flow rate through a nozzle hole can be calculated by applying Bernoulli's flow rate equation:

$$\dot{m}_{th} = A \cdot \sqrt{2 \cdot (P_{inj} - P_{back}) \cdot \rho_f} \tag{2.1}$$

with A the nozzle hole exit area, P_{inj} the injection pressure, P_{back} the pressure at the hole's exit and ρ_f the fuel density. While this theoretical mass flow rate depends on the pressure drop over the nozzle, the actual mass flow rate does not increase when chamber pressure is reduced for a fixed injection pressure when cavitation occurs. This is described theoretically by [40] and observed by many authors when nozzle flow rate was measured for different injection and chamber pressures [41, 42].

At this mass flow stagnation point cavitation is starting to play a role in two ways: the area, available for liquid fuel, decreases as part of the nozzle hole is occupied by vapor. Secondly and because of this reduced area, friction with the wall becomes limited as the liquid fuel is mostly surrounded by vapor. This results in a higher exit velocity, compared to non-cavitating flow. These two deviations result in a stagnating mass flow while flow velocity still increases and two flow coefficients are defined in literature to describe these two deviations: a velocity coefficient and an area coefficient. Additional explanation about nozzle flow and definition of the flow coefficients is given in Appendix C.

2.4.2 Atomization and Evaporation

The evaporation process consists of three main processes: primary and secondary **breakup** and **dispersion** of the droplets into ambient gas. These droplets then **evaporate**. Primary breakup is the process that occurs when fuel exits the nozzle: by aerodynamic drag, jet turbulence and cavitation in the nozzle, droplets and ligaments are formed. Once these droplets are created they break down further during secondary breakup into smaller droplets. These small droplets then mix with ambient gas, heat up and start to evaporate.

Spray characteristics

The complete spray atomization is usually characterized by the spray angle: several definitions of the spray angle based on high speed imaging exist in literature and the most important ones are discussed in Section 3.3.2. Although comparing the exact values of spray angle is difficult because of different spray spreading angle definitions and different optical measurement techniques, authors found similar trends. Spray angles can be measured in the near field or on a macroscopic scale.

Near field spray angle measurements focus on an area limited to around $5mm$ from the nozzle hole and are mainly influenced by nozzle flow changes, while macroscopic spray angles are measured on the complete spray development and can be influenced both by ambient gas conditions and nozzle flow.

A clear increase of the macroscopic spray angle with increasing density ratio of air and fuel (ρ_a/ρ_f) was found in [43] and [44]. The spray angle changes during the injection process: a wide spray angle is found in the beginning of the injection before transitioning to a lower steady state value [34]. This phenomenon has different explanations: low initial gas motion causes more drag which results in a higher initial spray angle, the flow in the nozzle is still developing and spray angle detection is not very reliable when spray penetration is small because limited data (for line fitting to detect the angle) is available.

The effect of cavitation on atomization is very large: implosion of cavitation bubbles creates instabilities in the exit flow which promotes primary atomization to a great extent [45]. The result of this improved atomization can be witnessed from optical studies when the near field spray angle is measured. The spray angle near the nozzle increases when cavitation is stronger [38, 39, 46] which indicates a finer dispersion of droplets during the atomization process. In typical light and heavy duty injection conditions, a certain amount of cavitation is always present due to the high injection pressures and small nozzle holes which always results in a very finely dispersed fuel spray during the injection. The effect of increasing cavitation is shown in Figure 2.7. These pictures have been obtained by recording the spray of an upscaled optically accessible nozzle. Injection velocity increases from left to right. With increasing velocity, cavitation progresses further into the nozzle hole which influences the atomization near the exit as well.

Spray angle was found to be almost unaffected by injection pressure during typical diesel operating points [47], however some authors claim to measure changing spray angles when injection pressure varies [44, 48], but clear trends have not yet been shown. A partial explanation can be given by the onset of cavitation. During needle lift, throttling happens over the needle instead of over the nozzle holes and pressure in the sac volume remains low which decreases cavitation. As the needle lifts higher, the injector holes start to be the main throttling losses and cavitation increases again. A computational fluid dynamics (CFD) simulation study [33] of a common rail system showed that during needle lift, cavitation moved from the bottom to the top of the orifice due to changing stream lines, which would influence the spray atomization greatly. Liquid, non-atomized fuel was observed in [34] close to the nozzle at several moments during the injection when spray angle values were small. This lack of

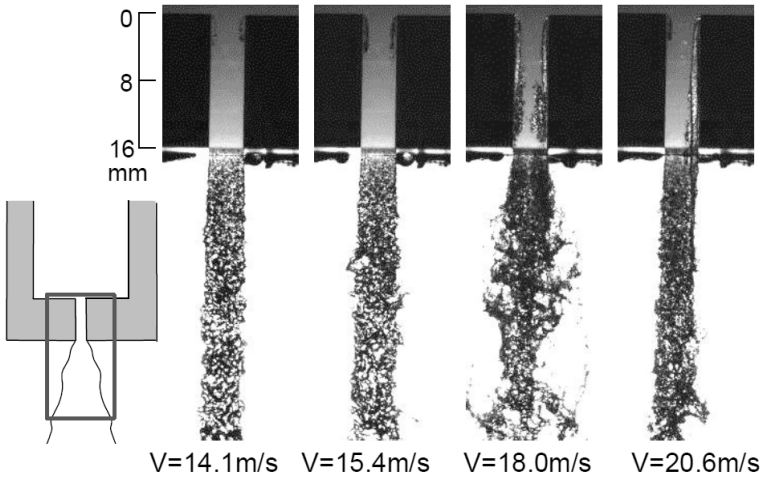

Figure 2.7: Visualization of the spray behavior that results from different cavitation regimes (taken from [39]).

atomization indicates a low amount of cavitation in the nozzle, which resulted in a small spray angle value.

Spray angle stability is also found to be sensitive to the relative position of the hole to the sac volume of the nozzle: a single hole nozzle with an axially drilled hole provided very stable spray angles with a low standard deviation over time during the steady state spray angle part because of a very smooth flow transition from the sac volume to the nozzle hole. Repeating the measurement with nominally the same size holes drilled in a three hole injector, spray spreading angle started to oscillate more [44]. Additionally, the spray mean axis angle (defined as the angle between the geometric spray direction and the actual spray direction) started to oscillate slightly as well. Again, this shows that internal flow structures in the nozzle affect macroscopic spray characteristics.

It is clear that cavitation, jet turbulence and aerodynamic drag are highly important mechanisms for atomization and spray angle development, each with their importance on certain aspects of the spray. Nozzle flow strongly affects initial jet turbulence and cavitation which in turn strongly changes the near field spray angle, while the effect on spray angle of aerodynamic drag is influenced by gas and liquid density. Aerodynamic drag has a smaller effect on the spray angle than cavitation, but it still influences the macroscopic spray angle.

Liquid length linearly increases with increasing orifice diameter and is not influenced by injection pressure [49, 50]. Ambient gas density

and temperature have strong effects on liquid length: increasing gas density and/or temperature causes a decrease in liquid length but with a decreasing sensitivity as they increase [49, 51, 52]. A fuel temperature increase results in a linear decrease in liquid length.

Fuel vapor penetration is found to not be influenced by gas temperature [51, 52]. Increasing ambient density decreases vapor penetration [48]. Increasing injection pressure increases spray penetration [48] because the injection velocity increases.

Mixing limited evaporation

Based on the above measurement results Naber and Siebers [47] showed that for CR diesel technology, atomization is quick enough so that droplets are always available in high enough amounts such that mixing with ambient air is the limiting factor for evaporation. This was examined by studying the liquid length dependence on orifice diameter and injection pressure [49]. This dependence can either be controlled by mixing or by local interphase transport processes which will be compared in the next paragraphs.

If the mixing-controlled model is assumed, local interphase transport is fast relative to the mixing rate. Droplet evaporation is controlled by the rate at which energy is entrained in the spray, which is directly proportional to the ambient gas mass entrainment rate. When the fuel mass flow rate increases, the entrainment of air needs to increase to supply the energy for complete evaporation.

In [47] relationships for the fuel injection rate and air entrainment rate are derived by applying conservation of mass and momentum to a simple conceptual model of a spray:

$$\begin{aligned} \dot{m}_f &\simeq \rho_f \cdot d^2 \cdot U_f \\ \dot{m}_a &\simeq \sqrt{\rho_a \rho_f} \cdot d \cdot x \cdot U_f \cdot tan(\theta/2) \end{aligned} \tag{2.2}$$

with ρ_a the ambient density, ρ_f the fuel density, d the orifice diameter, U_f the injection velocity, x the axial distance from the orifice and θ the spray spreading angle. The first equation states that the fuel mass flow rate at any axial location is equal to the injection rate and is proportional to the square of the orifice diameter. The second equation shows that the rate of energy supplied to the spray by air entrainment is proportional to the orifice diameter, the axial location in the spray and the injection velocity.

Assuming all other parameters fixed, varying the orifice diameter results in a linear dependence between orifice diameter and the length of the spray needed to entrain enough air to evaporate all liquid. For example, doubling the orifice diameter doubles the entrained gas, but quadruples the amount of injected fuel. This means that a longer spray length (increasing x) is needed to supply enough energy to evaporate all the fuel.

On the other hand, by assuming the local interphase transport limit one should look at the lifetime of a droplet in contact with gas containing more than enough energy to evaporate the droplet. The orifice diameter was found not to influence the mean diameter of the droplets strongly in the considered injection pressure range [53], while the lifetime of the droplet linearly depends on its diameter.

Siebers gave a numerical example based on the above discussed literature: a factor five increase in orifice diameter would result in a 50 % increase in mean droplet diameter and 50 % larger droplet penetration (liquid) under the local interphase transport limit. This is significantly less than the measured factor of five increase in liquid length which means that this conceptual model is unable to explain the measurements and that local interphase transport is not the rate limiting step. The mixing controlled assumption is able to explain this by a linear relationship between the orifice diameter and liquid length. Evaporation of high pressure diesel injection is thus controlled by air entrainment when sufficiently high injection pressure is achieved and atomization is fine enough.

With the PLN injection equipment, lower injection pressures are typical at lower load points. Even at higher load points, the injection pressure starts at a low value, and increases during the injection process to a peak value. It is not known how this influences the validity of the mixing limited evaporation hypothesis when it is applied to PLN injection systems because the injection pressure influences cavitation, atomization, and finally the evaporation.

2.4.3 Ignition and Combustion

Typical diesel spray combustion happens in two stages: a first stage ignition with a low amount of heat release which then develops in a highly exothermic premixed burn. These two stages will be observed in Chapter 4 when discussing the measurement results. Depending on the boundary condition these stages are more or less separated from each other. This insight was described by Musculus [58] and is based on optical measurements from several authors. This behavior depends on the fuel: i.e. iso-octane shows a single stage ignition.

In conventional diesel combustion, these two stages cannot be observed easily because they partially overlap. In this case, the apparent heat release rate (AHRR, i.e. neglecting heat losses) is divided into three parts: ignition delay, premixed burn and mixing controlled combustion. This is shown in Figure 2.8 in the top left figure, together with the needle lift for a low load operating point. After the start of fuel injection liquid fuel starts to evaporate and cools down ambient gas which is shown as a small negative heat release. Once fuel starts to heat up enough it starts to react and then heat release becomes positive again which is commonly used as a marker for start of combustion. The premixed burn that follows consumes all the oxygen in the current mixture and the AHRR reaches a maximum. During the premixed burn, combustion speed and thus AHRR is controlled by chemical kinetics in the mixture that was formed during the ignition delay and by the total mass of premixed fuel. After this premixed burn, the AHRR decreases to a somewhat lower level. Now, combustion speed is controlled by mixing speed, rather than by chemical kinetics.

In more diluted conditions, these two ignition stages are visible separately in the heat release rate due to chemical kinetics of the ignition process. This method shows promise for road applications [22–25] and is achieved either by EGR or by air dilution. During the measurement campaign, the effect of diluted combustion will be estimated for PLN injection systems.

The injection profile and AHRR are shown on the top right of Figure 2.8 for an EGR diluted combustion, with a similar load as the described conventional diesel combustion. The crank angle degree values at SOI in these plots are zero to compare the timings between the two combustion conditions. In reality, injection timing would be shifted either earlier, or much later during LTC operation to obtain lower gas temperature at SOI.

Initially fuel evaporation shows the same negative heat release rate and then heat release starts to rise when combustion starts. This first stage of positive heat release is short and it starts to decrease before strongly increasing to a very high peak value. Evidenced by the combustion peak, and without apparent mixing controlled combustion, most of the heat release happens very quickly and this results in a high pressure rise rate and combustion noise. This two-stage combustion can be explained with the help of chemical kinetics.

Chemical kinetics can be used to calculate the evolution of a reaction. It starts with reactants, which are converted by a number of intermediate reactions to the final products. The development of a reaction scheme for combustion of fuel is a very complex task [59], which is why a single component fuel with similar properties is sought: a surrogate fuel. Several schemes have been developed: e.g. for n-dodecane [60, 61] or as a reduced

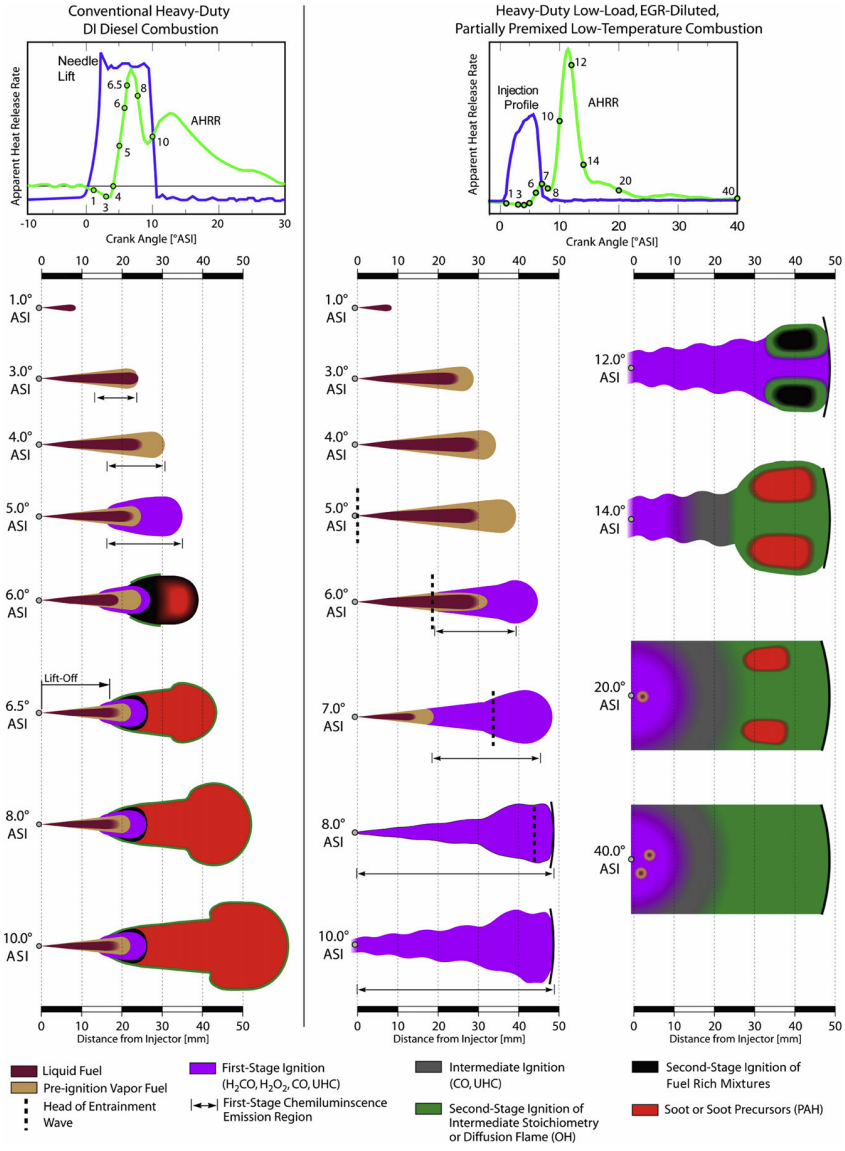

Figure 2.8: Conceptual model of conventional diesel combustion (left hand side) and extention to low-load EGR-diluted low temperature combustion (LTC) (right hand side), taken from [58]

version [62] with less reactions and species to decrease computational time.

The detailed mechanism from Lawrence Livermore National Laboratory (LLNL) was used by Musculus to investigate the combustion of n-heptane in a closed reactor at constant pressure for a diluted mixture. A distinct two-stage combustion was observed, similar to the AHRR from the engine measurements. These two stages could be characterized by the presence of specific intermediate reaction species. The transition from the first to the second stage was found to be governed by the mixture temperature. Once the mixture reaches 1000 K, the reaction rate rapidly increases.

The above description is valid for diluted combustion, but the same reactions are present in conventional diesel combustion. Less dilution and injection closer to top dead center result in higher ambient temperatures and richer mixtures and these affect the time-delay between the first and the second-stage ignition. Simulations of richer mixtures result in a shorter second-stage ignition delay, which is caused by an increased temperature rise during first-stage ignition. As temperature approaches 1000 K near the end of first stage ignition, the second-stage starts almost immediately. On the other hand, when the initial dilution results in a relatively low ambient temperature, the two stages can be observed separately. This results in the LTC combustion method.

Some of these intermediate species can be easily detected by optical diagnostics in spray measurements. The combustion structure of a reacting spray was studied by Bruneau in [63] in a constant volume combustion chamber. By employing two laser sheets, characteristic species for the two combustion stages could be visualized. While the ambient conditions resulted in a conventional spray combustion, the first stage ignition could be optically separated from the second stage ignition. Second stage ignition was present over the spray edge, with first stage ignition visible in the core of the spray. The two ignition stages were not separated in time, but were separated in space in this work.

A similar study was done by Genzale [64] at lower ambient oxygen concentrations in an optically accessible engine. Analysis of the AHRR showed a highly premixed two-stage combustion: LTC was achieved by the low oxygen concentration and a delayed SOI until well after top dead center. The first stage ignition was detected well before the second stage ignition. The second stage ignition started at the head of the spray which had the largest mixing time and highest temperature. The second stage ignition does not initially appear at the center of the spray, instead it was observed in structures off the spray-axis.

A conceptual spray combustion model was based on optical measurements by Dec [22] and extended by Musculus [58]. The spray development at several time steps after SOI for a conventional diesel injection and

for a LTC condition is shown in Figure 2.8. For the first three crank angle degrees the evolution of the spray is very similar: liquid fuel and vapor penetrate together until near 3° after SOI, after which vapor fuel penetrates beyond the liquid.

After initial penetration, ignition processes from the conventional combustion deviate from the LTC spray. While the conventional spray burns to completion with high soot production rates, the LTC only shows first stage ignition.

For conventional diesel combustion, regions that first ignite, are fuel rich and soot precursors appear during the premixed burn. The diffusion flame appears in the periphery of the spray close to the timing of soot precursor formation which indicates simultaneous combustion at fuel-rich and intermediate stoichiometry conditions. The diffusion flame grows quickly around the spray. A zone of first-stage combustion products exists upstream of the diffusion flame, as observed by [63].

For LTC conditions, second stage ignition only starts after the end of injection (EOI) so OH is distributed through much of the spray's cross section where mixtures are of intermediate stoichiometry. Some fuel rich pockets remain in the downstream spray: formaldehyde is consumed but OH cannot accumulate because of the local equivalence ratio. Soot formation happens in these small pockets symmetrically around the spray axis, surrounded by OH, observed by [64].

2.5 Summary

Conventional fuel injection, relatively close to TDC at high ambient temperatures leads to zones with a high equivalence ratio and high temperature close to the nozzle and stoichiometric, high temperature zones in the diffusion flame. These zones are characteristic for high formation rates of soot and NO_x and these develop depending on the initial ambient gas conditions; but also depend strongly on injection equipment.

To reduce optimization time, a commercial engine simulation model was utilized to predict the combustion rate of a marine diesel engine that still employs a PLN direct injection system. While it was possible to calibrate the model for high engine loads, this calibration resulted in emission prediction deviation and HRR deviation for low engine loads. Additionally, the prediction of NO_x emission was twice the measured value. Clearly, due to the underlying model assumptions, not all physics of the injection process were captured.

Emission formation and efficiency are largely influenced by the combustion process and underlying physics. A compression ignition engine relies on high pressure direct fuel injection and this consists out of several physical processes: nozzle flow, atomization, mixing with ambient gas and evaporation and finally ignition and combustion. These processes are all influenced by the ambient gas conditions and the injection equipment. Relatively small differences between the investigated marine engine and on road application regarding ambient gas conditions were found.

On the other hand, the injection equipment shows distinct differences. It is not completely clear from literature how large sprays for marine application would develop as the time and length scales are much bigger. This work tries to contribute to the knowledge of marine diesel sprays and its effects on the emission formation for a wide range of boundary conditions.

3

Fuel Spray Measurement Equipment

"There are no big problems, there are just a lot of little problems."

- Henry Ford -

In this chapter the most important features and improvements of the GUCCI setup are described, ranging from the PLN injection system to the gas filling system and data acquisition. Next, the used optical high-speed imaging techniques are explained. Then, the post-processing methodology is shown, together with best practices to obtain the most robust and reliable spray metrics from the measurements. Finally the measurement methodology is described.

3.1 Ghent University Combustion Chamber I

To study fuel sprays at conditions relevant to an internal combustion engine at the time of injection, a high temperature high pressure environment is reproduced in an optically accessible constant volume combustion chamber: The Ghent University Combustion Chamber I (GUCCI). This measurement rig was designed and improved over time by several PhDs [65–67], the current state is shown in Figure 3.1. Other facilities have been designed to study fuel sprays with similar conditions [49, 68, 69], but the one used here was sized to house bigger marine diesel injectors.

A comparison of the main characteristics of several constant volume combustion chambers is given in Table 3.1. The Eindhoven High Pressure Cell is the smallest chamber in this comparison and is mainly used for investigations for road applications [50, 70, 71]. The biggest chamber in this comparison is the Spray Combustion Chamber which was designed to measure marine two-stroke engine injections. A different filling process results in a strong swirl during a spray measurement, not representative for a four-stroke marine diesel engine. The sprays were visualized through a relatively small window of 100 mm diameter. By measuring multiple times and by moving the window, the whole spray could be visualized with the help of post-processing.

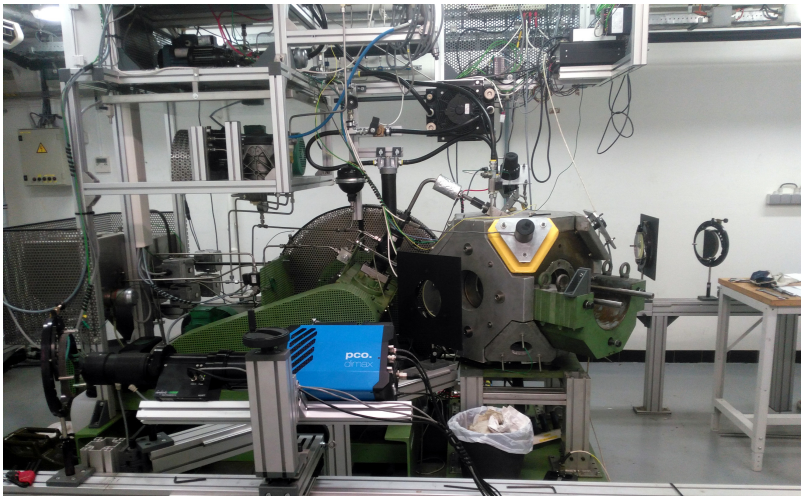

Figure 3.1: The current state of the GUCCI setup: high speed camera (blue) in front, the combustion chamber with yellow insulation piece slightly right off center and the injection system on the left. Various conditioning components are mounted above the injection system.

Table 3.1: Main specifications of the GUCCI setup compared to the Eindhoven High Pressure Cell (EHPC) [71] and the Spray Combustion Chamber (SCC) from the Hercules project [69, 72].

	GUCCI	**EHPC**	**SCC**
Dimensions	Cube with edge 160 mm	Cube with edge 108 mm	Cylinder with diameter 500 mm
Main application	Marine 4-stroke	HD road	Marine 2-stroke
Gas conditioning	Pre-burn	Pre-burn	Fast high pressure, high temperature gas filling
Turbulence and Mixing	Mixing fan	Mixing fan	Strong swirl during experiment to represent two-stroke engines
Optical access	Complete spray 150 mm	Complete spray 100 mm	Partial spray 100 mm, expanded to 150 mm, glass can be rotated to combine images over multiple experiments

3.1.1 Design overview

The design is a cubical chamber with openings on every face and in every corner of the cube. Removable inserts can be placed in these openings (see Figure 3.2): the respective glass and diagonal pieces. Because of its complex shape the chamber was made from of a solid block of Stavax steel by electrical discharge machining. Glass insert pieces are used for optical access by mounting a glass element in the inserts, but the system was designed to be able to hold other components as well. They are also used for mounting the injector and a rupture plate into the chamber. The rupture plate is used to protect the windows from excessive pressure. On the diagonal pieces other measurement equipment is added such as the chamber pressure (AVL QC34D) sensor and a thermocouple reading. A stirring fan is mounted on one diagonal piece to provide a homogeneous mixture and temperature throughout the experiment. A compressed air and a gas connection is also made through these diagonal pieces. The basic setup was built mainly during the PhD of Galle [67]. In Table 3.2 an overview of the improvements that were made in this work is given. For the remainder of this section, this will not be emphasized to improve the readability of the text.

3.1.2 Injection system

The injection system is currently a PLN system: a cam driven pump compresses fuel into a high pressure line and the fuel pressure then mechanically opens the injector to start the injection, shown in Figure 3.3a.

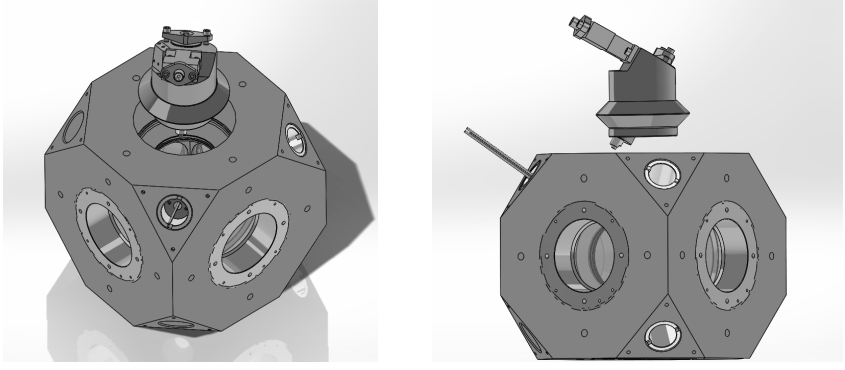

Figure 3.2: View of the GUCCI with its diagonal and window pieces, the injector piece is shown at a higher position.

Table 3.2: Overview of improvements of the GUCCI setup that were made in this work, grouped by the different subsystems in the setup.

	Original	**Improvement**
Injector cooling	Problem with the oil viscosity: too low to lubricate the oil pump.	Redesigned for higher viscosity, higher flow losses required redesigned tubing.
	Regulation of cooling power not sufficient.	Redesigned cooling hardware and software part of the circuit.
Gas filling	Valve corrosion.	Identified problem as material incompatibility, replaced valve with correct material.
	Accuracy and repeatability insufficient.	Designed gas filling controller to account for different filling pressures.
	Reliability: valves getting stuck after some measurements.	Installed gas filters to avoid contamination on the valves.
	Gas mixture calculation resulted in non-ignitable mixtures or abnormal combustion.	Major rework and improvement of the calculation code.
Data acquisition	Synchronization of camera with spark and injection trigger not repeatable.	Caused by limitation of the original data acquisition system. Replacing this system and rewiring all electric wiring resolved the hardware problem.
	Original software could not be used with the new hardware.	Reprogrammed the test-bench. Automated as much as possible to avoid operator error and inconsistencies.
Optical setup	Perfect alignment of camera not possible.	Added tilt and roll degrees of freedom to allow image alignment.
	Overexposure during reaction.	Available optical filters were unable to filter noise acceptably. After spectrum analysis, the optical filter could be optimized.

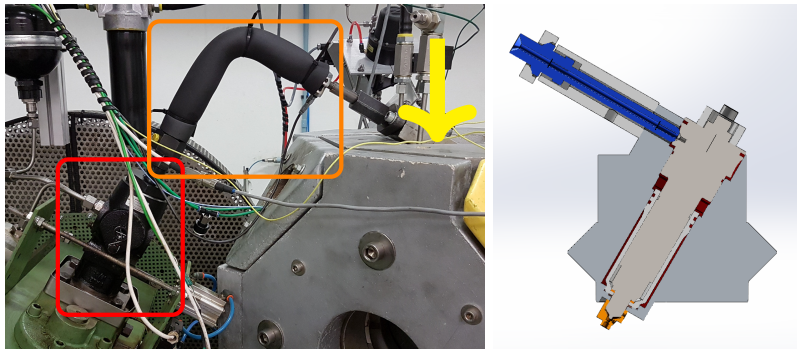

(a) Indicated from left to right: pump, line and injector mounting piece.

(b) Injector mounting piece. Oil (red) circulates around the injector assembly.

Figure 3.3: View of the PLN injection system.

A low pressure fuel circuit is connected to the high pressure pump. Fuel temperature is controlled by heating a fuel tank indirectly and continuously circulating the fuel at low pressure through the high pressure pump. By circulating the fuel, the high pressure pump also achieves the correct temperature. The fuel tank sits in an oil bath to avoid high local wall temperatures from the heating elements to the fuel that could change its composition by thermal breakdown.

The injector temperature is also controlled by oil: the injector is mounted into the chamber by an injector holder (Figure 3.3b). Oil (red in the picture) is circulated between the holder and the injector for the largest part of the injector. Seals are made at the top and close to the nozzle to condition the temperature of the complete injector assembly properly. The chamber is heated electrically to prevent water and fuel condensation on the windows. The oil heats up by contact with the heated chamber and continuously circulates through a cooling radiator. The electric fan on the radiator is Pulse Width Modulated (PWM) by a proportional integral derivative controller (PID-controller) to adjust the cooling power and obtain a constant injector temperature.

Pump Line Nozzle

The camshaft of the high pressure pump is electrically driven by a motor connected to a frequency drive to regulate the speed. During the injection the pump demands a very high power and a speed drop is prevented by a large flywheel which was sized in [65]. On overview is shown in Figure 3.3a: the high pressure line (center) connects the pump (left) to

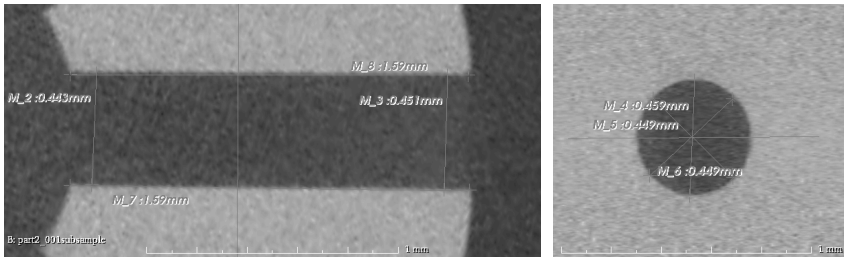

(a) Diameter and Length (b) Roundness

Figure 3.4: CT scan of eight hole nozzle. Values which are difficult to read in the images are shown in Table 3.3.

the injector (right) and the injection pressure sensor (Kistler 4067A200) is mounted as close to the injector side as possible by a Kistler pressure clamp adapter (Kistler 6533A19), on the right-hand side of the center rectangle. The injector is mounted in the injector holder as shown in Figure 3.3b and this holder is mounted in the top 'glass' opening (Figure 3.2). The high pressure inlet is shown in blue: the high pressure line is connected here. Finally, the injector assembly was modified [67] to house a hall effect needle lift sensor (Wolff ASM).

CT scan

Several nozzles were scanned with a CT scanner to obtain the inner dimensions of the nozzle holes. The scanner slices the nozzle in small two-dimensional surfaces. From these surfaces a three-dimensional object can be derived by stitching the slices back together in a slicer software [73] which was originally developed for medical imaging. By entering the resolution in all directions in the software, the dimensions of the nozzle hole can be measured on the 3D model. The results of the eight hole nozzle are shown in Figure 3.4: the sac volume is shown on the left which means that flow goes from left to right. The nozzle has straight, circular holes with limited divergence from inlet to outlet and the inlet port on the left is not rounded to improve flow. The length over diameter (L/D) ratio is 3.53. Results for the other nozzles are similar: they have cylindrical nozzle holes with no inlet rounding and low L/D ratio.

Comparing these results to the 'spray A' test nozzle that is used in ECN, some important differences can be identified: obviously the diameter, but also the convergence, inlet rounding and L/D ratio differ. The data is summarized in Table 3.3. Due to its geometry, the 'spray A' nozzle will be less sensitive to cavitation as the nozzle hole converges and the

Table 3.3: Comparison of spray A nozzle to a marine nozzle

	Spray A	Eight hole nozzle
diameter	0.09	0.44
rounding	hydro-erosion	No rounding
convergence	$K = \frac{D_{in}-D_{out}}{10} = 1.5$	$K = \frac{443-451}{10} = -0.8$
L/D ratio	11.1	3.53

entry of the nozzle hole is rounded by hydroerosion. A measure for the convergence of the nozzle hole is the K-factor:

$$K = \frac{D_{in} - D_{out}}{10} \tag{3.1}$$

Comparing the values between the eight hole nozzle and the spray A injector, it seems that the eight hole nozzle has a very low K-factor which would contribute to strong cavitation but this factor does not consider the diameter. Relatively speaking the nozzle diameter only increases by 1.77% for the eight hole nozzle while this is a decrease of 16.67% for the diameter of the 'spray A' nozzle. This is why the investigated nozzles are considered cylindrical.

3.1.3 Gas Filling

Ambient temperature in the combustion chamber is limited by the electrical heating elements to approximately $120°C$. To increase gas temperature to the target values a precombustion technique is used as in [50, 71, 76, 77]. To obtain the correct gas boundary conditions (density, temperature, heat capacity and oxygen fraction), several gases are filled by a gas filling system. The selected gas mixture contains a gaseous fuel and is ignited by two spark plugs located in two diagonal pieces of the combustion chamber. This increases gas temperature temporarily to the target conditions.

The initial gas mixture fractions are chosen such that all gas boundary conditions are obtained shortly after ignition. These are calculated by using the mass and energy conservation equations and setting a target gas density, target gas temperature, target gas heat capacity and target oxygen fraction of the mixture at SOI conditions. Implementation details are given in Appendix A.

The filling system consists of a gas manifold that is connected to the gas bottles, an exhaust valve, a vacuum valve and the chamber. The chamber is connected to the manifold by a gas filter and a pneumatically actuated valve. The gas filter protects the filling system from soot that might be produced during the pre-combustion and spray combustion and that would clog the filling system. Proportional valves connect the gas bottles to the manifold to provide flow regulation.

Gases are filled sequentially and obtained partial pressures are logged for analysis. When switching to the next gas, the manifold is vacuumed by a vacuum pump to prevent overfilling. After the filling procedure, the valves are closed and the filled mixture is then ignited such that during the combustion, gas temperature increases strongly. Peak pressure and temperature is higher than the target because the premixed fuel fraction needs to be high enough to allow ignition. After a cooldown period of about two seconds (depending on the exact boundary condition) the target temperature is reached, fuel injection is triggered and a spray measurement is executed.

Two problems can occur during the precombustion: *ignition failure* and a *too vigorous combustion*. Ignition failure can be explained by a range of things: dirty spark plugs, dirty gas filters, broken power supply, broken spark plug coils, bad filling accuracy or a non-ignitable gas mixture of which all but the last can be solved by replacing or cleaning components. The gas filters have a pore size of $15\mu m$ which protects the filling system very well, but certain experiments produce soot that deposits on the filter. This results in a higher pressure loss over the filter during the next gas filling routine which decreases accuracy.

Some gas mixtures are difficult to ignite because of reactivity reasons: the mixture is theoretically able to achieve the target condition but it does not react in the given concentrations: the oxygen concentration together with the fuel concentration does not support combustion. To identify this problem two quantities are calculated: the Lower Explosion Limit (LEL) and the Limiting Oxygen Concentration (LOC). The LEL is the lowest fuel concentration that can be ignited in air at standard ambient conditions and the LOC is the minimum oxygen concentration that is necessary to obtain ignition at any fuel concentration. When the oxygen concentration is near the LOC the LEL increases, i.e. more fuel is necessary for ignition at lower oxygen concentrations. Once fuel concentration is above LEL and oxygen concentration is well above LOC combustion will always happen easily.

The other problem is a too vigorous combustion: combustion happens uncontrolled, pressure rise rate is too fast and even knocking combustion occurs in the end gas. The result of such a combustion is shown in Figure 3.5. The rupture plate that protects for excess pressure opened as

(a) Glass in the gucci setup (b) Unmounted

Figure 3.5: Glass damage after knocking combustion in the GUCCI

intended for this experiment but pressure rise rate was so fast that two windows broke anyway.

It was expected that the combustion pressure would load the glass homogeneously and that this would result in compression forces on the inside of the glass. The damage was located on the inside of the glass as distinct arched lines close to each other which makes it difficult to understand, as quartz glass has a high compressive strength and low tensile strength. Additionally, the glass was mostly damaged in the bottom right corner as shown in Figure 3.5a. This is the furthest away from the spark-plug and contains end gas for the longest time. Only a pressure gradient perpendicular to the window can induce local tension which can explain the damage. As most of the damage was located close to the end gas, knocking combustion was thought to be the cause of the problem.

This experiment was executed during the search for reacting conditions: gas concentrations were calculated to end with 21% oxygen. For the first experiment, the oxygen concentration was reduced by reducing the target filling pressure because it was thought to be safer to increase the oxygen concentration gradually to protect the setup. During this experiment, no images were taken on purpose to protect the camera and saving the measurement data failed unexpectedly: the only thing left from this experiment was a screenshot from the controller software: Figure 3.6. Pressure is shown as a function of time, with time indicated as the sample number at a sampling rate of 5000 Hz. Chamber pressure increased very quickly from zero to 80 bar (almost invisible on the graph) and the rupture plate opened to protect the chamber, chamber pressure

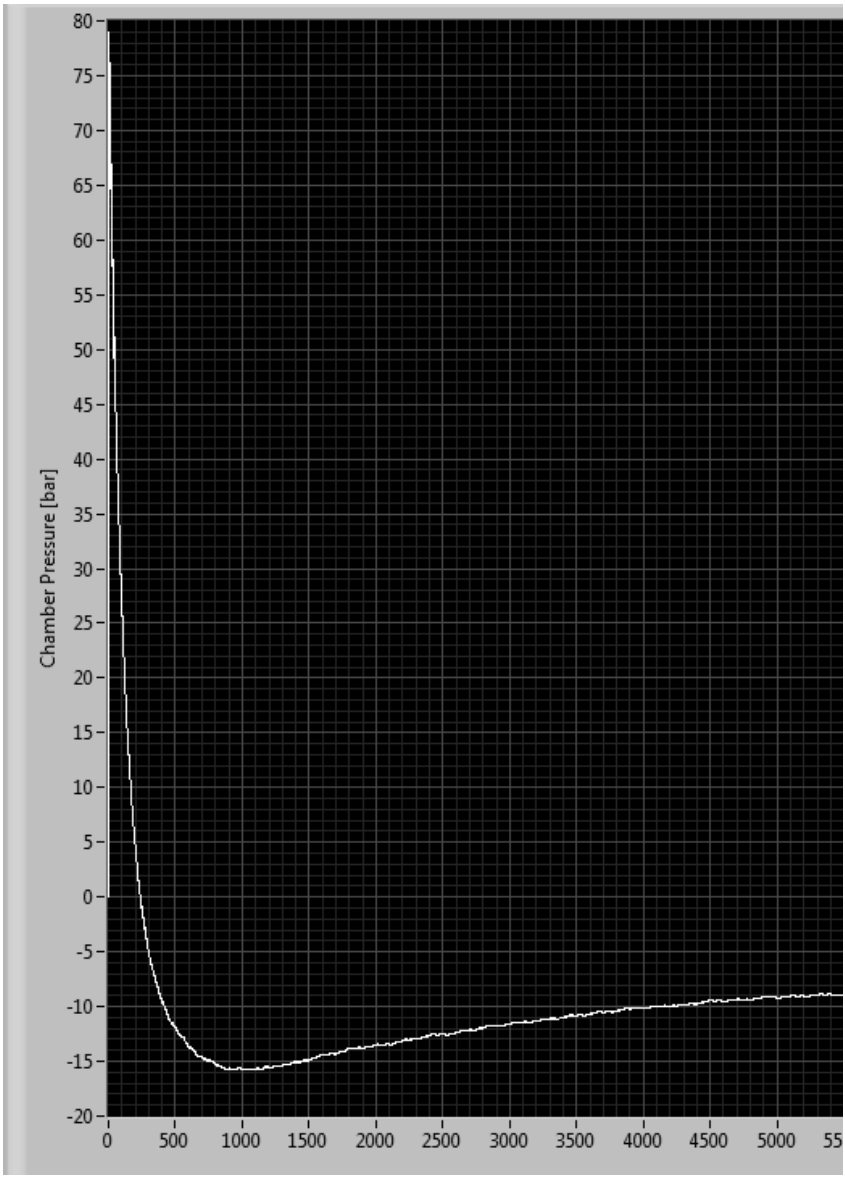

Figure 3.6: Screenshot of the pressure in the control software, the pressure sensor measures pressure increase since the start of the experiment. This results in negative relative pressures when the rupture plate opens, as the total cumulative filled pressure still needs to be added.

was back to atmospheric in a period of under $\frac{500 samples}{5000\,\mathrm{Hz}}$ =100 ms.

To avoid auto-ignition in the future the auto-ignition delay of the mixture should be larger than the time required for the flame to travel approximately half the combustion chamber (as spark plugs are mounted on opposing corners of the chamber). To help analyze this problem the dilution ratio is defined:

$$D_{mix} = \frac{m_{Ar} + m_{N_2} + m_{O_2}}{m_{O_2,stoich}} \tag{3.2}$$

with m_x the mass of the filled gas $_x$. Two opposing effects influence auto-ignition when varying the dilution ratio from very diluted to stoichiometric mixtures: flame speed increases, but at the same time auto-ignition delay time decreases. Laminar flame speed typically increases linearly with decreasing dilution ratio [78, 79] which reduces the chance of auto-ignition because the required time for complete combustion reduces. However, auto-ignition delay time decreases exponentially when dilution ratio decreases [80]. When combining these opposing effects it is clear that a higher dilution ratio will decrease the chance of auto-ignition. This technique is also used to suppress knock in spark ignition engines: EGR is used to dilute the mixture and prevent engine knock [81].

By reducing the excess oxygen concentration without compensating with another gas, the dilution ratio decreased. Partial gas pressures were measured after filling and these are used to calculate the dilution ratio of the gas mixture: it is shown in Table 3.4 in the second to last column.

To solve the problem two adjustments were tried: the premix fuel was changed and the mixture was made leaner. The mixture composition after the premix fuel change is shown in *iteration 1* of Table 3.4: acetylene was replaced by methane because methane is very knock resistant. The effect of replacing the fuel did not solve the problem completely. Chamber pressure as a function of time after start of ignition is shown in Figure 3.7 on the left: combustion duration is very short, maximum pressure is

Table 3.4: Dilution ratio and peak adiabatic combustion pressure to obtain gas mixtures with 21% *oxygen content at SOI*

Name	C_2H_2 [*bar*]	H_2 [*bar*]	CH_4 [*bar*]	Ar [*bar*]	N_2 [*bar*]	O_2 [*bar*]	D_{mix} [−]	p_{adia} [*bar*]
broken glass	1.3024	0.0	0.0	0.483	5.825	4.528	6.3	114
iteration 1	0.0	0.0	1.17	0.95	6.81	2.75	5.6	77
iteration 7	0.0	0.0	0.87	0.38	8.28	4.54	9.4	66
C_2H_2+H_2	0.36	0.51	0.0	1.64	9.43	4.5	12.96	62

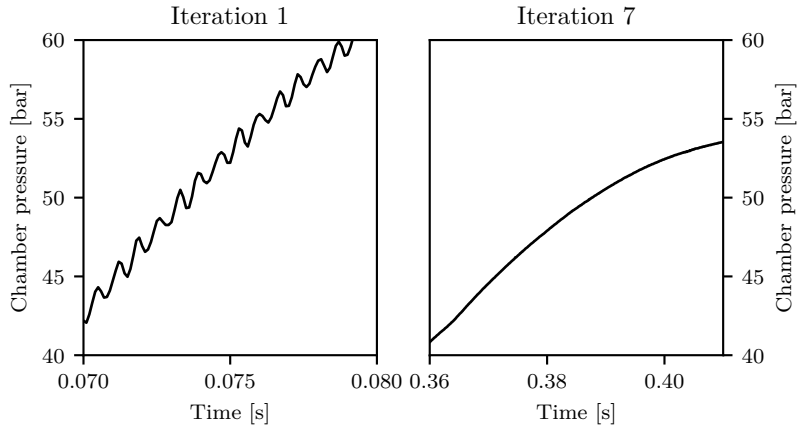

Figure 3.7: Chamber pressure after ignition for two different gas compositions: iteration 1 still shows some abnormal, knocking combustion which was also observed in the high-speed movie. Iteration 7 shows a smooth combustion. Note the much longer timescale, indicating the much slower combustion.

reached after only 90 ms and high frequency pressure waves are measured which indicates a moderate abnormal combustion.

This was also observed on the high speed camera. Normally, images start bright and the front of the combustion is visible as a darker region that moves from the spark plug to the center until the two combustion fronts meet: An example of a normal combustion is shown in Figure 3.8. However, on this particular experiment combustion started normally but when the combustion fronts came closer to each other they started to oscillate back and forth which indicates pressure waves. As shown by the dilution ratio, the oxygen concentration in this experiment was reduced without compensating with nitrogen and argon just as in the first experiment. The knock resistance of the fuel decreased knock intensity, which shows that the critical dilution ratio differs between fuels.

The final adjustment was a gradual increase in oxygen content by repeating the calculation of the mixture composition such that a reduction in oxygen fraction was compensated by an increase in nitrogen and argon. After a couple of iterations with increasing oxygen concentration the final composition with 21% oxygen after precombustion was reached in iteration 7, shown in Table 3.4 and on the right in Figure 3.7. Now, the dilution ratio is higher, combustion speed slows down (400 ms and the ignition delay is higher because of the dilution ratio. With this dilution ratio no abnormal combustion could be observed.

When the calculation was repeated for higher ambient densities with

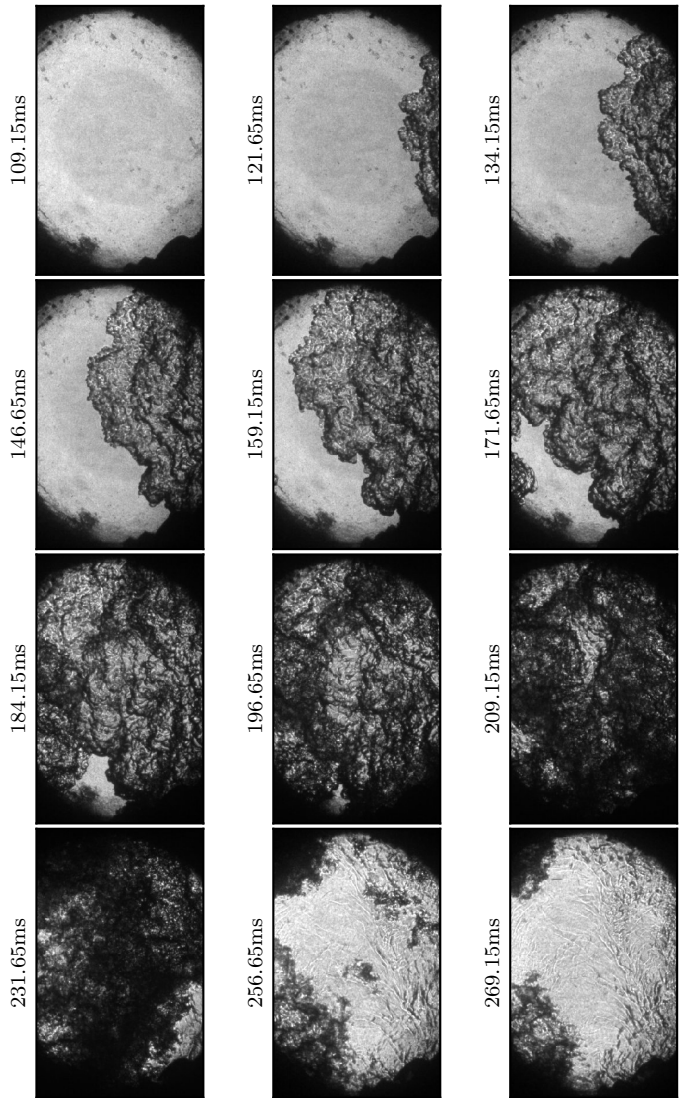

Figure 3.8: Schlieren imaging showing the evolution of normal precombustion, time after start of ignition shown on the left of each figure.

lower oxygen concentration to obtain an evaporating spray, ignition was not stable with methane, as explained before by the influence of LOC on the LEL. The fuel that was finally selected is a combination of acetylene and hydrogen. Hydrogen and acetylene have a much lower LEL than methane and a lower minimum ignition energy as well. When calculating the new mixture compositions the minimum dilution ratio was kept above 9 and the combustion remained relatively slow without knock. An example is given in Table 3.4 and all other conditions are listed with their gas partial pressures in Table A.1.

3.1.4 Data-acquisition and control

Data-acquisition and control of the test bench is done by a National Instruments compactRIO and a Labview program as a replacement for a compactDAQ system. The original compactDAQ system had limitations regarding synchronization of multiple high speed signals and to remove these a new system was implemented.

The compactRIO system exists out of a chassis and I/O modules, the chassis contains a Field Programmable Gate Array (FPGA) chip and embedded controller that interfaces with the FPGA chip. The I/O modules provide digital and analog input and output channels to connect several sensors and actuators.

Once all sensors (e.g.: chamber pressure and temperature) and actuators (e.g.: inlet valves, heating elements) are connected to the controller through the appropriate I/O module the software program can start to read sensor values, prepare the test bench for a measurement and finally execute the measurement.

The software program is built out of several components: the graphical user interface (GUI) on the host computer, the controller software and the FPGA program on the target computer. The GUI is started by the operator and contains software buttons to interact with the setup: experimental parameters can be set (e.g.: the engine speed, recording frequency, gas filling concentrations) and after a final manual validation of the boundary conditions an automated experiment can be started.

The target computer is the CompactRIO system with two processing units: a real-time operating system for communication and signal processing and an FPGA for high-speed control, custom timing and data acquisition directly in hardware. This is the main difference between the compactDAQ and compactRIO system: the timing and synchronization in the compactRIO can be set up freely while the compactDAQ is limited to four high speed signals which was not enough to properly configure the whole synchronization. The real-time system is used to process GUI

inputs, prepare the setup semi-automatically for a measurement, trigger the FPGA to do a measurement and then transfer the data from the measurement back to the GUI for the operator.

The FPGA system provides low level access to the I/O: inputs are read and outputs are set through this system. The FPGA chip is programmed in hardware which means that its outputs are available instantaneously: customized triggering is implemented to obtain a reliable activation of the PLN actuator, synchronization between sensor sampling and camera triggering is also done by the FPGA chip.

A high-level overview of the control software is given below:

Slow tasks The controller executes a number of slow tasks:

- Control and check temperature of
  - Fuel
  - Chamber
  - Injector
- Update experimental parameters in the FPGA: e.g. engine speed, precombustion delay time, sample frequency, …
- Update the status of digital in-, and outputs: e.g. valves, motors, …
- Read in analog data from the FPGA for logging purpose
- Gas filling procedure

Spray measurement High speed tasks such as a spray measurement require synchronization between the sensor data acquisition, camera and LED sampling, spark ignition and activation of the pump actuator for exactly one revolution. This is done by creating one high speed synchronization pulse train when the measurement starts. This synchronization pulse train is then subsampled by the different tasks to obtain multiple synchronized sampling speeds. This is shown in Figure 3.9. Analog sampling occurs at rising and falling edges of the camera pulse train while the camera only records a frame on rising edges. The LED pulse train is synchronized at exactly half the camera frequency because two different LEDs are used (explained further in the text). One lights up at rising edges and the other one at falling edges. Finally, the spark and actuator signal are only synchronized at the start of the experiment: the mixture is ignited after a time delay and the actuator is enabled for one camshaft revolution after the cool-down period.

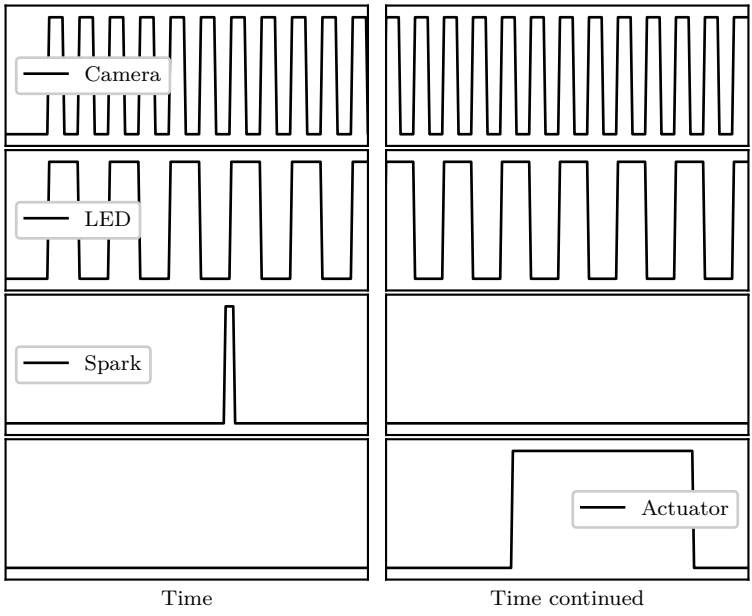

Figure 3.9: Synchronization between camera, LED, spark ignition and the actuator for a typical spray measurement. The measurement sequence starts on the left hand side with the start of LED and camera activation. The camera records twice as quick as the LED pulse train to capture two different images. Then the spark is triggered. After a cooldown time (indicated by the split in the plot), the actuator is triggered and images of the spray are recorded.

3.2 Optical techniques for high speed imaging

Over the years multiple optical techniques were developed to visualize different parts of the spray [82]. In this work high speed schlieren visualization is used to detect fuel vapor together with a Mie scattering technique to visualize liquid droplets. These are recorded by one camera with the frame straddling approach: each frame of the schlieren technique is alternated with a Mie scattering frame.

3.2.1 Schlieren

The chamber is equipped with three large quartz windows (150mm diameter) for optical access to the spray. In this work vapor and liquid penetration of the spray are measured with a high speed camera: a schlieren technique is used to measure gas penetration and spreading angle. The schlieren effect consists out of deflection of light rays which is caused by gradients of the refractive index in the medium. This refractive

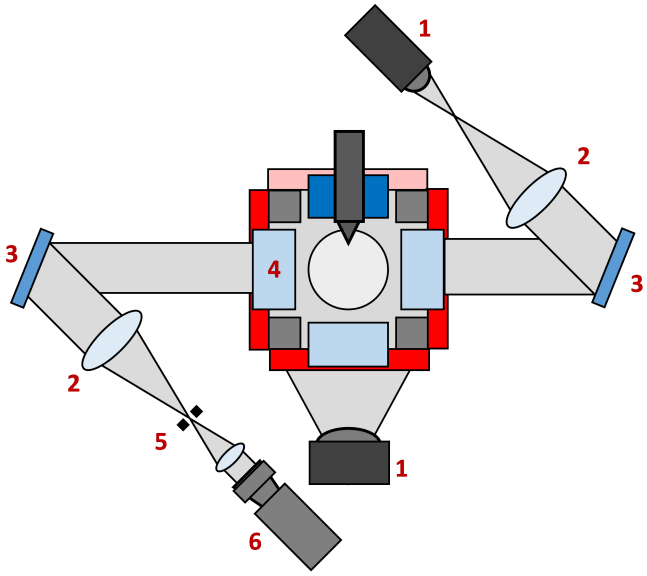

Figure 3.10: Schematic view of schlieren and Mie scattering techniques. Schlieren collimated light beam generated by an LED (1, on top) through collimating lens (2), reflected by a mirror (3) into the chamber through the optical windows (4). The camera (6) then captures the light passing through the schlieren stop (5). The Mie LED (1, on bottom) illuminates the droplets.

index varies linearly with density according to the Gladstone-Dale relation [83] which makes the schlieren technique perfect for visualizing density gradients from evaporating fuel, even fuel vapor has a sufficiently high density gradient with ambient air to deflect light rays. Several authors [84], [85], [86] have used this technique to visualize fuel sprays with good results.

The lighting consists of a collimated light beam which is formed by a green LED light source that is focused into a pinhole to provide a point light source. This point light source is then placed at the focal length of a 160 mm diameter lens (f1200) which results in a collimated light beam of 160 mm diameter. This beam is then guided through the test section by a mirror. After the test section this light beam is reflected into the direction of the camera by a second mirror and is focused again with a similar large lens (f1200) on the sensor of the high speed camera. This Z-type schlieren setup is shown in Figure 3.10. Refracted light is prevented to enter the camera lens by placing a schlieren stop in the focal point right before the camera. The aperture of the camera lens was used as the schlieren stop by placing it slightly closer to the focusing lens. By adjusting the aperture, the sensitivity can be changed.

3.2.2 Mie scattering

Mie scattering imaging is used for liquid phase detection. Liquid droplets are illuminated by a LED light source, mounted perpendicular to the schlieren optical axis (Figure 3.10) and scattered light from these droplets is captured with a camera. Mie scattering is frequently used in literature [49], [51], [87]. In this work a large LED array was used to illuminate the test section homogeneously.

3.2.3 Optical filtering

To minimize natural luminosity of the combustion an optical band-pass filter that was matched to the spectrum of the LED is placed directly before the camera lens. The signal of the LED light source was measured by an optical spectrometer (AdvanTest Q8381A) and the spectrum is shown on the bottom left of Figure 3.11. Several optical filters were tried with different filtering performance: one Standa filter with a Gaussian transmission characteristic. This characteristic provides a maximal throughput at the center frequency with a roll-off that is specified by the full width at half maximum (FWHM) value (the width of the filter measured between the points where the transmission is half of the maximum). Two filters from Thorlabs were also considered: these are band-pass filters with a center wavelength and a constant transmission

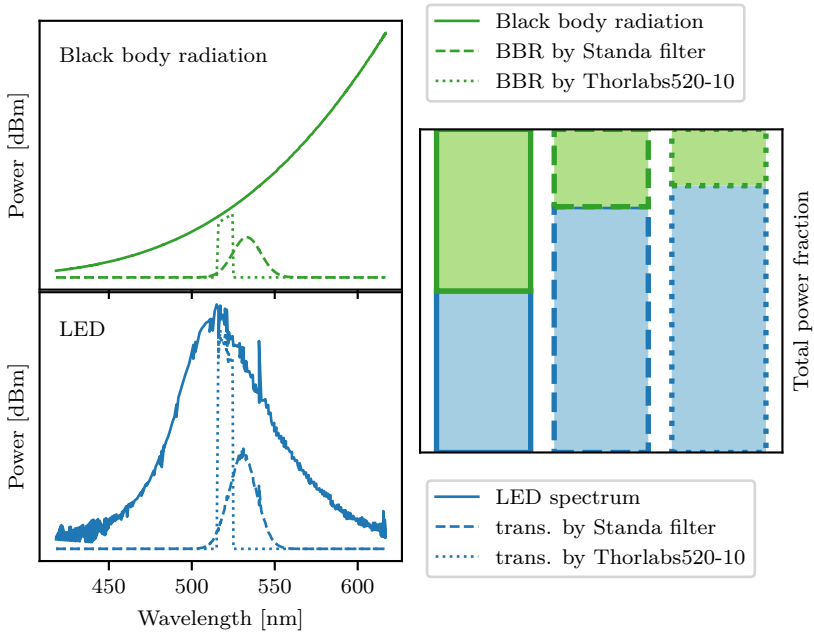

Figure 3.11: On the left: spectra of the LED signal (bottom) and black body radiation (top), before and after optical filtering. On the right: relative power integrated over the visible spectrum of the LED signal (blue) and the black body radiation (green).

for the complete filter band. The center wavelength is chosen as 520 nm and two different widths are considered: 10 nm (Thorlabs520-10) and 40 nm (Thorlabs520-40, not shown in the graphs). The theoretical output spectrum from LED and filter combination is calculated by multiplying the LED spectrum with the theoretical transmittance of the filters. It is shown for the first two described optical filters in the figure.

To investigate the effect of the filter on the signal quality the signal to noise ratio is estimated. It is assumed that optical noise is mainly generated by soot luminosity from the pre-combustion and diesel combustion. The spectrum of soot luminosity is calculated by assuming black body radiation such as found in [88] and applying Planck's law.

The spectrum of black body radiation with a constant temperature of 2000 K is shown on the bottom left of Figure 3.11. When this temperature would decrease, the spectrum moves towards higher wavelengths. Higher soot temperatures would result in a spectrum that shifts to lower wavelengths. The temperature is kept constant during this estimation,

as only relative improvements are considered.

Finally, the total optical power is calculated by integrating the LED and noise spectra over the visible spectrum: the fraction of LED and noise power are shown on the right of Figure 3.11. The noise power without filtering was set equal to the LED power to obtain an initial signal to noise ratio of one. Filtering with the Standa filter resulted in a signal to noise ratio of 3.18, but at approximately the same transmitted LED power the signal to noise ratio with the Thorlabs520-10 filter increased to 4.75. Because of the improved signal to noise ratio this optical filter was chosen. The transmitted LED power is only 10 % of the input LED power because the filter is very narrow but this was necessary to reduce soot luminosity enough.

3.2.4 Optical techniques combination

One line of sight technique (e.g. Schlieren) and one perpendicular technique (e.g. Mie scattering) are combined by the frame straddling approach: the schlieren and Mie LED light sources were alternately activated at half the camera frequency to acquire both optical techniques with one camera during each experiment as shown in Figure 3.9. Images were recorded at a speed of 20 kHz and a resolution of $460 \times 288 px$ by a high-speed camera (PCO DiMax). Exposure time was kept constant at 5 µs during the experiments and was determined by the electronic shutter (gate) of an image intensifier (Lambert Instruments HiCATT).

Mie scattering results in a lower image intensity compared to schlieren imaging: the schlieren stop determines the sensitivity of the system by choosing how much light enters into the camera lens. When adjusting the size of the schlieren stop in a combined Mie scattering and schlieren measurement this schlieren stop causes a mismatch in sensitivity change. The light throughput of the Mie experiment diminishes faster than the schlieren light throughput when the diameter of the stop is decreased. This is caused by the perfect alignation of schlieren lighting that makes it insensitive to diaphragm size; without disturbance in the measurement section all light would go through the diafragm because this is placed in the focal point of the focusing lens. On the other hand, light from Mie scattering is not perfectly aligned to the focusing lens which means that it is sensitive to the diaphragm. This is shown in Figure 3.12: light from the collimated schlieren beam is focused perfectly into the diaphragm and the size of the diaphragm does not influence the average schlieren intensity much. In the bottom image a droplet that scatters light in the test section is shown: this acts as a point light source and is highly sensitive to the diaphragm size. Some light rays are drawn through the focusing lens and when the diaphragm is closed more, Mie scattering

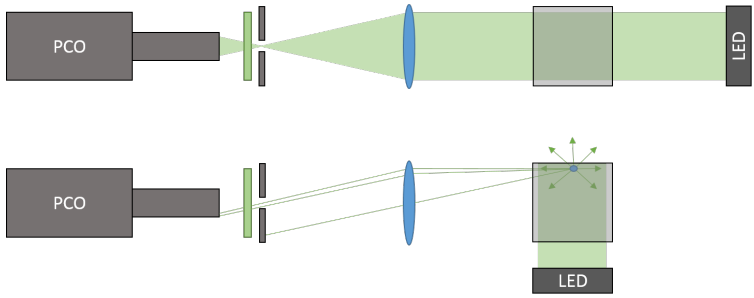

Figure 3.12: Diaphragm influence on the optical combination of schlieren (top) and Mie scattering (bottom) techniques

intensity decreases directly.

To solve this mismatch, the optical efficiency of the schlieren setup was deliberately reduced by moving the focus point of the LED light source slightly away from the pinhole. This results in a reduced throughput in the collimated light bundle in the schlieren setup which is closer to the Mie intensity. An external diaphragm was not use: to avoid loss of light of the Mie scattering technique, only the diaphragm of the camera lens was used. Image intensity was then improved with an image intensifier for both techniques at the same time. To avoid overexposure and damage to the camera sensor, the schlieren intensity still limits the maximum gain of the intensifier.

3.3 Spray detection and spray metrics

After images have been acquired by the high speed camera they are processed to obtain spray parameters such as penetration length, spray angle and liquid length.

For image analysis, schlieren and Mie images were processed separately because of the distinct difference between the two techniques. Schlieren images show a dark spray upon a highly non homogeneous background with a relatively high contrast ratio whereas Mie images show a bright liquid spray on a homogeneous background but with a very low contrast ratio. Images were processed in several steps:

- Images were rotated until the spray axis was horizontal, the nozzle hole was positioned on the left meaning that the spray traverses from the left to the right side.
- Contrast enhancement to provide a consistent image for subsequent processing
- Spray detection: detection of either vapor or liquid in the image
- Spray metric calculation: determine key spray parameters based on the detected spray

3.3.1 Pre-processing

After rotation and positioning, contrast enhancement was used for the schlieren images: a histogram of image intensity was calculated. Image intensity was scaled around 40 % of the maximum histogram value, shown in Figure 3.13 with dotted vertical lines. This essentially means that 10 %

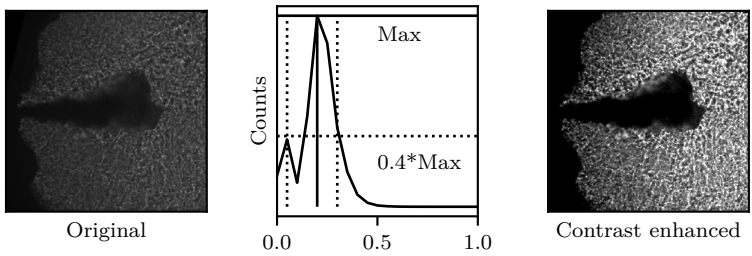

Figure 3.13: Contrast enhancement illustrated on a schlieren image. The histogram of the original picture is shown in the center. The maximum histogram value is detected and intensity is scaled to around 40 % *of this maximum.*

of either the lightest and darkest intensity pixels of the images is removed and the rest of the intensity is scaled without loss.

Reacting measurements were additionally adjusted by a soot luminosity correction. After the ignition delay, soot luminosity starts to appear in the whole spray. This reduces the contrast of schlieren images which makes boundary detection impossible. As soot luminosity is independent of LED illumination, it appears in both the schlieren and Mie images and is only separated by one frame in time. The schlieren image at time t was thus corrected by subtracting the Mie image at $t + 1$ from it. All pixels in this Mie image larger than one certainly belong to the vapor spray, as the Mie image contains information regarding both liquid length and soot luminosity. To avoid calculation problems, all pixels from the resulting image with a value smaller than zero were limited to zero.

Mie images were recorded with the same camera and exposure settings as the schlieren images and even after optical improvements this resulted in relatively dark images. Liquid length is typically determined as the maximum distance from the nozzle to a point with an intensity of at least three percent of the maximum image intensity. In [49] a gated intensified camera with a gate (exposure) time of 3ms was used to acquire a time-averaged liquid length. Because the exposure time was very long, very high maximum intensities were achieved. Time resolved measurements with a much shorter exposure time result in a lower maximum intensity and this intensity was scaled to the maximum possible image intensity by choosing a target threshold intensity from the measurements. This threshold was chosen as the maximum intensity for every experiment.

3.3.2 Schlieren detection

The spray contour is extracted from the schlieren images with a dedicated edge detection algorithm. First, a background correction is done. The background image exists out of small temperature and density vortices, which are created during the precombustion. When studying evaporating spray these vortices look very similar to the spray after evaporation [85]. Payri et al. proposed a successful strategy to remove the background as much as possible, which will also be applied here [51]. The background image is initialized with the first image. The background for the next timestep is then determined dynamically. Only the area of the background that was not within the currently detected spray area, is updated with the current image. The rest of the image pixels is not updated which means the background image always consists out of the most recent available background pixels.

The schlieren edge detection method in this work is a combination of morphological filters to further smooth background noise, while

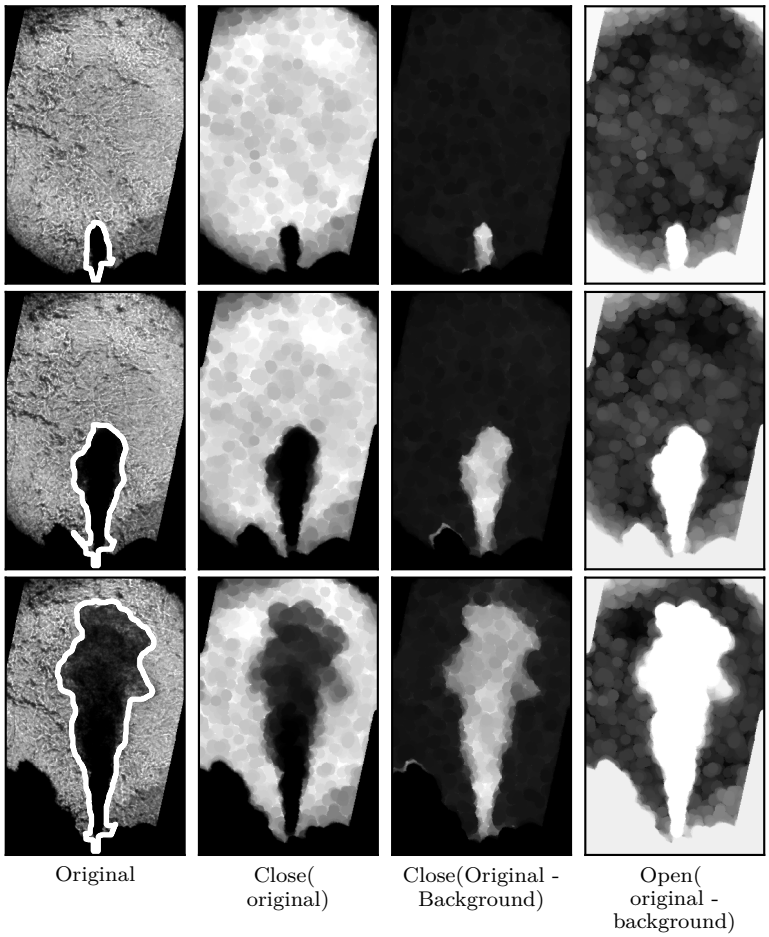

Figure 3.14: Spray detection on schlieren image with morphological filters.

retaining the spray information. A combination of the original image and the background-corrected image was used because the original image contains information about the optically dense region of the spray, while the background-corrected image mainly contains the furthest spray penetration.

This is shown in Figure 3.14. The original image for three different times after SOI is shown on the left. On the second position the morphological closing of the original image is shown. A morphological closing is used to remove black spots smaller than the opening element from the image.

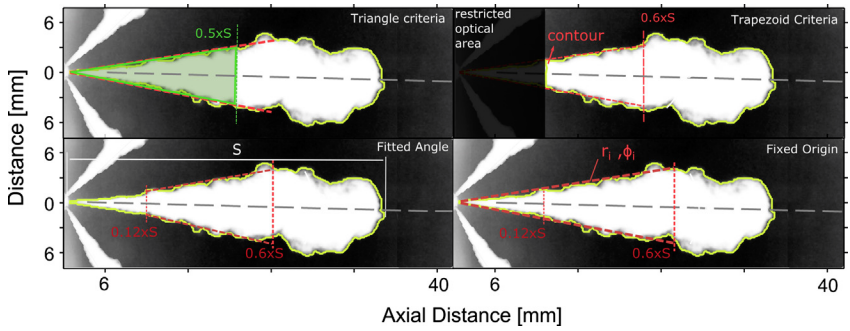

Figure 3.15: Spray spreading angle definitions: detected spray angle is show in red, while the spray contour is green. Taken from [51]

In this case a disk (filled circle) with $8px$ diameter was used. This image provides an indication of the optically dense part of the spray, but lacks sensitivity for the evaporated region. On the third position the closing of the background-corrected image is shown. This image shows a higher intensity in the moving part of the spray, also in the evaporated zones. These image are combined into one as: $Open[image - background - Close(image) + Close(image - background)]$. The resulting image is converted into a binary image by Otsu's thresholding. This method minimizes the sum of interclass variance [89].

The spray boundary is then processed to obtain a spray angle and penetration length. Over time, several definitions have been employed to extract the spray angle from the detected contour:

1. **Triangle** An isosceles triangle is built with a height of half the spray penetration and an area equal to the spray area from the nozzle's exit until half the penetration. The spray angle is then measured between the two sides with equal length. This definition was described in [47].

2. **Trapezoid** This definition is similar to the isosceles triangle but it is adapted for boundaries where the spray is not available near the nozzle, e.g. the start of the spray is not visible because the window cannot be placed close enough. The angle is measured between the two equal sides of an isosceles trapezoid with the same area as the spray. The trapezoid is built after the restricted optical area until half the penetration.

3. **Fitted lines between intervals** Two lines are fitted to the contour of the spray, in [51] starting at 12 % and ending at 60 % of the spray penetration. The angle between these lines is the spray angle. The

lines might not intersect at the orifice, so the origin of the spray is not taken into consideration. This method is also used in [34, 44] to analyze the spray angle of microscopic imaging: the camera focus was now on a region close to the nozzle hole. The fitted interval was now very close to the nozzle hole, between 0mm and 5mm from the hole.

4. **Fixed origin** The origin is put onto the nozzle orifice and two lines are fitted by calculating a weighted average of the points from the origin until 60 % of the penetration of the contour defined in polar coordinates.

The four methods are compared visually in Figure 3.15. The triangle method is limited because of its sensitivity to the detected spray region close to the nozzle hole. In literature this method is left out for its lack of robustness [51]. The other methods give similar results as can be seen in Figure 3.16: the spray angle is shown for 7.6 and 15.2 $\mathrm{kg/m^3}$ ambient density after processing with the different methods. The needle opening and closing is shown by vertical dashed lines. It can be noted that the first part of the angle does not make much sense: when the penetration length is not high enough the definitions that force the fitted lines to go through the origin measure a very high spray angle, this was also observed in [51]. The trapezoid and fixed origin definition suffer from this problem strongly whereas the fitted line approach converges quickly to a normal value. No steady state value is reached which could also not be expected as the injection pressure and velocity are not constant because of the PLN injection system.

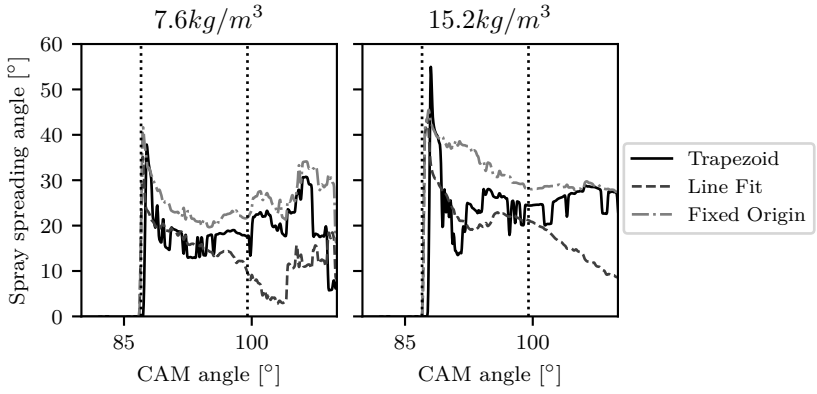

Figure 3.16: Spray spreading angle plotted as a function of cam angle for the different detection methods, (n-Dodecane fuel, 850 K, 800 rpm*).*

In Figure 3.17 samples of the recorded images are shown with the detected spray boundary and fixed origin and fitted lines spray angles on top. Here the difference between the angle definitions becomes more clear. As the spray already has a certain width when it emerges from the nozzle hole the fixed origin method measures a bigger spray angle than the line fit approach because it is forced to go through the injector nozzle hole center. Initially, the line fit approach shows a better correspondence to the detected boundary. During 'steady-state' (around 94° CA), the detection agrees quite well and both methods can be used to measure spray angle. After needle lift closure (around 94° CA), the spray boundary becomes unclear and the spray angle is not clearly defined anymore.

Optical sensitivity and image processing routines can affect the calculation of the spray spreading angle as showed in [90, 91]. It is certainly possible to compare trends, but the actual value of spray angle depends too much on the configuration of the test bench to compare spray angles from different test benches.

In the rest of this work, the line-fit method is used as this provides the most robust detection. It is insensitive to the boundary close to the nozzle hole in the beginning of spray development while it still matches the spray boundary near the end of injection well.

Finally, the spray penetration length is defined as the distance between the nozzle and the furthest pixel from the nozzle that still lies on the detected spray boundary.

3.3.3 Mie scattering

Liquid penetration was determined with three different methods: the furthest pixel with three percent of the maximum intensity (as described in literature [49]), spray boundary detection and an intensity fitting approach. Examples of the detected liquid lengths are shown in Figure 3.18. The complemented Mie image is shown for the three detection methods: on the left the boundary detection method as in [51]. The liquid length is determined as the furthest pixel from the origin in the detected boundary.

In the middle, the average intensity over a window of 30 px around the spray axis is shown. This intensity shape looks identical to the extinction profile of diffuse back illumination images in [71] and [50]. The intensity increases gradually up to a certain semi-constant value when the distance to the nozzle increases because of increasing spray width. Average intensity drops very quickly after a certain distance, this drop is detected in software and the decline is fitted with a straight line. The distance at which this fitted line crosses zero is defined as the liquid

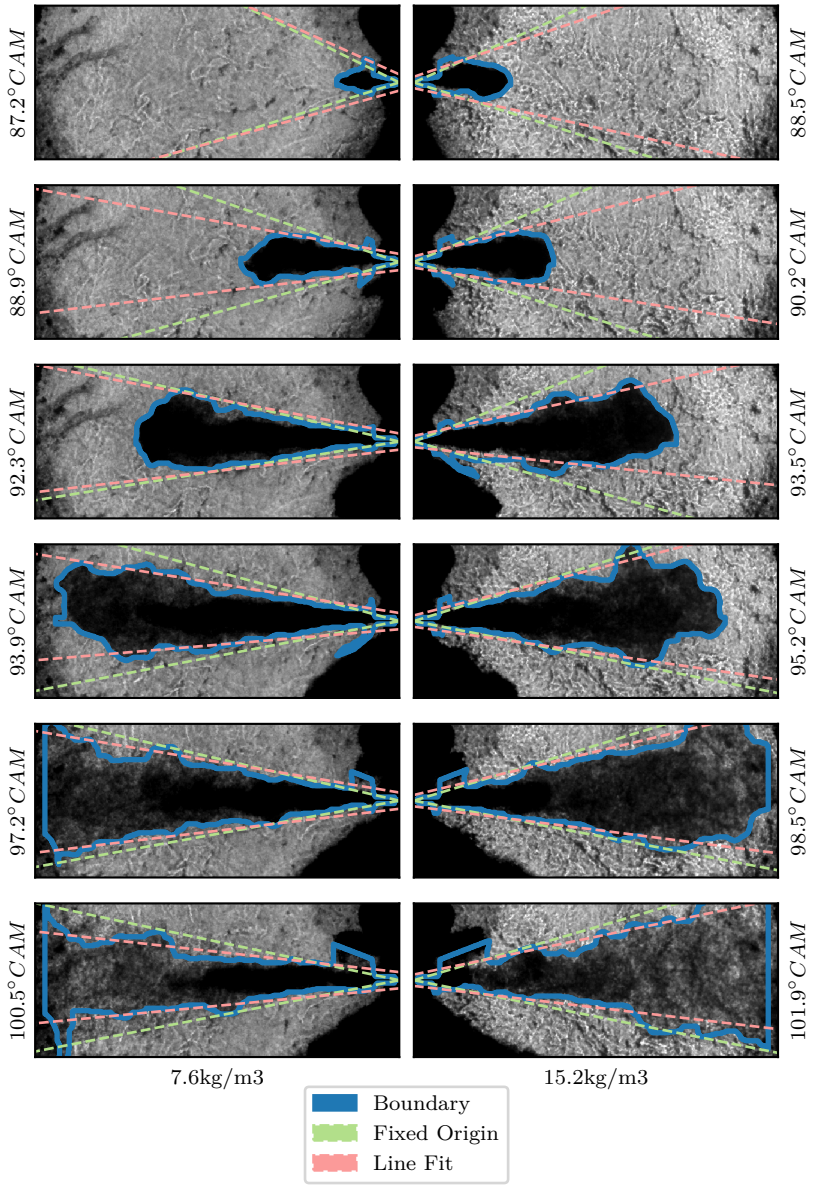

*Figure 3.17: Spray spreading angle plotted for **fixed origin** and **fitted lines** processing on several stages of the spray, (n-Dodecane fuel, 850 K, 800 rpm). The fixed origin method is much less sensitive to perturbations close the nozzle hole.*

length. On the right of Figure 3.18 the three percent of maximum image intensity is shown.

Detected liquid length as a function of crank-angle is shown for 7.6 kg/m^3 (left) and 15.2 kg/m^3 (right) for the three different processing techniques in Figure 3.19. For the lowest ambient gas density, detection results vary significantly: near EOI liquid length has a value from ±38 mm until ±69 mm depending on the technique.

By investigating the images, it was found that large structures detached from the spray core during experiment with the lowest ambient density. The DBI method detects the spray intensity decrease, starting from the maximum intensity. When a large structure detaches image intensity locally decreases which is detected as the liquid length. The spray detection method could suffer from the same problem, but this was avoided by combining large detected structures into one spray during processing. The three percent method detects the furthest pixel of the spray and does not account for local intensity decrease which avoids this issue completely.

For the highest density, detaching structures are not observed and the methods provide a better agreement. The DBI method is still the most sensitive, additionally the argument of a calibrated liquid length for the DBI case does not hold here, because the images do not result from an extinction measurement, rather they are generated by complementing a contrast enhanced Mie image. The DBI detection is discarded for further processing.

While theoretically the detection method could provide more stable results because of the fitting approach which provides some insensitivity to local image intensity changes, the results are comparable. For the following measurement analysis, the 3% detection is used for two reasons. It provides the highest dynamic range, i.e. the difference between highest and lowest lengths is higher, which makes interpreting results easier. Secondly, it is the most widely used detection technique in

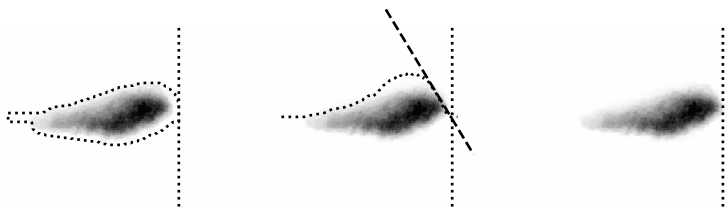

Figure 3.18: The same Mie (complemented) image shown for three processing techniques: Spray boundary detection (left), Spray axis intensity (middle), three percent maximum intensity (right).

literature which makes direct comparison with reported liquid lengths more realistic.

3.3.4 Data averaging

The data that will be reported is all ensemble averaged. Measurements were repeated at least five times, processed by the above described routines and then averaged on a crank-angle basis.

As will be shown in the next section, gas conditions at SOI with a good repeatability are obtained, but when analyzing initial results outliers in all obtained spray parameters could sometimes be observed. The reason for this lies in the measurement, ranging from LED malfunction to residual fuel that makes the pre-combustion slightly too rich which results in soot production and decreases optical transmission.

This is why manual validation was necessary and some measurements were completely discarded. The processed results of individual measurements are shown in Figure 3.20 on the left. One measurement differs from all the others while the remaining ones show a better correlation. In this case the problem was visually confirmed to be caused by low light throughput because of a rich pre-combustion. This was the first measurement after down-time of the test-bench and residual fuel that could not be cleaned caused an richer and sooty pre-combustion.

To calculate the average and standard deviation the outlier was left out and the ensemble averaged results are shown on the right-hand side of Figure 3.20. The standard deviation of spray spreading angle and liquid

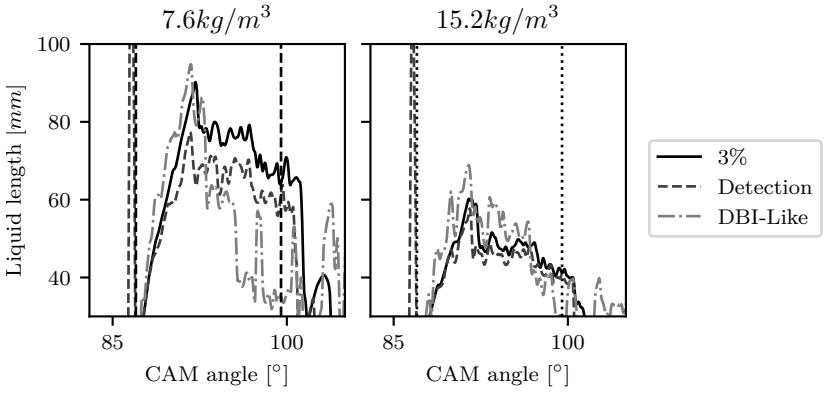

Figure 3.19: Spray liquid penetration plotted as a function of cam angle for the different detection methods, (n-Dodecane fuel, 850K, 800 rpm).

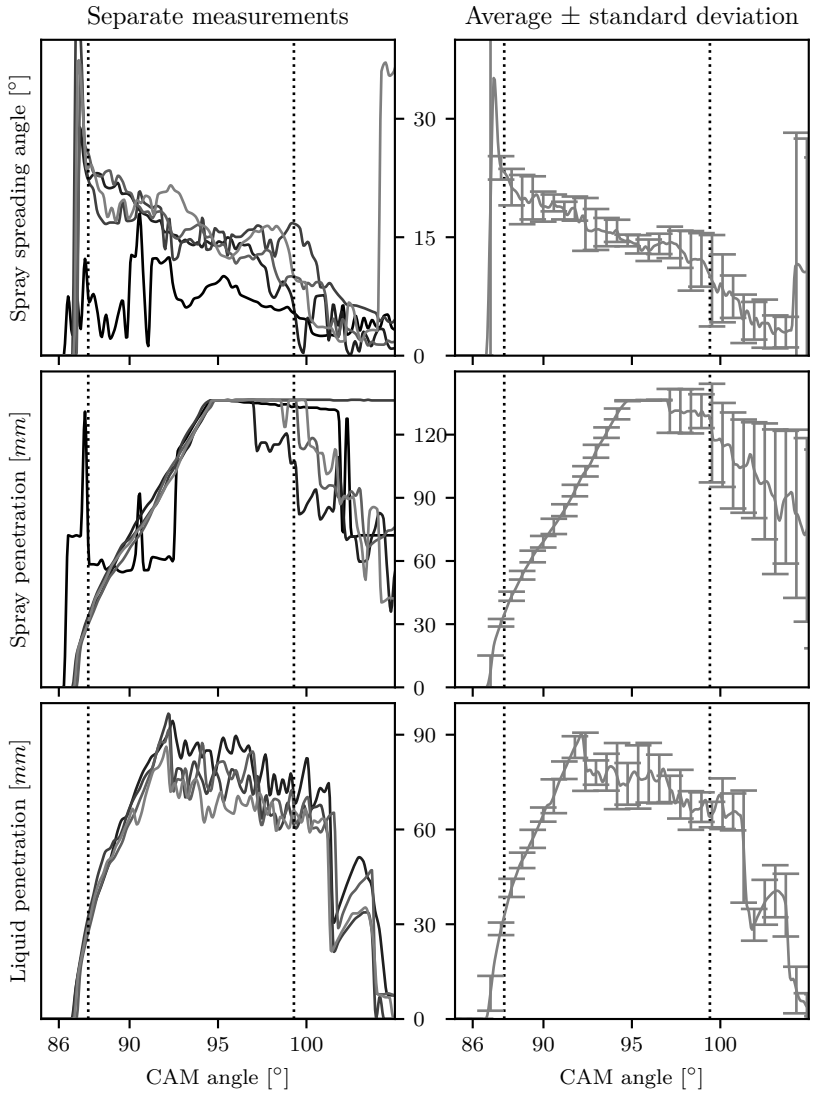

Figure 3.20: Separate measurement results shown on the left-hand side with one outlier due to optical problem, ensemble average excluding that outlier (right), SOI and EOI shown with dashed vertical lines, (n-Dodecane fuel, 850 K, 800 rpm*).*

penetration is still on the high side because of the transient injection process.

For a part of the measurement analysis in Chapter 4, time-averaged values

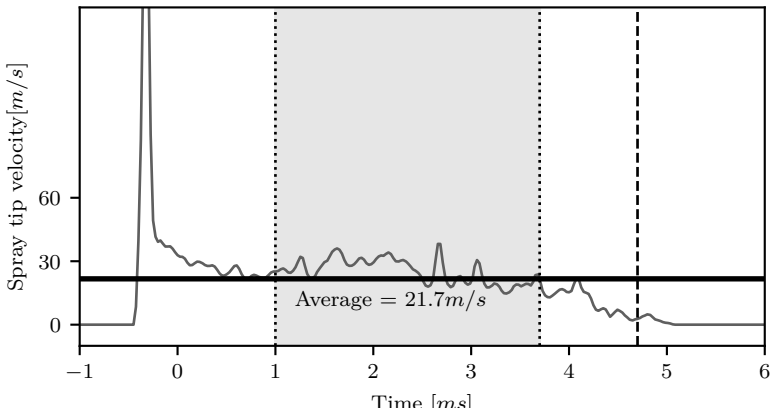

Figure 3.21: Spray tip velocity as a function of time after SOI with EOI indicated (dashed lines) and the steady state period (between dotted lines), (n-Dodecane fuel, 850 K, 800 rpm*).*

are also calculated for every measurement condition. A semi-steady state can be observed for spreading angle and liquid length in Figure 3.20. The spray vapor velocity (calculated as penetrated distance over consecutive frames) also shows this steady state behavior.

This steady state period is calculated by detecting the SOI and EOI, based on needle lift, and assuming that the averaged parameter is stable between SOI+1 ms and EOI−1 ms. This is shown for vapor velocity in Figure 3.21. The steady state period is shaded and the resulting average value is shown with a horizontal line.

3.4 Measurement methodology

A spray measurement starts by preparing the spray condition: the gas mixture is chosen and filled as described in Section 3.1.3. Then, the automated spray measurement procedure is activated: the controller makes sure that the valves are closed, activates the electric motor that drives the pump camshaft and waits until the target speed is achieved. Once this happens, the fast data-acquisition procedure is activated which first waits for a trigger pulse from the camshaft, then generates a spark to ignite the mixture.

The pre-combustion then increases gas pressure and temperature and after the cool-down time (expressed in a number of revolutions at a certain engine speed instead of time, as further explained below) the high pressure pump is activated for exactly one revolution. At the same time,

starting with the trigger pulse from the camshaft, the pressure sensors and needle lift sensor are sampled with exactly double the sampling frequency of the camera acquisition (shown in the synchronization plots in Figure 3.9) while the LEDs are activated at half the camera frequency to obtain a Mie and Schlieren frame every other frame.

The final results depend on the accuracy of all the above described steps. The cool-down time is determined in advance, from a separate precombustion experiment, and is fixed for a spray measurement. Gases are filled sequentially and after achieving the partial pressure setpoint the pressure is measured with the absolute pressure sensor. This pressure measurement will be used to evaluate the performance of the filling system and to calculate what the exact gas conditions were at the SOI.

With a PLN injection system, the fuel pressure starts to rise when the inlet port of the pump is closed by the pump plunger when it moves upwards, pushed by the camshaft. Fuel pressure increases more and more and at a certain point the injector needle is able to lift and injection starts. Because it is possible that the electric motor runs slightly faster or slower, the camshaft position and thus port closure timing after the cool-down period is not exactly known. This is the reason that the cool-down time is converted to a number of revolutions instead of time. This method limits the total time variation at true SOI to 1.85 ms (observed from the images).

To evaluate the exact gas conditions during the spray experiment, the SOI is determined for every measurement by detecting the time at which the needle lift reaches half its maximum. Together with the measured gas partial pressures and the measured chamber pressure this allows to calculate the actual gas temperature at SOI. This analysis will be done in the next Chapter for an evaporating, non-reacting measurement set and a reacting measurement set.

After checking the ambient conditions, the images from the measurement are processed with the image detection code, described in Section 3.3 and results are checked before calculating an ensemble average. Experiments that showed clear problems, e.g. due to bad cleaning of the setups windows in between experiments, were discarded. Final ensemble averaged results are reported in the next chapter.

4

Marine fuel spray measurements

" There's method in his madness!"

- William Shakespeare - Hamlet -

In the following Chapter, the accuracy and repeatability of the ambient boundary conditions are first checked. Next, the obtained spray parameters for evaporating, non-reacting and reacting conditions are discussed for a range of boundary conditions. The influence of the injection rate is explained after which a discussion of the effects of the ambient conditions follows. Finally, the influence of the selected surrogate fuel is shown in the last Section of this Chapter.

4.1 Evaluation of the repeatability of ambient gas conditions

To make a further analysis of ensemble averaged data possible, the repeatability of the ambient conditions has to be checked rigorously. If ambient conditions would change between iterations of the same measurement point, it would be difficult to defend that spray development would be the same in between iterations which would render the ensemble average useless.

On the other hand, the accuracy (as in achieving the exact right ambient conditions) is not critical as long as the actual achieved condition can be known based on the measurement data. This will be explained for evaporating, non-reacting conditions and evaporating, reacting conditions in the next subsections.

4.1.1 Evaporating, non-reacting conditions

The chamber pressure from four evaporating, non-reacting experiments is shown in Figure 4.1. After ignition and the cooling time the injection pump is activated and fuel is injected. Because the fuel evaporates, the chamber pressure decreases faster during the injection of fuel; visible at around 2.15 s after the start of the experiment. The pressure

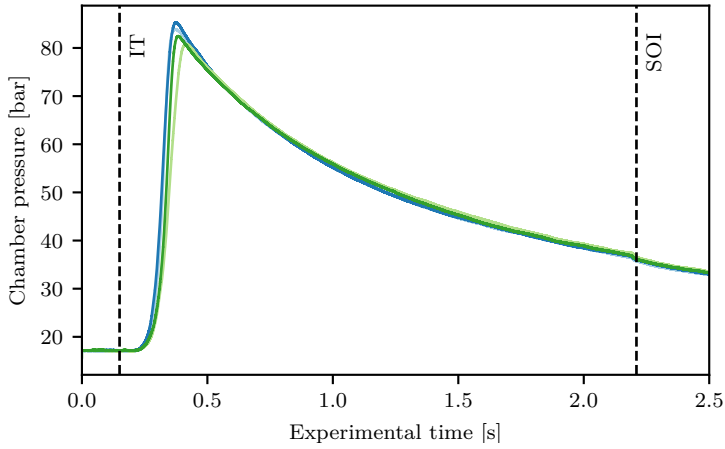

Figure 4.1: Chamber pressure as a function of time from four non-reacting spray experiments: pressure increases from the pre-combustion (left dashed line shows ignition timing), diesel start of injection results in a faster pressure decrease (right dashed line).

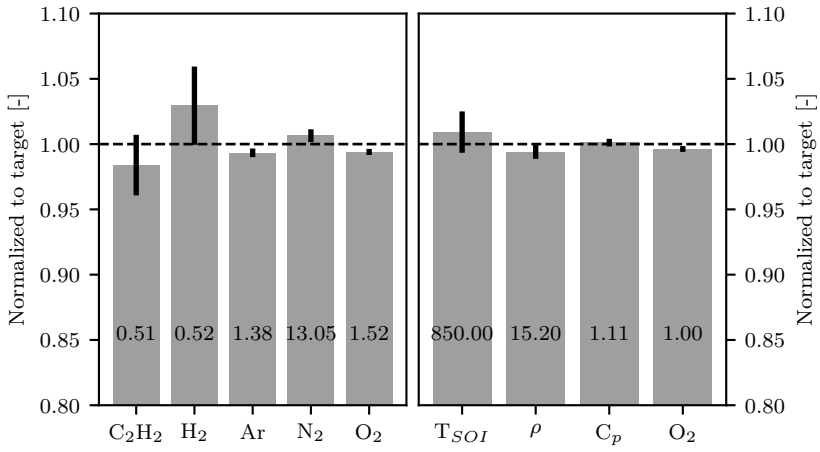

Figure 4.2: Normalized averaged measured partial pressures and resulting normalized averaged ambient conditions for an evaporating, non-reacting case, with the target values shown in the bars and the standard deviation as the error bar.

measurement already shows the repeatability of the pre-combustion. Peak pressure varies by less than 6 % and variation after the cooling time is even lower, as will be quantified later in the analysis.

To quantify the performance of the pre-combustion technique the measured partial pressures are compared to the target pressures on the left-hand side of Figure 4.2. The average value over all measurements is normalized by the target partial pressure and the standard deviation is shown as the error bar. Acetylene is systematically slightly underfilled, while hydrogen is slightly overfilled. The other gases are filled within 1 % of their target. The standard deviation of the fuel gases is also bigger, which can be explained because they are filled first and because the setpoints are very small. Filling the first gas in the chamber causes less dampening of pressure oscillations over the gas filter. The setpoints are small, so the update speed of the filling controller becomes much more important. Once there is an overshoot, the relative error becomes bigger much quicker for lower setpoints than for higher setpoints.

Mixtures that had a filling accuracy worse than ±10 mbar on a setpoint of 0.5 bar were discarded before executing the measurement because of a higher risk of abnormal combustion or no pre-combustion at all, so these are not included.

The effect of the filling error on the target is calculated backwards as in Appendix A. The calculation is started from the measured partial pressures and the gas conditions after complete combustion at SOI are calculated: gas temperature, gas density, gas heat capacity and oxygen

concentration.

The SOI timing is determined from the needle lift measurement: the time of the rising edge of the needle lift is detected and this time is used to evaluate bulk gas pressure and bulk gas temperature at the precise moment of injection.

Density is determined by calculating the mass in the chamber from the pressures and dividing by the chamber volume which was determined from the cad drawings. The mixture's heat capacity is weighted by mass fractions. The target oxygen concentration after pre-combustion is zero and to normalize this fraction the following equation is used to avoid division by zero:

$$O_{2,norm} = \frac{O_{2,burned} + 1}{O_{2,target} + 1} \tag{4.1}$$

where $O_{2,burned}$ is the oxygen fraction after complete combustion. The burned oxygen fraction is calculated as the difference of the $O_{2,filled}$ and the necessary O_2 to oxidize all the fuel which means that rich mixtures result in negative $O_{2,burned}$. This means that the normalized oxygen concentration is lower than one when there is an oxygen deficiency and higher than one when there is excess oxygen. Normalized results are shown on the right-hand side of Figure 4.2.

Density, heat capacity and oxygen concentration results are within 1 % of the target. Gas temperature at SOI is on average 8 K higher than the target with a standard deviation of ±22.5 K. The effect of these deviations will be estimated in Chapter 5.

4.1.2 Reacting conditions

After analyzing the reacting conditions in the same way, the repeatability was found to be very good as shown in Figure 4.3: pressure as a function of time is shown for five reacting experiments at 21 % oxygen concentration, 850 K SOI gas temperature and 15.2 kg/m^3 density. The variation between measured maximum pressures is minimal as is the variation in pressure and bulk temperature at SOI.

In Figure 4.4 the gas partial pressures and conditions are again compared to the target. The partial pressures are good, given that the target partial pressures for acetylene and hydrogen decreased relative to non-reacting conditions which increases the relative error. Care was taken not to overfill the premixed fuels to prevent an excessive peak pressure. From the right-hand side it is clear that a mistake was made for the SOI gas temperature which is on average only 762 K instead of the target of 850 K. The cool down time was chosen wrongly; longer than necessary and this resulted in a lower gas temperature. To make

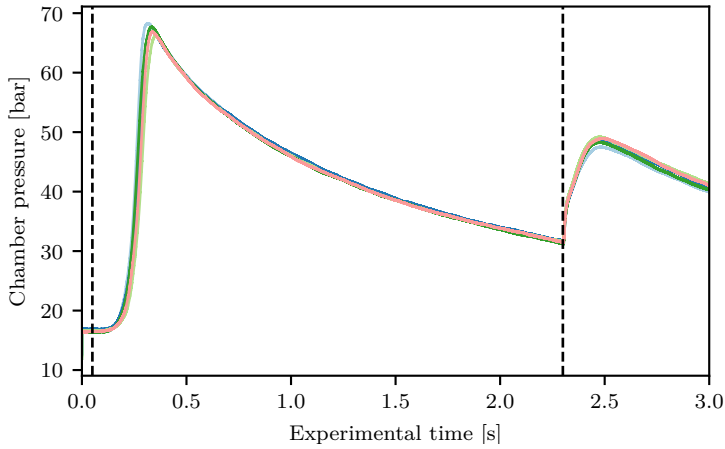

Figure 4.3: Chamber pressure as a function of time for reacting spray experiments: pressure increases from the pre-combustion and diesel combustion also causes a pressure increase.

comparison with the non-reacting measurements possible, the reacting measurement with 13 % oxygen was repeated with the correct cool-down time. Because the standard deviation is small in the first measurement set, the measurements were then analyzed further with a changed SOI gas temperature of 760 K as another target point.

4.1.3 Evaluation of all conditions

One evaporating, non-reacting and one reacting condition was discussed above in detail, the rest of the conditions are summarized in Table 4.1. The data shows that the standard deviation is always very low, but that the exact condition is not always reached perfectly. For example the resulting heat capacity differs from the target at some conditions. The explanation for this error is twofold: the target heat capacity and the different temperature dependence of the heat capacity of the mixture, as will now be explained further.

An error during the calculation of the gas mixtures was detected: the target heat capacity was always calculated for an air mixture at 850 K. The target heat capacity was constant, but in reality it changes, e.g. from 1.08 J/kgK to 1.14 J/kgK when gas temperature increases from 700 K to 950 K. Secondly, the mixture after pre-combustion is not air, it contains combustion products as well. This changes the temperature dependence of the heat capacity of the mixture compared to air which explains the rest of the error. The effect of this error is estimated in Chapter 5. It was

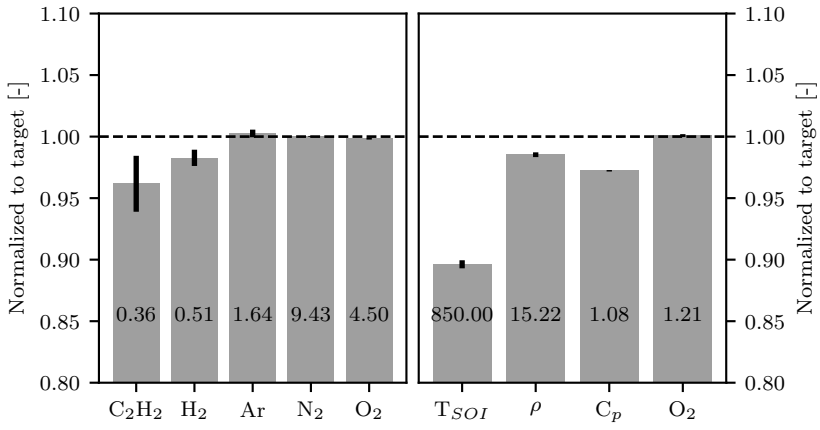

Figure 4.4: Normalized averaged measured partial pressures and resulting normalized averaged ambient conditions for a reacting case, with the target values shown in the bars and the standard deviation as the error bar.

found that this error only has a limited effect on spray development, so the conditions were not updated during the main measurement campaign.

Table 4.1: Target conditions and achieved conditions

Target condition				**Average± standard deviation**			
T_{SOI}	O_2	ρ	C_p	T_{SOI}	O_2	ρ	C_p
[K]	[-]	[kg/m^3]	[J/kgK]	[K]	[-]	[kg/m^3]	[J/kgK]
Evaporating, non reacting							
850	0	22.8	1.11	850±7	0.0048±0.0015	22.36±0.04	1.106±0.002
1000	0	15.2	1.14	950±18	-0.0035±0.0021	15.19±0.05	1.060±0.002
850	0	15.2	1.11	856±11	-0.0048±0.0025	15.07±0.08	1.110±0.003
700	0	15.2	1.08	706±7	-0.0048±0.0017	15.14±0.05	1.080±0.003
850	0	7.6	1.11	846±4	-0.0062±0.0058	7.64±0.05	1.070±0.001
Reacting							
760	0.13	15.2	1.09	780±9	0.1290±0.0008	15.01±0.04	1.050±0.002
850	0.13	15.2	1.11	869±5	0.1300±0.0011	15.01±0.02	1.110±0.0005
760	0.19	15.2	1.09	770±7	0.1900±0.0007	15.03±0.02	1.050±0.002
760	0.21	15.2	1.09	762±3	0.2110±0.0016	15.00±0.03	1.050±0.001

4.2 Influence of injection rate on spray development

Due to the specifics of the PLN injection system, injection pressure varies strongly during every injection and additionally the maximum injection pressure depends on the engine speed and injection duration. Especially at low loads and thus lower injection pressures, the combustion behavior of this injection system cannot be captured by standard modeling techniques as will be explained in Chapter 5. In this section the spray formation is studied for different injection rates, to improve the understanding of the spray formation at different injection rates.

The injection pressure and needle lift are shown in Figure 4.5 for four different injection configurations. The first experiments were executed with a moderate injection duration and as liquid length already reached a maximum value after about 2 ms (shown in later figures) it was chosen to reduce the injection duration for further experiments to reduce fuel deposition in the chamber. A nozzle hat allows one spray to pass freely while the other sprays are caught in a central tube. This fuel does not evaporate and drops to the bottom of the chamber which requires cleanup between experiments.

The figure also shows the result of the needle lift detection that was used to determine the exact timing for determination of the achieved boundary conditions mentioned above. The time of the detected needle lift, i.e. start of injection (SOI), is set to 0 ms after SOI and this is used in the subsequent figures to allow a comparison of the spray development as a function of time.

The initial pressure increase is followed by a small decrease at the moment that the needle lifts and fuel velocity suddenly increases at the nozzle. This creates a pressure wave which is visible at the pressure measurement location. This is more pronounced for the eight-hole nozzle than for the ten-hole nozzle.

The ten-hole nozzle shows a smooth, steady needle lift while the eight-hole nozzle has a two-stage needle lift. The initial needle lift in the eight hole nozzle apparently causes a pressure decrease in the volume below the needle so that the needle is unable to lift completely. Additional fuel compression by the pump finally increases the flow rate and pressure in the volume below the needle causing a full needle lift. A lower engine speed results in a slower pressure increase and a lower maximum pressure.

Average vapor and liquid penetration is shown on the top of Figure 4.6 for 800 and 630 rpm while the spray spreading angle is shown on the bottom as a function of time after SOI. The end of injection (EOI) is determined based on the needle lift measurement and shown with a vertical line.

Initially, liquid and vapor are penetrating together and after about 1.2 ms liquid length starts to deviate and reaches a semi-constant value. Steady state liquid penetration is unaffected by engine speed.

The transient penetration differs however: while the penetration speed at 800 rpm is more or less constant, the vapor penetration speed at 630 rpm first decreases and then accelerates again. This can be explained by the small partial needle lift at 630 rpm in Figure 4.5: the needle first lifts only partially, closes and then opens completely. This results in an unsteady pressure in the nozzle sac volume which explains a variable injection velocity and thus variable penetration speeds.

The spray spreading angle shown is detected with the line-fit method and shows a high initial value which then decreases to a steady state value which is consistent with literature [44, 46]. Near the end of the injection, when the injection pressure is decreasing, the spray angle decreases slightly. Differences of the spray angle between engine speeds are very limited.

The same comparison is done for an eight and ten hole nozzle in Figure 4.7. Vapor and liquid penetration start earlier for the eight hole nozzle. This is due to the needle lift profile: the eight hole nozzle shows a two-stage needle lift. At 800 rpm the needle does not close as at 630 rpm but nevertheless needle lift slows down slightly. The needle lift detection determines half of the maximum needle lift as the SOI time which offsets

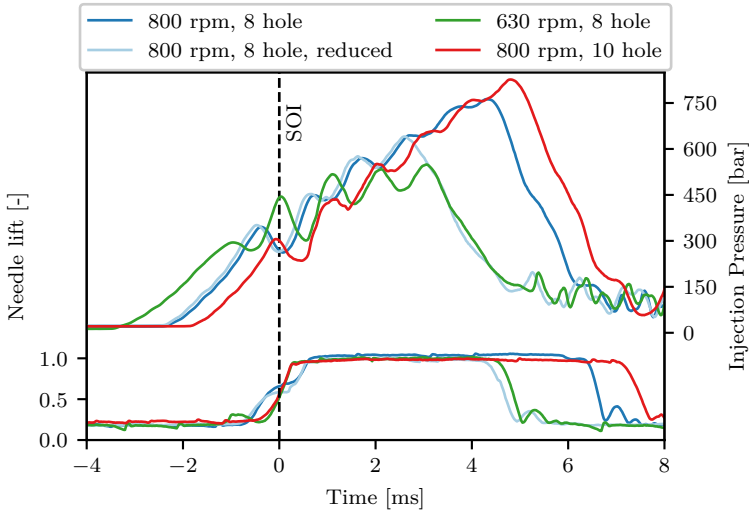

Figure 4.5: Injection pressure and needle lift for n-Dodecane sprays with 800 *and* 630 rpm *engine speeds.*

this time slightly.

Penetration speed of the ten hole nozzle is on par with that of the eight hole nozzle, while liquid length is smaller. The hole diameter of the ten hole nozzle (0.38 mm) is smaller than the eight hole (0.44 mm). Liquid length scales with hole diameter which was found by several authors [49–51] and can be confirmed here for PLN systems. The spray angle of the ten hole nozzle directly shows a semi-steady state, while the eight hole nozzle has a strong initial peak and ends with a slightly smaller spray angle in the end. This difference can be explained by the two-stage needle lift. During the first-stage the spray angle is bigger. With a fully opened needle, the spray angle decreases.

After the EOI, indicated by the vertical lines, the liquid length quickly drops to zero. The experiments with the ten hole nozzle had a higher

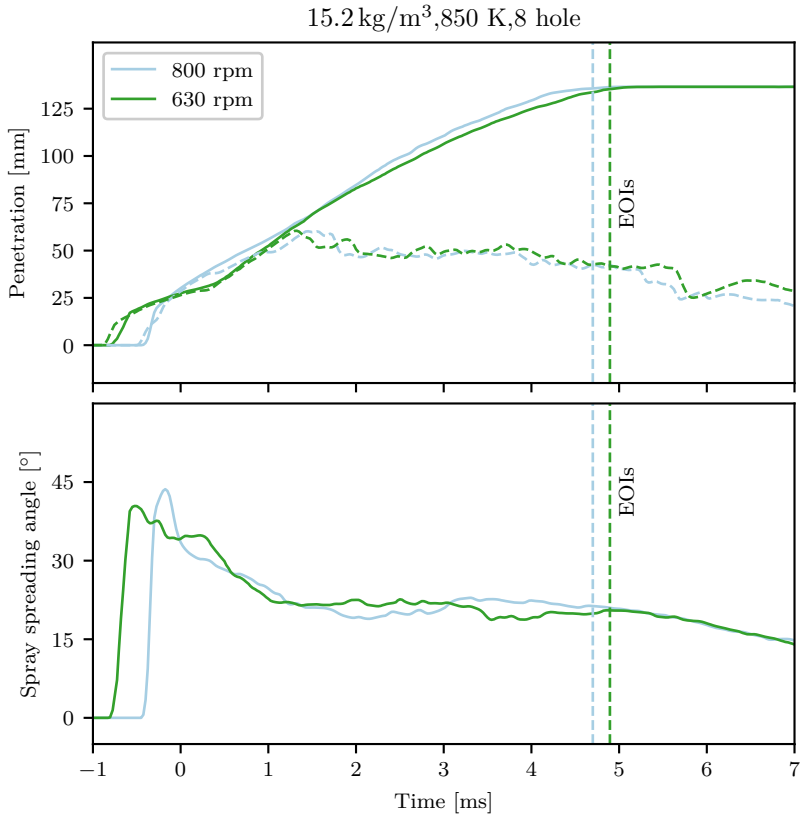

Figure 4.6: Liquid (dashed) and vapor (solid) penetration (top) and spray spreading angle (bottom) for n-Dodecane sprays with 800 *and* 630 rpm *engine speeds (constant ambient gas conditions).*

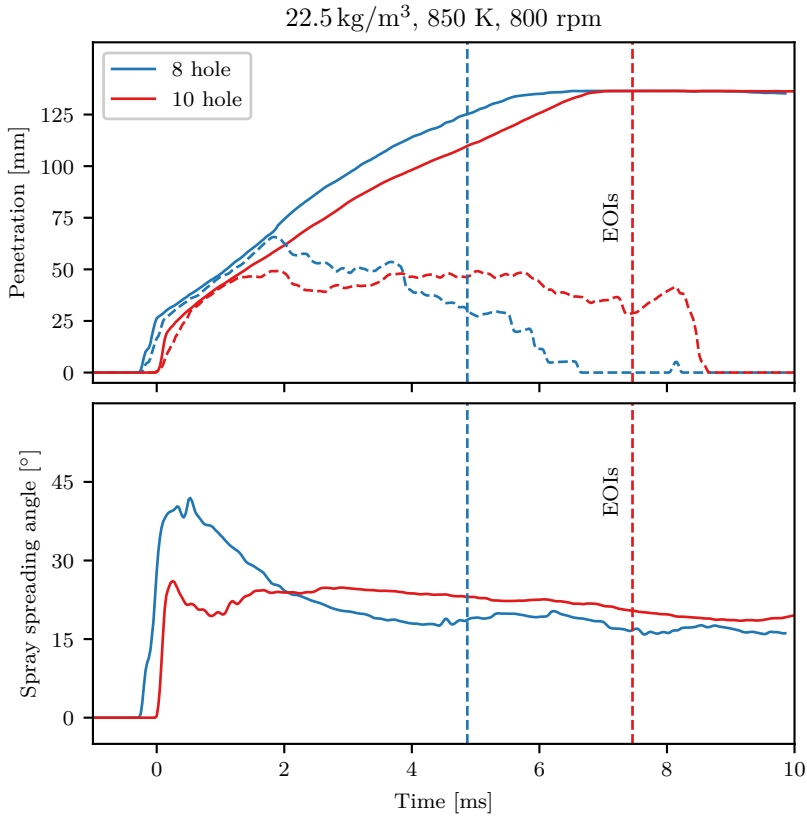

Figure 4.7: Liquid (dashed) and vapor (solid) penetration (top) and spray spreading angle (bottom) for n-Dodecane sprays with eight and ten hole injectors.

fueling rate. This was reduced for the other experiments to reduce contamination of the chamber. The quick liquid length decrease was not observed for the speed variation in Figure 4.6, but after analysis of the images it was clear that detection was not reliable for those measurements. Scattered light was present from the non-investigated sprays near the EOI which caused this deviation, while this was not the case for the hole variation measurements. Nevertheless, it is remarkable that it takes only about 1 ms for the liquid length to decrease back to zero, while it takes 2 ms to reach a steady state liquid penetration.

An explanation might be given by increased entrainment after EOI and this depends on the ramp-down of injection velocity, described by [54]. This will be further investigated by 1-D simulation in Chapter 5.

4.3 Influence of ambient conditions on spray development

First, the evaporating spray experiments will be explained. The ambient density and ambient temperature variation effects on spray penetration, liquid penetration and spray angle are shown. This is then repeated for the reacting spray conditions.

4.3.1 Evaporating, non-reacting conditions

The influence of ambient gas temperature is shown in Figure 4.8 for a fixed engine speed of 800 rpm and constant density of 15.2 kg/m^3 for the eight hole injector. Vapor penetration and spray angle (not shown) are unaffected by changing gas temperature while liquid penetration increases when the gas temperature decreases. This influence decreases with increasing gas temperature: liquid length decreases by approximately 30 % when temperature increases from 700 K to 850 K but only decreases by maximum 2 % when the temperature is further increased to 950 K. When evaluating the actual boundary conditions both 700 K and 850 K were achieved within 10 K with low standard deviations while the 950 K condition showed a lower actual achieved temperature and higher standard deviation. Thus experimental error can partially explain this

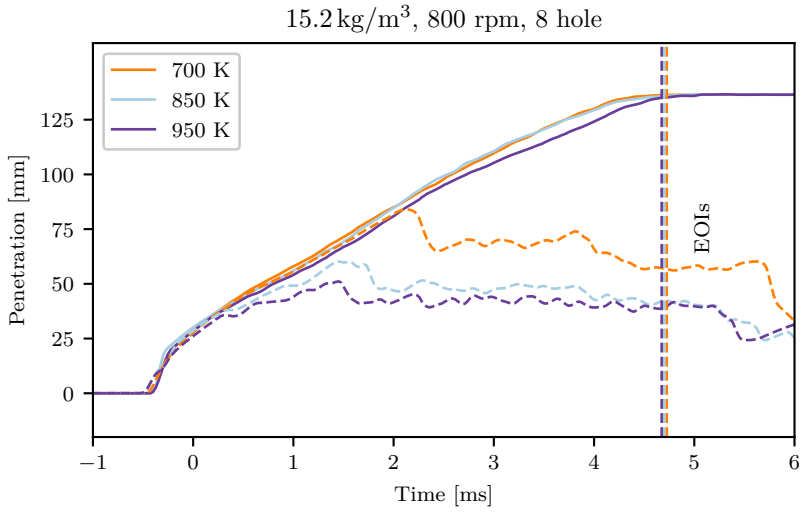

Figure 4.8: Liquid (dashed) and vapor (solid) penetration for n-Dodecane sprays with varying gas temperature.

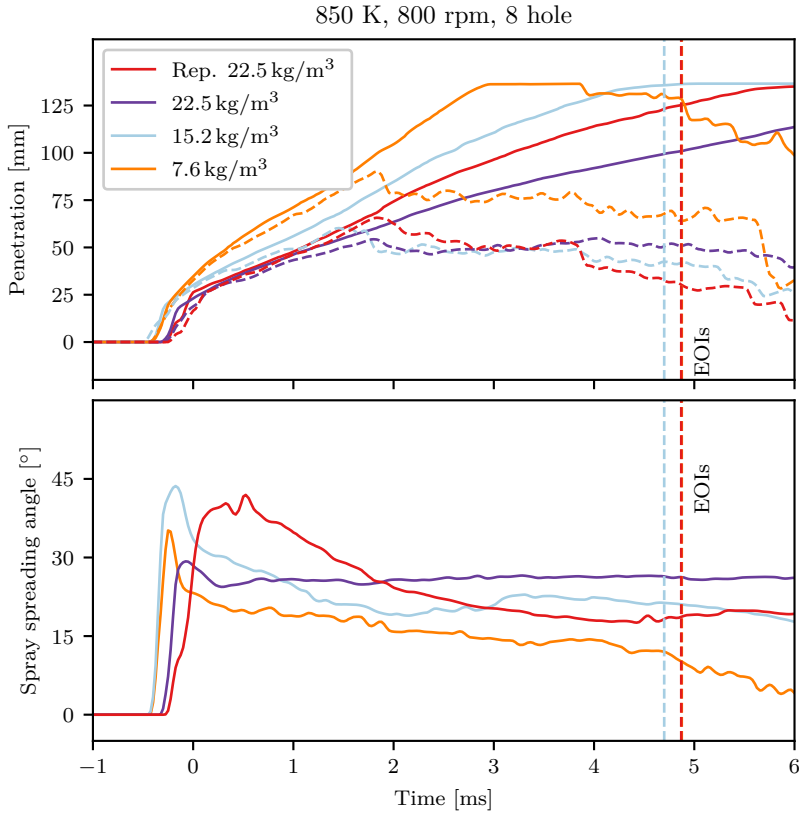

Figure 4.9: Liquid (dashed) and vapor (solid) penetration (top) and spray spreading angle (bottom) for n-Dodecane sprays with varying gas density.

behavior, but a decreasing influence with increasing temperature was also observed in literature [49, 51].

Increasing ambient density influences all measured parameters to a certain extent: spray angle increases, penetration speed decreases and liquid length decreases, as shown in Figure 4.9. In literature ambient density was found to have a strong, but non-linear effect on liquid length [49]. At higher densities a further increasing density results in a smaller effect on the liquid length. This is also found here, but while the penetration speed decreased when increasing ambient density from 15.2 kg/m^3 to 22.5 kg/m^3, the steady state liquid length did not decrease at all. Even with the decreasing effect at higher densities, the liquid length was expected to decrease slightly. Boundary conditions were evaluated rigorously, but no significant differences were found that could explain this.

Apart from increased drag by a higher density, the reasons for the density effect on liquid length lie in the energy that is entrained by ambient gas. This is a direct consequence of the mixing limited evaporation rate explained in Chapter 2. Equation (2.2) indicates that the amount of entrained gas increases proportional to the square root of the ambient density, which provides more energy for evaporation. The square root dependency explains the decreasing effect at increasing densities. Additionally, the spray spreading angle increases with increasing density [47, 51] which again increases the entrained energy and reduces the liquid length.

This makes an explanation of the highest density case difficult: the spray spreading angle increases, which together with an increased density and equal gas temperature should result in a decreasing steady state liquid length. This experiment was measured separately from the main measurement campaign and while care was taken to mount optical components in the same way one reason for this change could be a small change in optics positioning which altered the liquid length measurement. This sensitivity of the Mie scattering technique is acknowledged in literature [87]. After analysis of this measurement with a 1-D spray simulation code in Chapter 5, this was the only measurement that could not be matched with the simulation results..

This measurement was repeated and a higher vapor penetration speed was found in the repetition, while liquid length remained constant. The repetition was checked for consistency with the other measurements by repeating the 15.2 kg/m^3 at 850 K as well. This provided the same results, confirming the quality of this measurement set. The final vapor penetration in a high density environment aligns better with the simulation result, although the measured liquid length remains higher than expected. The reason for this measurement error is probably the nozzle hat. The nozzle hat is mounted on the injector to isolate one of the sprays for optical investigation, but it is possible that this was not aligned perfectly to the nozzle hole in the first measurement set. This would cause the exiting spray to impact partially on the nozzle hat, altering the spray characteristics.

4.3.2 Reacting conditions

Vapor and liquid penetration are shown for a varying ambient oxygen concentration on top of Figure 4.10, on the bottom the spray spreading angle is shown. The evaporating, non-reacting case with a slightly lower ambient gas temperature shows a semi-steady liquid length 2 ms after SOI. This is consistent with a shorter liquid length at 13 % oxygen concentration. However, at around 4 ms after SOI, liquid

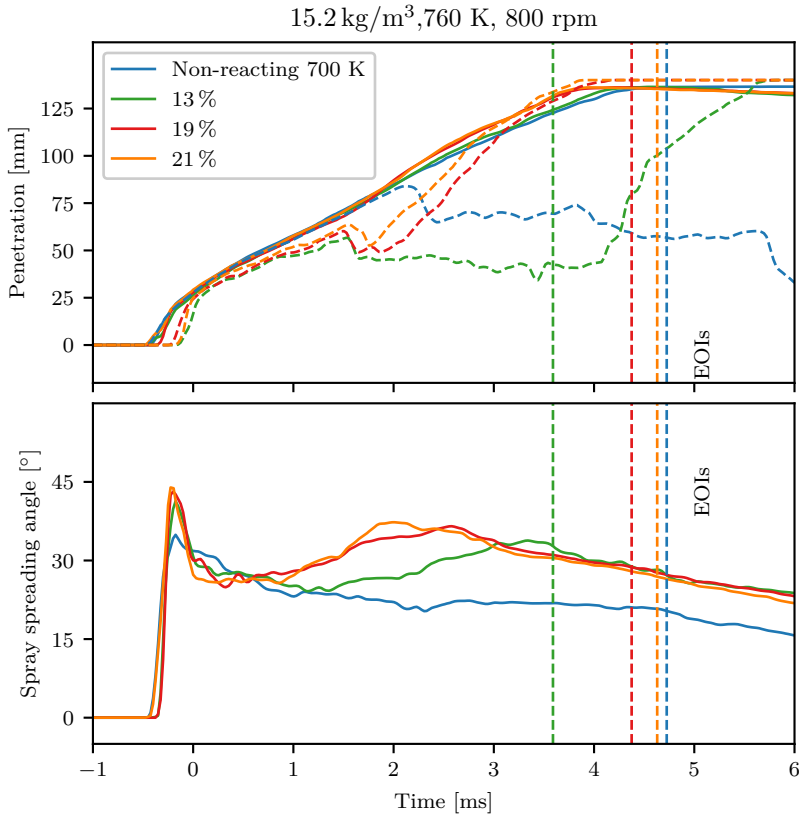

Figure 4.10: Liquid (dashed) and vapor (solid) penetration (top) and spray spreading angle (bottom) for n-Dodecane sprays with varying oxygen concentration.

penetration starts to increase again and this timing advances when oxygen concentration is increased.

This apparent liquid length increase is not caused by an actual increasing liquid penetration, but rather by soot luminosity that provides an indication of high temperature combustion. When the oxygen concentration increases, the ignition delay decreases and high temperature combustion starts sooner which results in an optical anomaly of a longer detected apparent liquid length.

The spray spreading angle first follows the evaporating, non-reacting case closely, but starts to deviate after some time, consistent with literature [92, 93]. The higher the oxygen concentration, the sooner this deviation starts. The spray angle always increases before the liquid length starts to increase which can be explained by chemical kinetics. First stage

heat release causes gases in the spray to expand, but temperature is not yet high enough to produce soot and increase luminosity. Shorter ignition delays with higher oxygen concentrations result in first stage ignition of richer mixtures which in turn promotes immediate second stage ignition and hence luminosity quickly starts to increase with higher oxygen fraction.

The injection process is compared between an evaporating, non-reacting case and a reacting case in Figure 4.11. Gas temperature was increased to 850 K to make direct comparison of the images possible. Spray penetration and spray spreading angle plots are shown on top, together with processed images of the experiment with their timings indicated as black dotted lines on the plots. The evaporating, non-reacting vapor penetration is shown on the left, the reacting vapor penetration in the middle and liquid detection images are shown on the right hand side.

During the first 2 ms spray development is very similar: the liquid length develops in a similar manner and reaches steady state after about 1 ms. At 2 ms after SOI the spray angle starts to increase for the reacting case. This is visible in the middle vapor penetration images as a low intensity schlieren 'disappeareance' while the non-reacting case remains completely dark. This schlieren effect is caused by radial expansion of the spray due to cool-flame reactions and decreasing local density. This was decribed as an apparent disappeareance of the schlieren effect in [94].

Around 3 ms after SOI the second stage ignition starts, visible as a luminosity cloud in the center of the right-hand side image. Liquid is also still visible near the injector. It is remarkable that initial ignition does not happen in the head of the spray. Penetration can be estimated from the middle images: at 3 ms after SOI the spray penetrates approximately until 75 % of the chamber while the initial luminosity is located in between 25 % and 50 % of the maximum penetration. Luminosity then expands quickly to fill the whole downstream spray and after the EOI at around 4 ms the luminosity recesses back to the nozzle hole (not completely shown in the images).

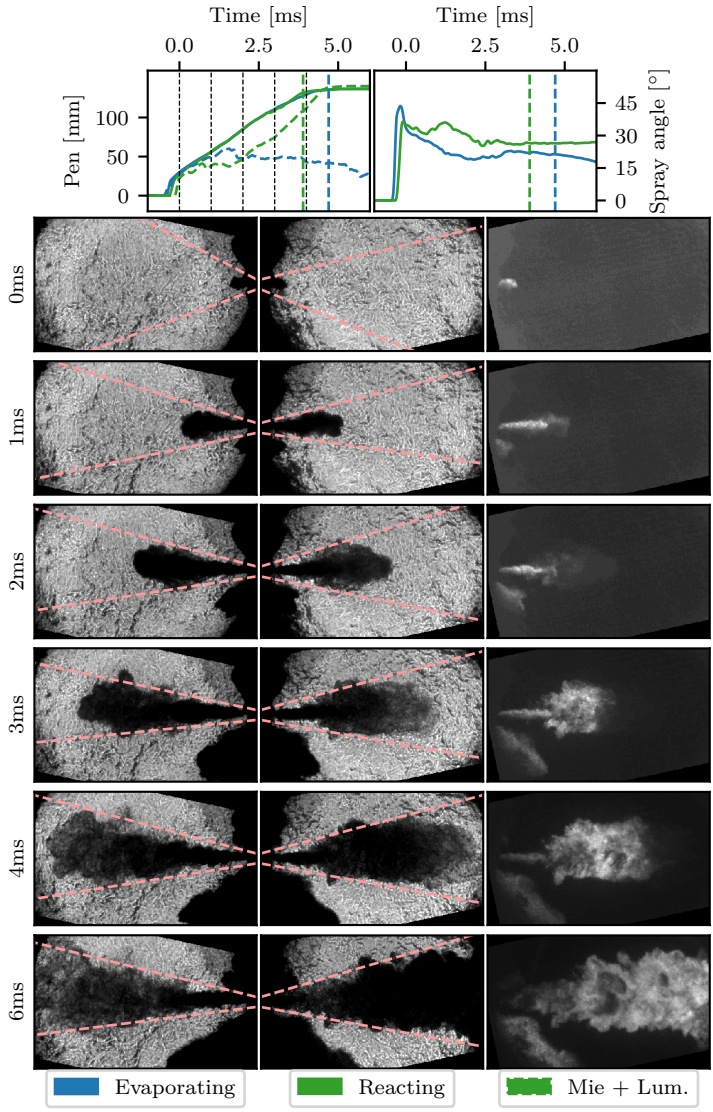

Figure 4.11: Set of spray images comparing a non-reacting spray (left) at 850 K *to a reacting spray (middle) at* 13 % O_2 *and* 850 K *gas temperature. Mie images on the right for the reacting spray: initially they show liquid penetration but soot luminosity expands in the spray from* 3 ms *after SOI. Spray vapor and liquid penetration, together with their spray angle shown on top: blue for non reacting and green for the reacting spray. Black dashed vertical lines show the timings of the selected images.*

4.4 Fuel influence

The surrogate fuel was tested in detail to provide the most useful measurement database for further testing and validation of other simulation codes. For n-dodecane multiple detailed and reduced chemical reaction schemes have been developed, as was described in Chapter 2. Avoiding the distillation curve of diesel simplifies the simulation in Chapter 5 greatly. In this section the influence of the surrogate fuel on spray characteristics is estimated.

The experiments were repeated with regular diesel fuel for evaporating, non-reacting conditions. As fuel properties of the surrogate fuel are only an approximation of the actual fuel, the sensitivity of the spray characteristics to changing boundary conditions is compared between the surrogate fuel and the actual fuel.

Injection pressure and needle lift development are compared for diesel and n-dodecane in Figure 4.12 for 800 rpm. These are found to be almost identical. Pressure waves in the injection system are reproduced with the surrogate fuel: evaluation of the fuel properties learns that the speed of sound difference is only 4 % which results in similar pressure waves.

Viscosity can differ more: depending on fuel temperature, pressure and time of the year, the viscosity of diesel is 30 % to 100 % higher than that of n-dodecane. During winter time the viscosity of diesel fuel is lower to enable better cold-starting ability and as the experiments were done in winter time the low diesel viscosity results in a limited effect on final injection pressure and needle lift. Diesel viscosity was measured ($1.5\,\mathrm{mPa \cdot s@40\,^{\circ}C}$) and this confirmed that the diesel viscosity was close to the viscosity of n-dodecane which resulted in almost identical injection pressure development. This further emphasizes the need for a well defined fuel to allow replication of experiments and simulations.

Averaged values for spray tip velocity, liquid penetration speed and spray angle are calculated as explained in Section 3.3.4. The spray tip velocity is calculated as the penetration difference between two samples, divided by the sampling time. These values show a semi steady state value between 1 ms after SOI and 1 ms before EOI. This approach is not perfect: especially the spray spreading angle shows non-steady behavior during this period, but when comparing spray angle development over time it shows the same trend, justifying the average as a comparison tool between the fuels.

The results are shown as a function of ambient density (left-hand side) and ambient temperature (right-hand side) in Figure 4.13. Vapor penetration speed is shown on top: n-dodecane and diesel fuel show the same trends. Penetration speed decreases with increasing ambient

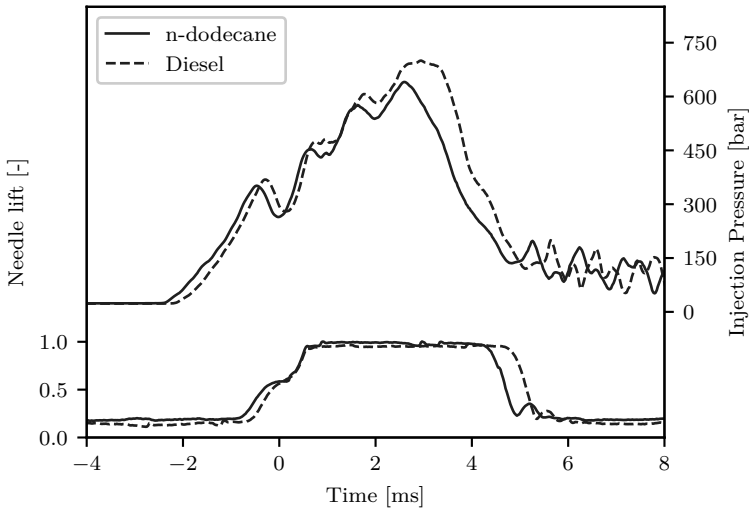

Figure 4.12: Injection pressure and needle lift comparison between diesel and n-dodecane.

density because of momentum transfer from the fuel to the ambient gas. Gas temperature does not influence penetration speed for n-dodecane, but for diesel fuel a decrease is observed for the highest temperature. This was traced back to bad image quality: contrast was low for these images and spray detection failed which resulted in low accuracy for this condition. All experiments at this condition suffered from this problem which was likely caused by a misalignment in the optical components. At the start of a new measurement day optics are checked and adjusted, so this problem was solved for other measurements.

Liquid penetration shows identical trends for both fuels with longer liquid lengths for diesel fuel which could be expected from the boiling point of n-dodecane and distillation curve of diesel (Figure 4.14). Liquid droplets will remain visible throughout the spray until the heaviest fractions are completely evaporated. While the largest part of diesel fuel evaporates relatively quickly, the heaviest fractions determine the liquid length and therefore the liquid length is higher for diesel fuel.

The spray spreading angle shows the same trend for the density variation but differs at the highest gas temperature. Again, this is caused by a problem in the processing of the images. After visual inspection of the resulting images, a too small spray boundary was detected and this results in low spray spreading angle values for diesel fuel at 950 K.

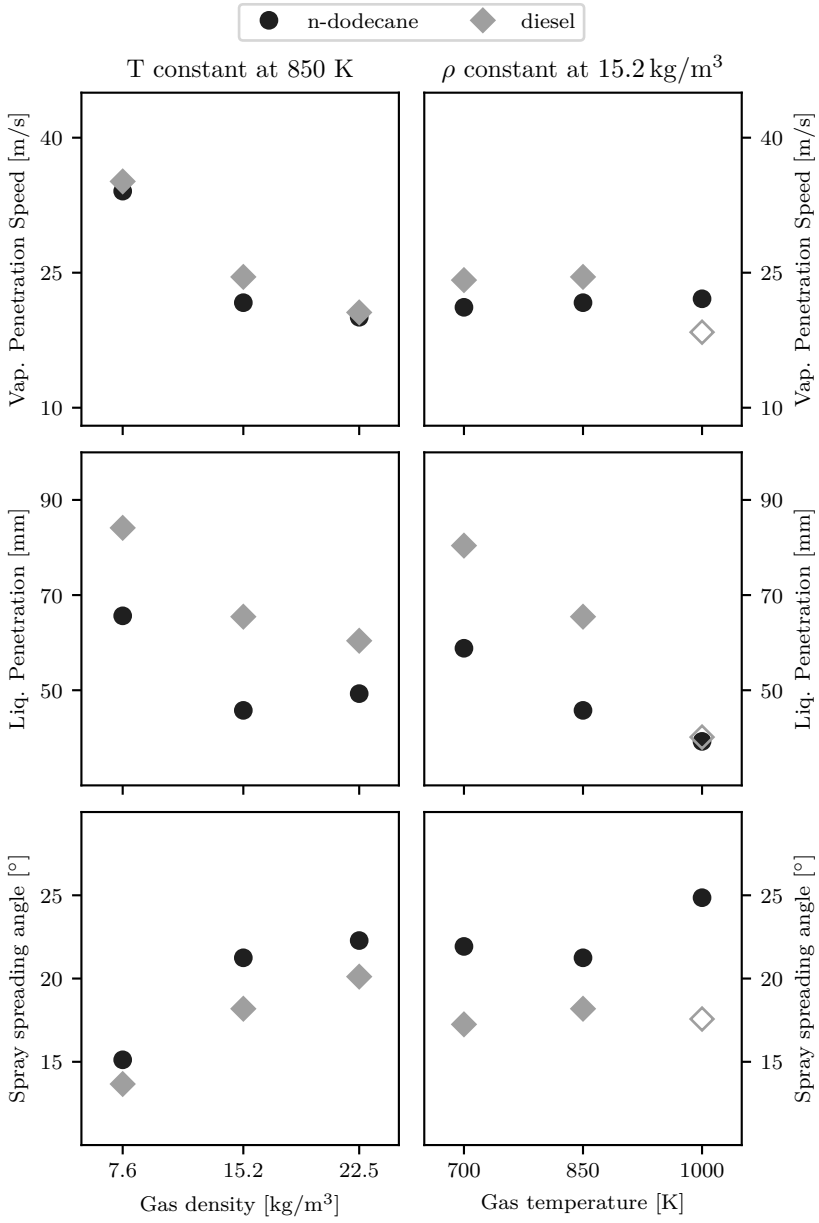

Figure 4.13: Comparison of diesel to n-dodecane fuel for 800 rpm *and the eight hole nozzle. Influence of ambient conditions on steady state spray parameters for evaporating, non-reacting conditions. The highest temperature case with diesel fuel showed optical problems, indicated with the open diamond.*

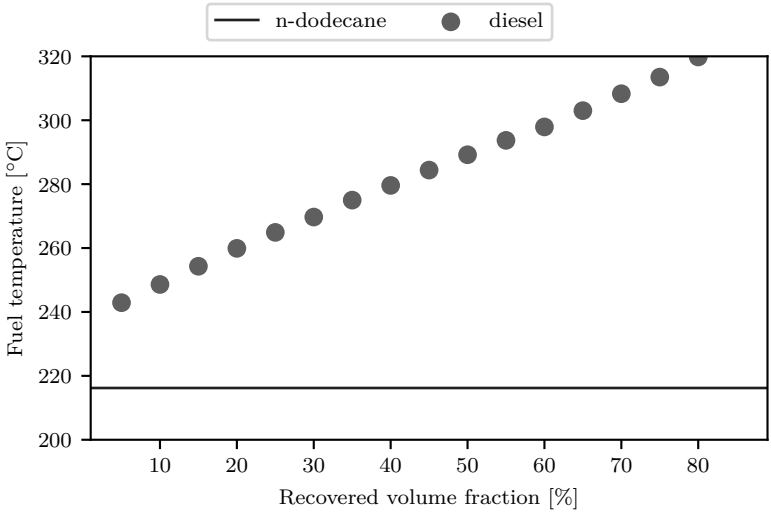

Figure 4.14: Distillation curve compared to n-dodecane boiling point, diesel distillation data taken from [95].

4.5 Summary

In this Chapter, the accuracy and repeatability of the ambient gas conditions were checked. The repeatability of the gas filling system was found to be good and although the fuel concentrations showed a greater standard deviation over the measurements, the final gas temperature, density and oxygen concentration did not show such a great standard deviation for the evaporating, non-reacting spray measurements due to the relatively long cooling period.

An error was identified for the first reacting measurement set. A wrongly chosen cool-down time resulted in a too low ambient gas temperature and heat capacity. These measurements were also discussed, together with a repetition with the correct cool-down time.

The influence of the injection equipment on spray development can be summarized as follows: liquid penetration length decreases with decreasing nozzle hole diameter as in literature, and vapor penetration of the ten hole nozzle is faster with a smaller spray angle.

Increasing ambient temperature results in decreasing steady state liquid penetration, with a decreasing influence with increasing temperatures, with no effect on the vapor penetration. Increasing ambient density results in a decreasing vapor penetration speed and liquid penetration, but at the highest ambient density liquid penetration remains constant. This could be attributed to the optical configuration but other reasons, that will be described in the next Chapter, can be the cause of this. The measurement was repeated and the vapor penetration of the first measurement at high ambient density indeed showed a measurement error.

When the oxygen concentration was increased, the measured spray angle widened compared to the inert, evaporating case. The timing of this spray angle increase advanced with increasing oxygen concentration. Additionally, some luminosity that did not originate from liquid droplets, was observed in the Mie images. Like the spray angle, the onset of this luminosity increase advanced with increasing oxygen concentrations and at 21 % oxygen concentration the spray angle increase and spray luminosity increase happened at approximately the same timing.

5

Fuel Spray Simulation

"I have not failed. I've just found 10,000 ways that won't work."

- Thomas A. Edison -

In this Chapter, a phenomenological spray model, based on literature, is implemented and adjusted for marine PLN operation. The same ambient conditions and injection rates as in the spray measurements are applied in the simulation code and model results are then compared against measured spray data. The simulation model allowed to detect a measurement error at high ambient gas density. A sensitivity analysis was employed to further analyze the deviations.

5.1 Introduction

In Chapter 2, a commercial engine simulation model was employed to predict emissions from a marine engine. It is able to provide information to calibrate current engines but it does not contribute to insight in what happens in the combustion chamber. The model is a black box with unknown tuning/correction values, which are not valid for all operating points in marine injection systems. A deviation in heat release rate at high engine load is discovered that at low engine loads is exactly the opposite. Due to the closed structure of the software it is impossible to identify the cause of the deviation.

This is why a phenomenological spray model, based on literature, is implemented and adjusted for marine PLN operation. The same ambient conditions and injection rates as in the spray measurements are applied in the simulation code. Model results are then compared against measured spray data.

The mass flow rate and momentum flux at the injector are important boundary conditions. It was impossible to measure these directly and another simulation code (Simcenter Amesim [96]) is employed to calculate the flow rate and velocity through the injector as an input for the in-house spray simulation code.

This Chapter starts by explaining some practical consideration regarding nozzle flow. Then, the spray simulation code is introduced and results are presented. The Chapter ends with a sensitivity analysis.

5.2 Nozzle flow

To simulate spray development, the injection velocity and mass flow rate at the nozzle hole are necessary. These could currently not be measured directly so an additional simulation tool was employed: Simcenter Amesim [96]. A hydraulic simulation model of the injection system was built and validated using measurements of the needle lift and injection pressure in the line. This results in mass flow rates as a function of time at the nozzle holes for varying engine speeds and injection set points.

The injection velocity could however not be determined directly by the software because it does not include simulation of cavitation: this will be summarized here, but is explained in more detail in Appendix C.

When injection pressure increases to higher levels, the flow starts to separate at the entrance of the nozzle hole due to inertia forces and a recirculation zone develops. The presence of this recirculation zone decreases the flow area, causing a velocity increase and pressure

decrease. When the pressure drops below the vapor pressure of the liquid, cavitation bubbles occur. Because the vapor from the cavitation separates the nozzle's wall from the liquid, the friction between fuel and the nozzle wall is reduced and as a result of this the wall shear could be expected to be near zero [97]. At the same time, the fuel vapor occupies part of the flow area and thus reduces the available area for liquid fuel flow.

Two flow coefficients can be defined to describe the influence of the above described phenomena: the velocity coefficient C_a and the area coefficient C_v but only an overall discharge coefficient C_d is used in the Amesim code, which does not provide the same information. The relation between the flow coefficients can be understood by the equation:

$$\dot{m}_{eff} = A_{eff} \cdot u_{eff} \cdot \rho_f \tag{5.1}$$

$$= C_a \cdot A_{th} \cdot C_v \cdot u_{th} \cdot \rho_f \tag{5.2}$$

$$= C_a \cdot A_{th} \cdot C_v \cdot \sqrt{\frac{2\Delta P}{\rho_f}} \cdot \rho_f \quad = C_d \cdot A_{th} \cdot \sqrt{\frac{2\Delta P}{\rho_f}} \cdot \rho_f \tag{5.3}$$

with A_{eff} the effective flow area, A_{th} the geometric area, u_{eff} the effective flow velocity, u_{th} the velocity that results from Bernoulli's flow equation and ΔP the pressure difference over the nozzle hole. The geometric area and theoretical velocity are coupled to their effective values by the respective flow coefficients and an overall mass flow coefficient can then be defined as: $C_d = C_a \cdot C_v$.

The mass flow rate increases with increasing flow area and increasing velocity, but the effect of each change is lumped into the discharge coefficient C_d. Now, when cavitation develops in the nozzle hole, the mass flow stagnates and the area coefficient decreases because the fuel vapor occupies part of the flow area and the velocity coefficient increases because the friction reduces. So, while the simulation code provides the correct mass flow rate, the velocity still depends on the onset of cavitation which in turn depends on hole parameters such as diameter, conicity and smoothness of the inlet edges of the hole.

Typically, the injection velocity is determined from the obtained mass flow rate with the assumption of a uniform velocity over the whole nozzle area, shown schematically on top of Figure 5.1 which underestimates injection velocity. By neglecting friction with the walls, a situation such as on the bottom of Figure 5.1 is obtained. In reality, the recirculation zone reattaches to the walls shortly before the nozzle hole's exit and fluid will still experience some friction from the walls.

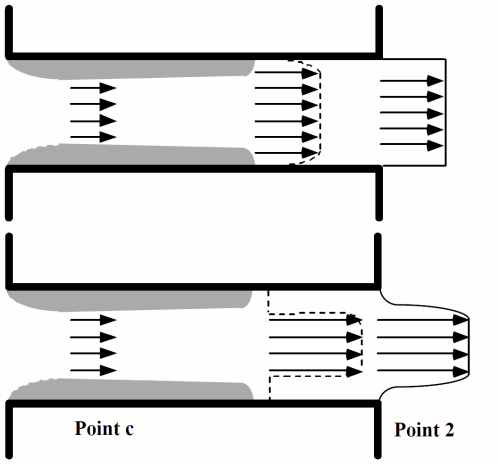

Figure 5.1: Schematic view of the outlet velocity profile in a nozzle hole, excluding the area coefficient on top, including it on the bottom, taken from [97].

The area coefficient is estimated by Equation (C.11) from [97] and depends on the injection pressure at which cavitation starts. When there is no cavitation, the whole area is assumed to have a uniform flow velocity and the area coefficient is unity. For a constant back pressure, the velocity in the hole increases with increasing injection pressure and at a critical injection pressure (P_{crit}) a recirculation zone is formed and the area coefficient starts to decrease. As the onset of cavitation is not known for this injection system, several critical injection pressures will be evaluated during the simulations.

Compared to uniform exit velocity, this assumption will produce the highest possible velocity for the given injection conditions but based on the observations from momentum measurements and optical studies of cavitating flow in nozzles, all described in Appendix C, this method proves to be the best possible option when cavitation is present and no direct measurement possibilities are available.

5.3 Phenomenological 1D modeling

A phenomenological 1D spray model describes the injection process in more detail, by exploiting observed spray characteristics. This model should explain, i.e. reproduce, the measurement results as well as possible. The difference with e.g. a CFD simulation lies in the amount of assumptions, described in the first section below. By accepting more describing assumptions, the amount of calculations can be reduced and computational time of the simulation decreases which is important for engine simulations. This requires more input to the model, e.g. the spray angle, but still some important insight in the spray formation and development can be gained.

The model that is employed here is based on the control volume analysis developed by Musculus-Kattke [54] which in turn was based on Naber and Siebers [47]. The model of Naber and Siebers assumed a constant spray spreading angle, no velocity slip between ambient gas and injected fuel, a constant injection velocity and uniform velocity profiles over the spray cross sections. Control volumes were placed on a 1D grid, ranging from the nozzle hole exit until the end of the combustion chamber. Balancing fuel mass and momentum fluxes over the control volumes, they were able to derive an expression for the cross-sectionally averaged velocity in the control volumes. The penetration distance as a function of time agreed well with experimental data.

The Naber and Siebers model treats the injection velocity invariant with time which does not allow to calculate the dynamics in a fuel spray with an unsteady injection rate. To alleviate this steady state constraint, the domain is discretized in the axial direction and transient terms for spray momentum and mass transfer are added such as in [54, 98].

The domain discretization is shown in Figure 5.2. The boundaries of the control volumes, indicated by dashed lines, are defined by a spray spreading angle Θ and they are further discretized by a constant control volume length dz.

5.3.1 Assumptions

Several assumptions are necessary to solve the transport equations in the spray. Some of the assumptions are based on measurements from either diesel sprays or gas jets, while others are necessary to make the calculation tractable. Gas jets are relevant as the transient development of a diesel spray is analogous to a gas jet [99]. These assumptions are the same as in the Musculus-Kattke model:

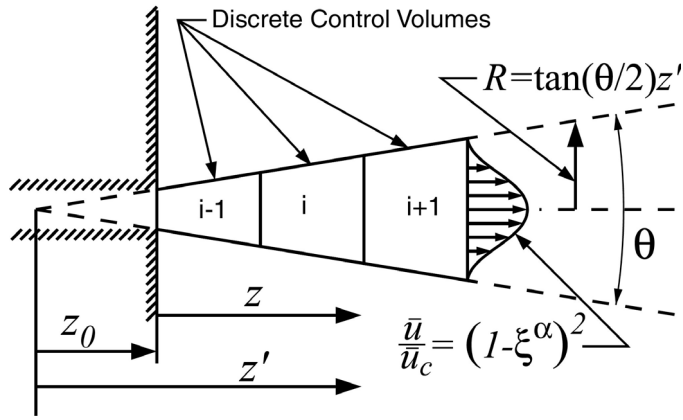

Figure 5.2: Representation of the control volumes in the one-dimensional model, image taken from [54].

- The transport equations are solved for a non-vaporizing spray. A scaling law, developed by Siebers in [43], predicted the liquid length of vaporizing sprays based on a mixing-limited assumption, without explicitly considering evaporation. It is assumed that fuel remains liquid and that the volume, not occupied by liquid, is filled by ambient air.

- The density variation across the jet axis is ignored, instead the cross-sectionally averaged value is used because this simplifies mathematics greatly. The effect of vaporization on local density is too complicated to be considered in this simplified model. This might have an influence on the momentum transport close to the nozzle, as will be explained later.

- The flow is incompressible.

- The turbulent viscous forces acting on the control volumes are neglected.

- The mixing of momentum due to axial diffusion is neglected. Only axial convection is considered in the momentum transport equation.

- The net force due to axial pressure gradients is negligible.

- The spray spreading angle is considered constant through the whole injection process.

- The axial fuel volume fraction, X_f, and velocity, u, are evaluated using assumed radial profiles instead of a constant value over the

whole control volume:

$$\frac{X_f}{X_{f,c}} = (1 - \xi^\alpha)^2 \tag{5.4}$$

$$\frac{u}{u_c} = (1 - \xi^\alpha)^2 \tag{5.5}$$

with subscripts c noting the values on the spray centerline, $\epsilon = r/R$ the ratio of the radial coordinate to the total spray width. The exponent α is a parameter that allows the profile to vary from a uniform flow at the nozzle, to a fully developed flow further downstream in the spray as shown in Figure 5.2. It is assumed these profiles do not change after EOI. Velocity profile measurements in a diesel spray indeed showed essentially identical profiles after EOI [99].

5.3.2 Model development

In each control volume the total fuel mass and total momentum are tracked. The next section is a rewrite of the essential equations of Musculus-Kattke [54]. The obtained total fuel mass will then be used in the next subsection to calculate the evaporation rate in each control volume. The transient transport equations in each control volume for fuel mass and momentum can be written as:

$$\frac{\delta m_f}{\delta t} = \dot{m}_{f,in} - \dot{m}_{f,out} \tag{5.6}$$

$$\frac{\delta M}{\delta t} = \dot{M}_{f,in} - \dot{M}_{f,out} \tag{5.7}$$

with the left hand sides representing the accumulation of mass and momentum in the control volumes and the right hand side the fluxes through the upstream and downstream boundaries. These fluxes are calculated as:

$$\dot{m}_f = \rho_f \int X_f u dA = \rho_f \beta \overline{X}_f \overline{u} A \tag{5.8}$$

$$\dot{M} = \int \rho u^2 dA = \overline{\rho} \beta \overline{u}^2 A \tag{5.9}$$

with ρ_f the fuel density, u the local velocity and β the coefficient that results from the mass distribution. The overbars denote boundary averaged quantities, defined by evaluating the integrals by assuming the radial profiles from Equation (5.4) and Equation (5.5) which could then be rewritten as a function of fuel fraction and velocity averages over the spray cross section, showed with overbars.

These averages are calculated by using $dA = 2\pi R^2 \xi d\xi$ and the centerline fuel fraction relation of Equation (5.4), this results in the averaged fuel fraction:

$$\begin{aligned}\overline{X}_f &= \frac{\int X_f dA}{\int dA} = 2X_{f,c} \int_0^1 (1-\xi^\alpha)^2 \, d\xi \\ &= \frac{\alpha^2}{(\alpha+1)(\alpha+2)} X_{f,c} \end{aligned} \tag{5.10}$$

The same relation is valid between the velocity u_c and $\overline{u}$. When integrating Equation (5.8) and Equation (5.9) centerline values are substituted with averaged values (Equation (5.10)) and β accounts for the residual factors that resulted from the integration and were not yet included in the averaging from Equation (5.10).

$$\beta = \frac{6(\alpha+1)(\alpha+2)}{(3\alpha+2)(2\alpha+1)} \tag{5.11}$$

The density in the momentum transport equation is treated constant over the cross section to remove it from the integral in the Musculus-Kattke model. In reality, the density will be higher at the spray centerline and lower near the spray boundaries. The mean density is evaluated as:

$$\overline{\rho} = \rho_f \overline{X}_f + \rho_a (1 - \overline{X}_f) \tag{5.12}$$

This means that momentum transport is underestimated at the centerline and overestimated near the boundaries. This assumption can be avoided by recalculating the momentum integral with the local density ρ instead of $\overline{\rho}$, calculated by the same expression as Equation (5.12) but without the overbars.

This results in an updated momentum flux equation:

$$\dot{M} = \int \rho u^2 dA = \int \left(\rho_f X_f + \rho_a (1 - X_f)\right) u^2 dA \tag{5.13}$$

$$= \left[\rho_f \sigma \overline{X}_f + \rho_a (1 - \sigma \overline{X}_f)\right] \beta \overline{u}^2 A \tag{5.14}$$

In the averaged density an additional factor σ appears, similar to the β factor, that results from residual integration terms and that are not yet included in this β.

$$\sigma = \frac{15(\alpha+1)(\alpha+2)}{(5\alpha+2)(3\alpha+1)} \tag{5.15}$$

The difference in momentum flux between the original calculation with a mean density assumption and the updated calculation with a calculated density over the spray's radial direction is shown in Figure 5.3. The

momentum flux is underestimated significantly near the nozzle in the original model as was reported as a limitation of the model. While this error is significant near the nozzle, further downstream when density variation becomes smaller this error becomes smaller as well. The Musculus-Kattke model was used to evaluate ambient air entrainment after the end of injection, so it was not an issue for their results. When this model is used to predict liquid length and spray penetration over the whole injection duration, the updated equation is necessary.

For every timestep, the transport equations Equation (5.6) and Equation (5.7) are solved and the total mass and momentum in each control volume are updated. Next, the mean fuel volume fraction $\overline{X}_f$ is updated as the ratio of the volume of fuel to the volume of each control volume $A\Delta Z$:

$$\overline{X}_f = \frac{m_f/\rho_f}{A\Delta Z} \tag{5.16}$$

The mean velocity $\overline{u}$ in the control volume is the ratio of momentum and total mass:

$$\overline{u} = \frac{M}{\overline{\rho} A\Delta Z} \tag{5.17}$$

5.3.3 Evaporation rate

The scaling law of Siebers [43] predicted the liquid length based on mixing-limited vaporization (described in Section 2.4.2) which will be applied here as well. It is assumed that interphase transport of energy is

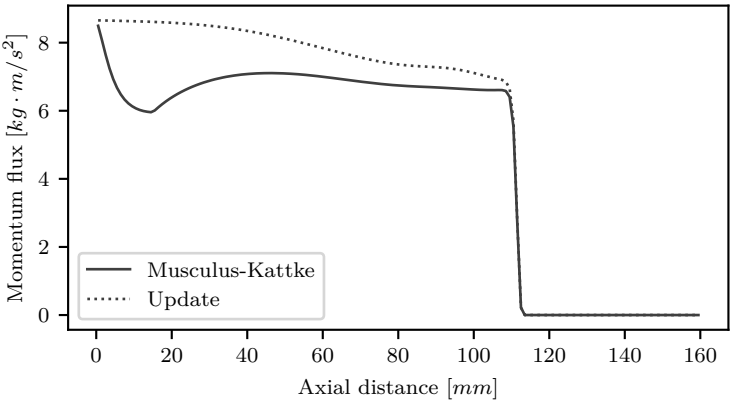

Figure 5.3: Calculation of momentum flux without σ factor (Musculus-Kattke) and with correction (Update).

faster than air-fuel mixing. This essentially means that when energy is entrained by hot ambient gas, fuel evaporates until it reaches its saturation pressure.

For a fixed size control volume and when considering the volume fraction of fuel constant in that control volume, evaporation causes a relative reduction of the mass of fuel in that control volume due to volumetric expansion on evaporation. For the above calculations it is unacceptable that, upon vaporization, fuel would disappear in a control volume to keep volume fraction constant. The volume fraction of the sum of the remaining liquid and vaporized fuel is thus larger than the original non-vaporized volume fraction: $X_{liq}+X_{vap} > X_l$. Because of this, the volume fraction of air will reduce.

The part of a control volume that is not filled with fuel contains ambient air and when no evaporation is considered, the mean density ρ can be calculated easily by weighing mass fractions, Equation (5.12). When fuel evaporates, the density depends on the obtained final temperature in the volume and the amount of fuel that evaporated.

One could also argue that the distribution of fuel, proposed by Equation (5.4) is not valid anymore for either X_{liq} or X_{vap}. On the centerline of the spray the fuel fraction is high and the amount of entrained air is limited which provides only a small amount of entrained energy for evaporation. On the other hand, near the spray boundary, the amount of entrained air is high with a high amount of energy available to evaporate fuel. These phenomena will create a high remaining liquid fuel fraction X_{liq} near the centerline, while the X_{vap} increases very fast close to the boundaries, reaching a maximum on a location that has just the right amount of liquid fuel available together with the entrained air that can provide enough energy to evaporate it.

The following procedure is developed to calculate fuel evaporation:

1. The calculation starts from a fuel density: a fixed volume is filled with a fixed mass of liquid fuel at initial fuel temperature.

2. The remainder of the volume is filled with ambient gas at initial gas temperature.

3. Local conditions are then calculated by assuming adiabatic mixing: fuel will start to evaporate and cool down the ambient gas, until it reaches its saturation pressure. The saturation pressure decreases with decreasing temperature. Saturation pressure thus provides an additional relation to close the energy balance, where both the end

temperature T_{mix} and the evaporated mass m_{vap} are unknown:

$$\begin{aligned} m_a h_{a,T_a} + m_f h_{f,T_f} =& m_a h_{a,T_{mix}} + (m_f - m_{vap}) h_{f,T_{mix}} \\ &+ m_{vap}(h_{vap} + h_{v,T_{mix}} \end{aligned} \tag{5.18}$$

4. In the above energy balance, the mass of air was constant. As the temperature and evaporated fuel fraction increased, the fuel volume increased as well. The calculation is repeated from step two: the remaining part of the fixed volume is filled with ambient air and the energy balance is evaluated again until the air mass stays constant.

The above described procedure is applied on the distribution of fuel X_f in the radial direction of the spray by repeating the calculation at several distances from the spray centerline. On top of Figure 5.4, the volume fraction of X_f is shown as a function of the distance from the spray centerline which is a direct evaluation of Equation (5.4). Close to the spray centerline the volume fraction of fuel is high and air provides little energy to increase the temperature of the mixture and evaporate fuel. Moving closer to the spray boundary, the energy entrainment becomes higher and fuel starts to evaporate more and more until complete evaporation is reached. Once all fuel is evaporated, local mixture temperature starts to increase quickly, shown in the middle of the figure.

The densities of the gaseous components in the ambient gas are evaluated by the ideal gas law and are shown in the bottom of Figure 5.4. The density of liquid fuel is assumed to be constant. While gas conditions would cause the fuel to exist over its critical point after evaporation, this is not the case for the largest part during the evaporation process as can be observed in the contour plot of temperature in Figure 5.16. Near the critical point, large deviations from ideal behavior can exist, so a real gas equation of state (van der Waals model) has been used to evaluated the density for the fuel vapor. The solid lines are the non-evaporating results, while the dotted lines are the densities of the components in the mixture at the thermodynamic conditions at that location in the spray after evaporation. The non-evaporating result shows a constant air density, as air temperature does not change in this case, with an increasing mixture density towards the centerline due to increasing fuel fraction.

The non-evaporating case illustrates the density dependence that was mentioned during the development of the updated momentum flux relation Equation (5.13). Density is indeed higher on the spray centerline and decreases with increasing radial distance, which would influence momentum flux as shown in Figure 5.3.

The evaporating results show an increasing density for air when approaching the spray centerline because air temperature is reduced due to heat transfer from the air to the liquid fuel. A theoretical density of the fuel vapor is shown as well, but the volume fraction of this component is limited by the vapor pressure which limits the effect of this component.

When evaporation is taken into account, mixture density increases which

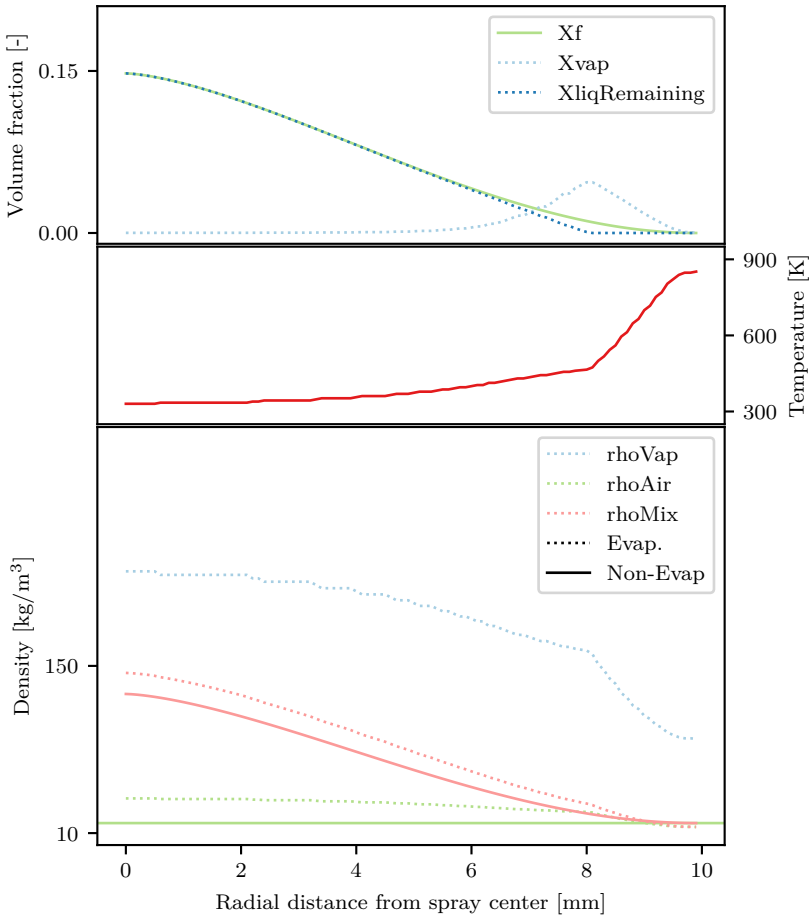

Figure 5.4: Variation over the radial direction of initial volume fraction of fuel and remaining liquid and vapor volume fractions after mixing limited evaporation up to the saturation point (top plot), resulting radial temperature distribution (middle plot) and single component densities at those conditions (bottom plot).

can be explained by looking at the component's densities. Both air and fuel vapor provide sources for a higher mixture density. On the spray centerline the increased air density, due to a lower air temperature, causes the increased mixture density because at that location the fraction of fuel vapor is limited by the low vapor pressure. Near the point of total evaporation (8 mm from the centerline) both fuel vapor and air contribute to increasing local density. Fuel vapor is now present in large quantities because of higher ambient temperature which increases the vapor pressure.

To calculate the liquid penetration in the complete spray simulation the evaporation is only calculated at the sprays centerline as this provides the highest fuel fraction and is thus representative for the maximum liquid penetration in every time-step.

5.3.4 Spray angle sub-model

The spray angle is the only parameter of the model and determines the control volumes and the general shape of the spray. As described in Section 2.4.2 the spray angle depends on the ambient gas conditions due to turbulence and aerodynamic drag but also strongly depends on the nozzle flow through cavitation.

An empirical spray angle model that was developed by Naber and Siebers [47] and employed in simulation studies in literature [100] is also applied here, next to the measured spray angles.

The spray angle Θ depends on the ratio of liquid fuel density and surrounding gas density according to:

$$\tan\left(\frac{\theta}{2}\right) = c\left[(\frac{\rho_a}{\rho_f})^{0.19} - 0.0043\sqrt{\frac{\rho_f}{\rho_a}}\right] \tag{5.19}$$

with c an empirical calibration constant that depends on the injection equipment. This constant captures the effect of in nozzle flow, while the effects of the ambient gas conditions are explained by the second factor. This relation will be tested in the sensitivity analysis, after the initial model validation.

5.4 Model validation

The implementation of the model was first tested by comparing penetration development to the original simulation. A square-wave injection pulse with a duration of 0.5 ms was simulated, as was done for the results reported by Musculus-Kattke and identical spray penetration development was found. A steady state injection was also simulated and again identical spray penetration was found. These are shown in Figure 5.5, the results are identical and no differences can be observed because the curves completely overlap.

Next, the updated momentum flux equation was evaluated. The penetration was compared and small differences were found: the updated momentum flux equation resulted in an increased penetration by less than 2 % compared to the original implementation, see Figure 5.5. To understand this better, the mean velocity in the spray as a function of penetration distance is compared for the two implementations in Figure 5.6 for a steady injection, 0.8 ms after SOI. Due to increased momentum transfer, the velocity of the new implementation decreases faster close to the nozzle compared to the original which in turn increases the momentum downstream. However, this momentum is distributed over a large fraction of ambient air and does not result in a large velocity increase downstream. The small penetration difference can be observed at the location where velocity drops to zero: 0.8 ms after SOI the difference is 1.6 mm.

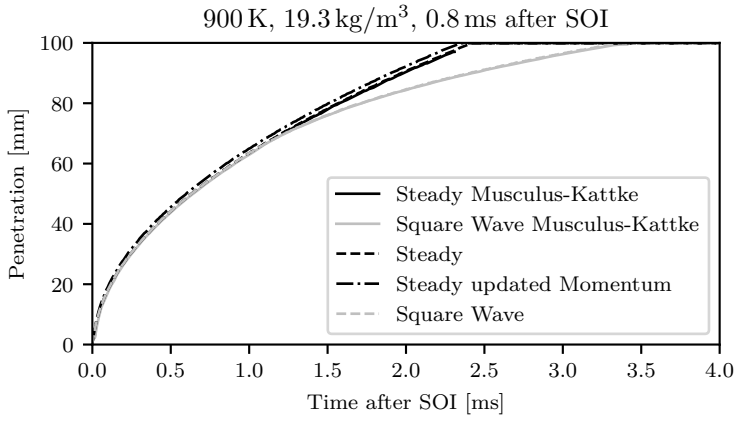

Figure 5.5: Vapor penetration comparison between the model and the original Musculus-Kattke model for a steady injection and a square wave pulse. The penetration with the updated momentum calculation is also shown.

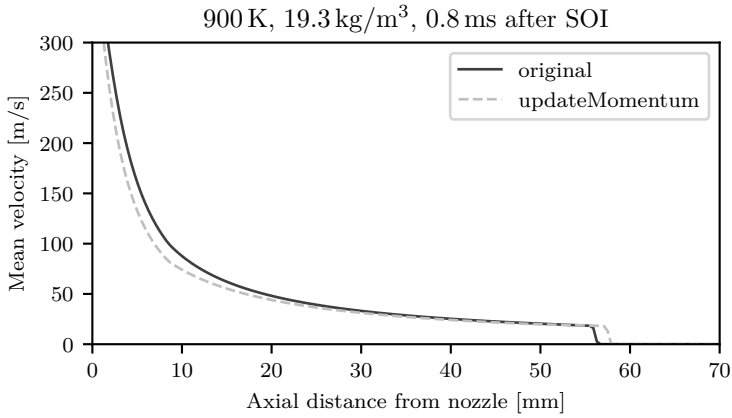

Figure 5.6: Comparison of mean axial velocity in the spray for the original and updated momentum flux for a steady injection.

For the following simulations, the updated momentum implementation is used as this provides more accurate axial velocity profiles, but the effect on penetration speed is small. The model will be applied on a PLN injection system, with variable injection pressure and variable resulting mass flow rate and velocity. Additionally, it was not possible to determine the cavitation in the nozzle hole which influences the injection velocity, as described in Appendix C and Section 5.2. The effect of cavitation on spray development is investigated first, after which the boundary conditions are varied as in the measurement campaign discussed in Chapter 4.

5.4.1 Cavitation effect

The effect of cavitation on the exit velocity is investigated for the eight hole injector at an ambient density of 15.2 kg/m^3, an ambient temperature of 850 K and 800 rpm engine speed. Three situations are evaluated: one with a uniform exit flow which essentially assumes that cavitation does not influence the exit velocity, one with a critical cavitation pressure P_{crit} of 400 bar and one with a P_{crit} of 100 bar, representing increasing influence of cavitation on the exit velocity. During these simulations, the spray angle value is kept constant at the mean measured value for these ambient conditions.

The penetration of vapor in the simulation was detected as the furthest cell that had a momentum flux higher than five percent of the maximum momentum flux and liquid penetration was defined as the furthest

location on the spray center-line where the liquid mass was higher than three percent of the maximum liquid mass, analogous to the Mie scattering liquid detection.

The resulting liquid and vapor penetration from the simulations are compared to the measurement in Figure 5.7. The simulation shows a faster vapor penetration and a lower steady-state liquid penetration when the critical cavitation pressure is decreased. A faster vapor penetration can be expected, as the injection velocity at the nozzle increases due to a lower area coefficient caused by the decreasing critical cavitation pressure. It is important to note that in this simulation, the spray angle was kept constant at its measured value to separate the effect of injection velocity from the primary atomization which can influence the spray angle and penetration significantly: see Section 2.4.2.

Measured vapor penetration initially follows the simulated penetration well, but at approximately 0.5 ms a deviation develops which can be explained by investigating the imposed mass flow rates and needle lifts. The imposed mass flow rate originates from the 1-D hydraulic simulation code and is shown in Figure 5.8 on top. The measured injection pressure in the line was nearly identical to the simulated injection pressure, but the needle position showed a deviation during lifting: the measurement shows a two-stage lift while the simulation predicts a smooth and quick lift. Of course, when the needle is not fully lifted, the pressure in the sac

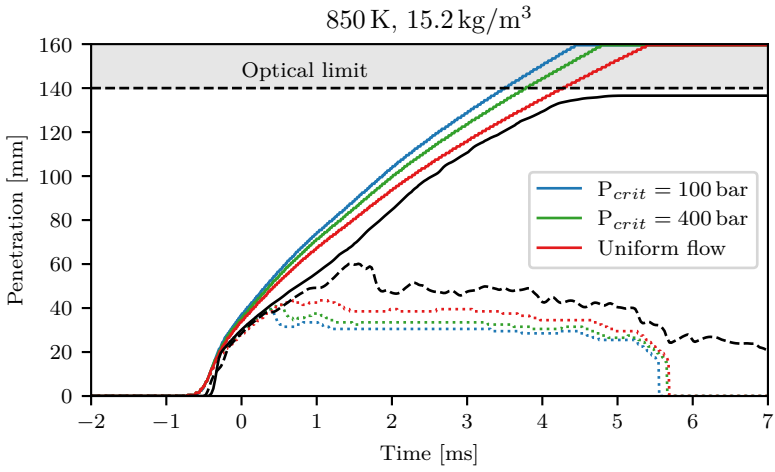

Figure 5.7: Comparison of the simulated vapor (solid lines) and liquid penetration (dashed lines) to the measurement (black) for different critical cavitation pressures.

volume can not fully develop. The mass flow rate will be lower compared to the simulation which is further investigated in the sensitivity analysis of the model.

From approximately 1 ms after SOI, once the effect of the two-stage needle lift is removed, the penetration development of the measurement and the uniform flow simulation case are again similar. The other two simulations, with higher injection velocities, predict a too high penetration speed.

The simulated liquid penetration shows a sudden decreasing value shortly after the EOI while this is not the case for the measurement. As explained in Section 4.3.1, this is caused by falsely detected liquid near the edges of the images from the non-investigated sprays. The true liquid penetration is found to decrease quickly after the EOI, observed for the highest ambient density which suffered less from this falsely detected liquid and shown in Figure 4.7. This was confirmed for the other cases by investigating the images manually.

The liquid penetration decreases with decreasing critical cavitation pressure which is caused by two counteracting effects. Similarly to vapor penetration, the liquid penetration can be expected to increase, due to increasing injection velocity when critical cavitation pressure drops. On the other hand, due to this faster penetration, the volume fraction of fuel decreases quicker as well. As evaporation is assumed to be limited only by the amount of energy that can be entrained into the control volumes, this results in a decreasing liquid penetration with decreasing critical cavitation pressure. Again, the simulation without the inclusion of the

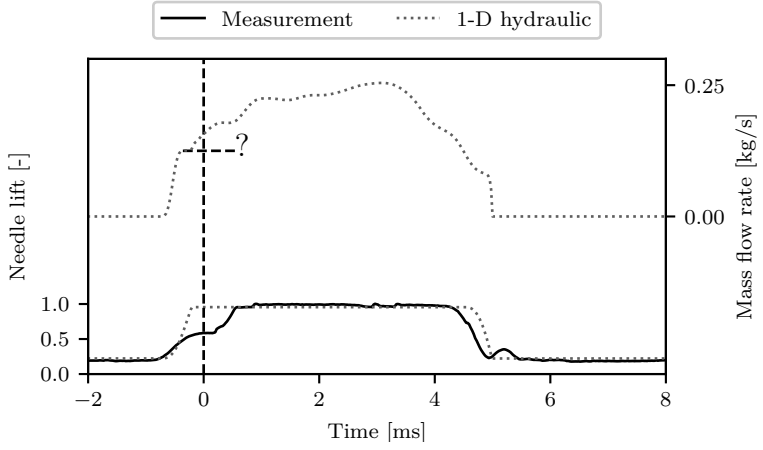

Figure 5.8: Mass flow rate (top) and needle lift (bottom) compared between the measurement and the hydraulic simulation for the eight hole nozzle at 800 rpm *engine speed.*

velocity effect of cavitation provides the best prediction.

5.4.2 Influence of the nozzle

The model should be able to capture the influence of the nozzle configuration on spray development, and this was tested by simulating the eight and ten hole nozzle and comparing this to the respective measurements. The ambient conditions were 22.5 kg/m^3 and 850 K. The comparison of the measured and simulated vapor and liquid penetration is shown in Figure 5.9. The simulation of the eight hole nozzle shows a strong over-prediction of the vapor penetration speed compared to the original measurement (shown in blue), while the liquid penetration of both nozzles is under-predicted by the simulation.

During the description of the measurement results, the measured liquid length at this condition was already questioned. The simulation model provides the results that could be expected based on mixing-limited evaporation. Because of a higher spray angle and a higher ambient density, more air and thus energy is entrained into the spray which results in a shorter simulated liquid length compared to the measurement for both nozzles which indicates that there is either a problem with the model or with the measurement.

This modeling approach does prove to be valid for the other conditions as will be explained below and these results are so remarkable that the measurements were repeated to check the initial results. This repetition shows a much better agreement to the simulation regarding the vapor penetration. The reason for the initial wrong measurement was probably the nozzle hat, that was not mounted perfectly on the injection equipment. A decreasing vapor penetration speed can be observed in the measurement until around 2 ms after SOI. Then, the vapor penetration accelerates again. This can be explained by the two-stage needle lift which will influence the injection velocity.

The simulated liquid penetration however, remains much lower than the one from the measurement. This deviation can be caused by multiple things: a changed optical configuration as described in Section 4.3.1 which could result in changed detection of liquid penetration but a shortcoming in the simulation code is just as well possible. This problem will be further investigated in the sensitivity analysis (Section 5.5.1)

For the remainder of the chapter, the repetition of the measurement will be used to present the results.

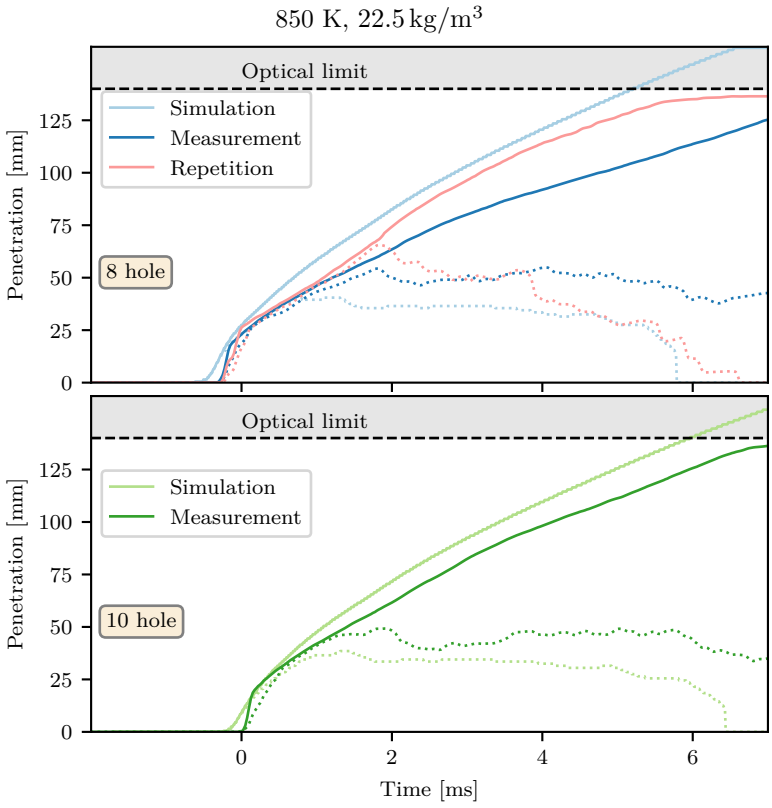

Figure 5.9: Liquid (dashed lines) and vapor (solid lines) penetration compared between the spray measurement and the spray simulation for the eight and ten hole injector.

5.4.3 Influence of ambient conditions

A variation of the ambient temperature is simulated by imposing different initial gas temperatures, together with the measured spray angles at those conditions, in the simulation code for the eight hole nozzle. The resulting vapor and liquid penetration is shown in Figure 5.10.

The liquid penetration changes significantly from approximately 75 mm at an ambient temperature of 700 K to 45 mm at 1000 K. The simulation is able to capture these trends, although the value of the simulation is consistently slightly lower than the measurement result. Two balancing effects are considered to explain this. On the one hand, when evaluating the volume fraction distribution from Figure 5.4 over the radial direction it is clear that the calculated distribution of temperature is not completely

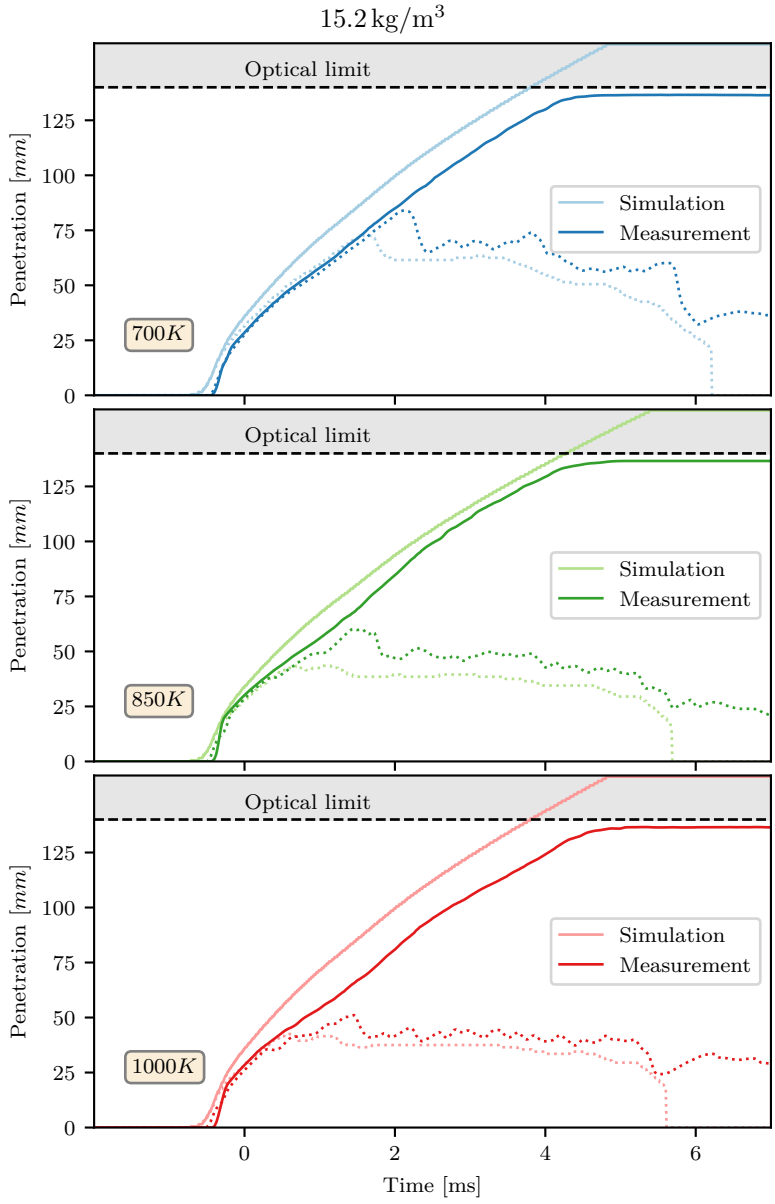

Figure 5.10: Liquid (dashed lines) and vapor (solid lines) penetration compared between the spray measurement and the spray simulation for an ambient temperature variation.

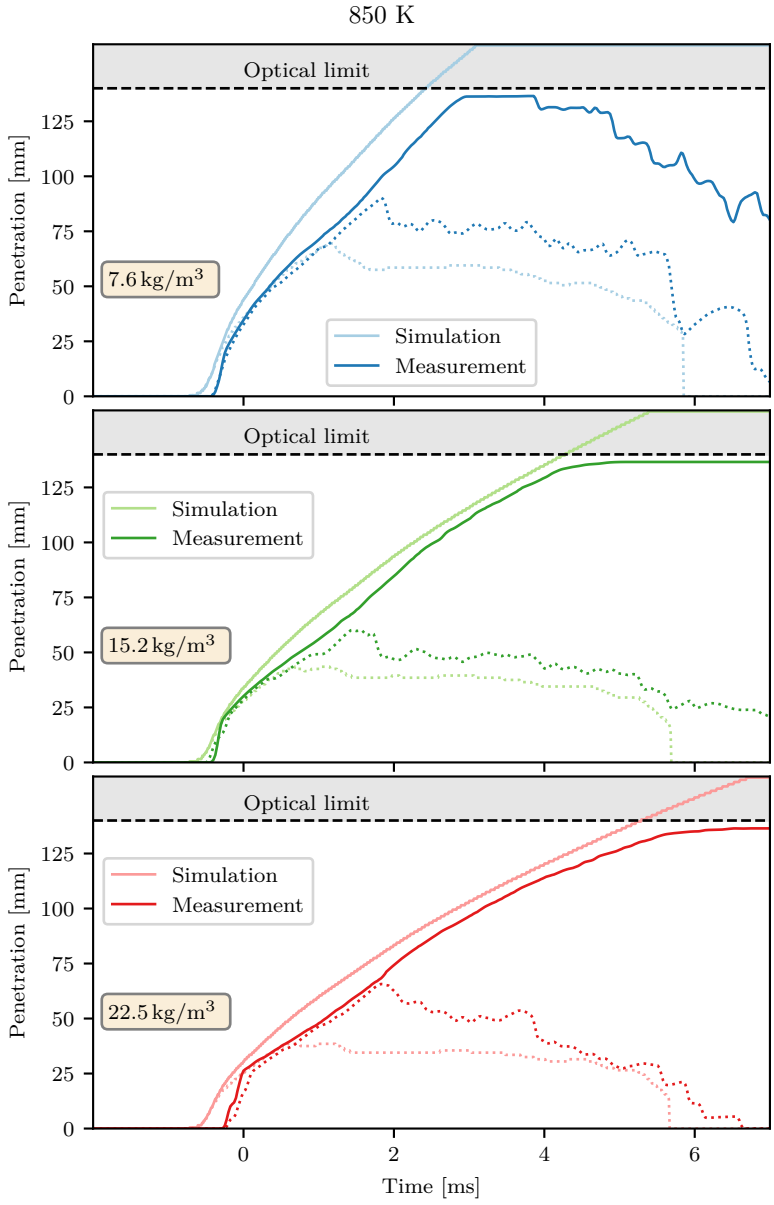

Figure 5.11: Liquid (dashed lines) and vapor (solid lines) penetration compared between the spray measurement and the spray simulation for an ambient density variation.

representative of the true temperature. Ambient gas, transported from the spray edge to the center, will contain a lower enthalpy compared to gas on the spray edge which should result in a lower centerline temperature that increases faster towards the spray's edge compared to the temperature shown in the middle of Figure 5.4. On the other hand, an opposing effect is present: the mixture density increases when considering evaporation due to cooling of the entrained air. This would further increase the mass of entrained air and thus entrained energy. In total, these two simplifications appear to balance each other out.

The vapor penetration does not change, both in the simulation and in the measurements. The difference between simulation and measurement consistently increases at the same timing, due to the stepped needle lift which will be explained in the sensitivity analysis.

A similar variation for ambient density is simulated by imposing the ambient densities from the experiments, together with their respective spray angles. The penetration results are shown in Figure 5.11. Penetration speed is found to increase, both in the simulation and the measurement, when the ambient density decreases. The simulation of the $7.6\,\mathrm{kg/m^3}$ case (on top) shows a similar agreement to the measurement as the $15.2\,\mathrm{kg/m^3}$ (in the middle) with the same reasoning about the deviation in vapor penetration due to the two-stage needle lift.

5.5 Study of marine spray development by simulation

Not all conditions are perfectly captured by the model and therefore this section checks the sensitivity of the model to try and further explain deviations between measurements and the simulation results. After that, the model is employed to find an explanation for the large deviation in penetration speed at high ambient density. Finally, the model is used to estimate local equivalence ratios and temperatures for the reacting sprays and these conditions are then used to estimate the difference between a spray in low and in high oxygen concentrations.

5.5.1 Sensitivity of the spray

Deviation between the measurement and the simulation can be split into three categories: it can be due to differences in the ambient conditions, the injection conditions and the measured spray angle.

Ambient conditions, achieved during the measurements, have been checked in detail in the measurement section (see Table 4.1) and in this sensitivity analysis, the simulated ambient conditions will be varied $\pm 2\sigma$ around the average value for every ambient parameter while keeping the rest of the parameters the same. To avoid the influence of the injection rate a square wave pulse of 0.2 kg/s for a duration of 4 ms is imposed. The spray angle was kept constant at 26°.

The results of the ambient condition variation show so little difference that it is impossible to distinguish the differences on a time-based plot. Instead the elapsed time from the SOI to achieve a 100 mm vapor penetration and the steady state liquid length are shown numerically in Table 5.1. These results show that, within the experimental uncertainty,

Table 5.1: Sensitivity analysis of ambient conditions.

		Mean	Variation	$t_{pen} = 100$ mm [ms]	Liquid length [mm]
ρ	[kg/m^3]	15.07	+0.16	2.12	37.5
			-0.16	2.10	39.5
T	[K]	856	+22	2.11	36.5
			-22	2.11	39.5
C_p	[kJ/kgK]	1.11	+0.05	2.11	36.5
			-0.05	2.11	39.5

Table 5.2: Sensitivity analysis of injection parameters.

		Mean	Variation	$t_{pen} = 100\,\text{mm}$ [ms]	Liquid length [mm]
D	[mm]	0.44	10 %	3.56	42.5
			−10 %	3.16	34.5
C_d	[-]	0.75	10 %	3.18	38.5
			−10 %	3.57	38.5
ρ_f	[kg/m^3]	750	6.7 %	2.18	39.5
			−6.7 %	2.04	37.5

liquid penetration and vapor penetration do not change and that it was indeed valid to calculate an ensemble average of the spray parameters.

The injection conditions result from the 1-D hydraulic simulation code and are validated indirectly with line pressure and needle lift for certain operating points but have some shortcomings: the stepped needle lift is not reproduced in the simulation code and the area flow coefficient is not obtained directly. The effect of the area flow coefficient was already discussed above, in Section 5.4.1. The influence of the stepped needle lift is investigated here by imposing a constant high, a constant low and a stepped injection rate in the simulation code as shown on the bottom of Figure 5.12. This was based on the simulated mass flow rates, shown in Figure 5.8 where at approximately half the needle lift the mass flow rate was found to be reduced by approximately 1/3rd of the maximum value.

The penetration results are shown on top in Figure 5.12 and this provides evidence that the above explanation for the deviation of the eight hole nozzle results is indeed correct. Due to a lower initial mass flow rate the penetration is initially slower until the mass flow rate increases which causes the penetration speed to increase. The penetration speed first increases to a value higher than when starting with the high flow rate, i.e. it catches up to the high flow rate, until it enters fresh, stagnant ambient air. The penetration speed then becomes equal to the high flow rate case, leaving a small time delay between the stepped and the high flow rate just as in the measured penetration of the eight hole nozzle. The steady state liquid length shows no difference.

To finalize the injection parameter analysis, the influence of the nozzle hole diameter, the discharge coefficient and the fuel density is summarized numerically in Table 5.2 with the time from SOI until the vapor penetration reaches 100 mm and with the steady state liquid length for a ±10 % variation of the diameter and the discharge coefficient while keeping the rest of the simulation parameters constant.

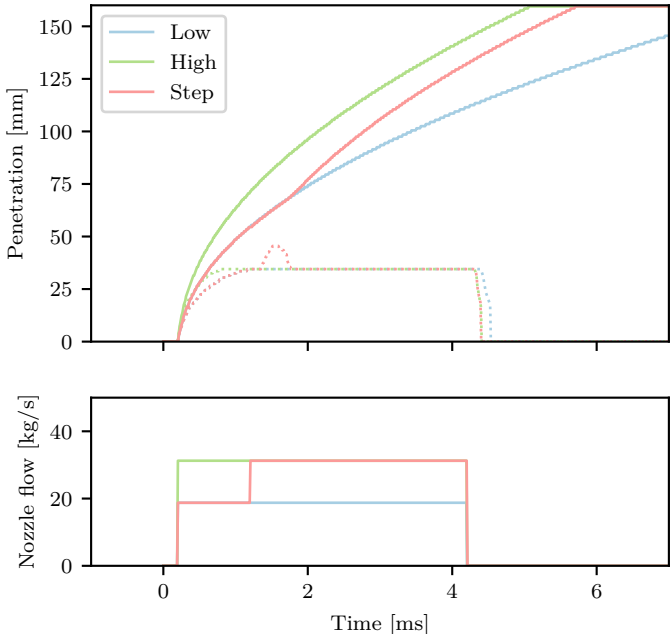

Figure 5.12: Liquid (dashed lines) and vapor (solid lines) penetration for a low constant injection rate, a high constant injection rate and an injection rate that steps from low to high flow rate.

When the hole diameter increases while keeping the fuel mass flow rate constant, the vapor penetration speed decreases due to a lower injection velocity. This lower injection velocity also results in higher fuel concentrations near the nozzle. A higher fuel fraction near the nozzle results in a lower amount of entrained air and this results in a lower equilibrium temperature and thus a longer liquid length. By using the same reasoning, the influence of the fuel density can be explained. An increasing fuel density results in a decreased exit velocity at the nozzle when mass flow rate is kept constant and this results in the same conclusions.

When increasing the discharge coefficient, essentially increasing the mass flow rate and velocity out of the nozzle at equal rates (in this case neglecting the area coefficient), the liquid length remains constant as the fuel concentration near the nozzle remains the same because of this simultaneous increase in nozzle exit velocity and mass flow rate. The penetration time is affected, decreasing with increasing discharge coefficient due to the increased nozzle exit velocity.

To end the sensitivity analysis, the spray angle influence will be investigated: this is a direct input parameter of the model and the measurement shows variation both over time and when progressing from the nozzle to the end of the combustion chamber. Currently, the spray angle in the simulation is assumed to be constant, both over time and in the axial direction. From the spray measurements the spray angle is found to have a high initial value, up to 50°, partially caused by the detection method because of the limited size of the detected spray but also due to high initial deceleration of the flow where slowed down fluid is pushed aside by freshly injected fluid, increasing the initial spray angle. The measured spray angle is found to decrease slowly during the progress of the injection.

A spray angle variation between 40° and 20° is simulated with a constant spray angle assumption to try to estimate both near-nozzle and far-field influences without further complicating the simulation code. Liquid and vapor penetration results are shown in Figure 5.13. A strong influence, both on the vapor and liquid penetration is found. With smaller spray angles, less ambient gas can be entrained into the control volumes which increases the resulting spray velocity and decreases the entrained energy, necessary for vaporization. This results in faster vapor and longer liquid penetration.

With this sensitivity analysis, the spray angle model can be evaluated as well. The spray spreading angle is found to be invariant with temperature and varies with ambient density. A scaling law was proposed by Naber and Siebers [47] with the equation given in Equation (5.19). The tuning

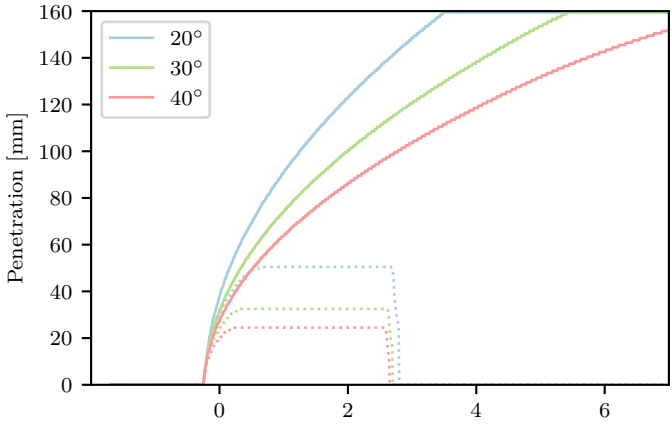

Figure 5.13: Simulated liquid (dashed lines) and vapor (solid lines) penetration for a variation in spray angle.

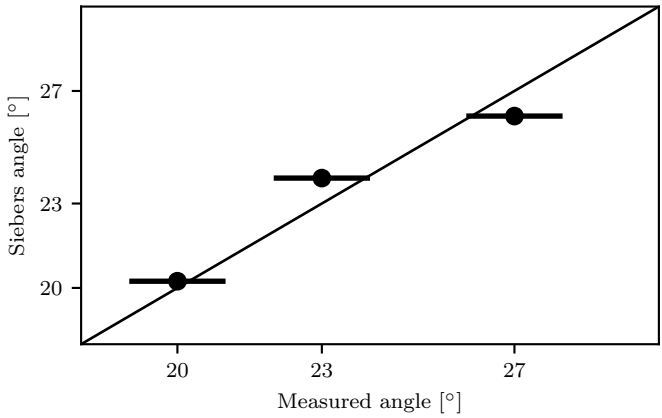

Figure 5.14: Predicted spray angle according to Equation (5.19) *as a function of measured spray angle, the perfect prediction is shown with a solid line.*

constant c was fitted to minimize the sum of squared errors of the obtained spray angles for the ambient density variation for the eight hole nozzle.

The predicted spray angle as a function of the measured spray angle is shown in Figure 5.14 and the agreement is found to be good. The variation of the measured spray angle during the steady-state injection period is estimated to be $\pm$ 1° and this error is also shown on the figure. The scaling law is thus able to capture the influence of the ambient density on the spray angle sufficiently. The largest error is 0.9° which would result in a limited decreased penetration.

5.5.2 High density simulation

From the above sensitivity analysis the only options that might explain the liquid length result for the eight hole nozzle at high ambient density are uncertainties in the nozzle diameter and the fuel density. Vapor penetration was predicted well, but the simulated liquid length was shorter than measured. As the same fuel was used to execute all the experiments and because fuel temperature was well controlled, the fuel density influence cannot be used to explain the difference.

From the repetition, it was found that the original measurement was faulty in some way. This was probably caused by a slight misalignment of the nozzle hat. However, although the vapor penetration was now correctly predicted, the liquid length measurement remained large.

While the diameter has a large influence on both the vapor and liquid penetration, it cannot explain the extreme difference completely.

Both the fuel density and diameter effects on liquid and vapor penetration rely on the balance between the nozzle's exit velocity and mass flow rate. A theoretical explanation could be the change in ratio of the nozzle's exit velocity to the mass flow rate. When the velocity decreases for constant mass flow rate, the liquid length increases while the vapor penetration decreases. This could happen when the nozzle flow would transition from strongly cavitating to a more uniform flow at the nozzle's exit due to increasing back pressures.

However, from the above analysis of cavitating flow, it has to be concluded

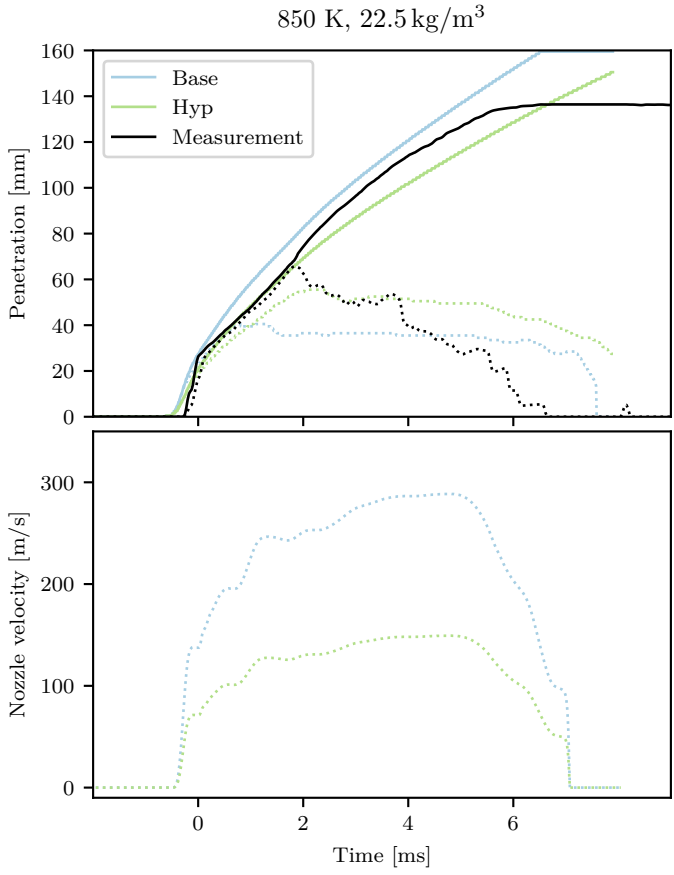

Figure 5.15: Effect of the reduced velocity hypothesis for the eight hole nozzle at high ambient density conditions, nozzle exit velocities shown on the bottom.

that exit flow velocity is already uniform for lower back pressures. Increasing the back pressure more will thus not have an influence on the velocity to mass flow ratio.

Neglecting the physical possibility of the following hypothesis, the exit velocity in the simulation model is scaled artificially until the simulated liquid penetration matches the measured liquid penetration. The resulting vapor and liquid penetration is shown on top of Figure 5.15, the bottom shows the injection velocity that was employed in the respective simulations. When injection velocity is decreased by 40 %, agreement becomes reasonable. This is the only way to explain the obtained measurement results with the current model.

The ten hole nozzle does not show such high deviations with higher ambient densities and the deviations that are present can be plausibly explained by hole diameter variation and measured spray angle variation.

The reasons for a lower evaporation rate at a certain operating point are currently not completely understood. Either the model fails to capture a certain aspect of the spray development or the injection boundary conditions that resulted from the 1-D simulation code are not completely accurate.

5.5.3 Reacting spray condition

During the analysis of the reacting spray measurements, the spray angle was found to suddenly increase after a certain time delay. This time delay decreased with increasing oxygen fraction. A certain delay after this spray angle increase, broadband luminosity first increased at the location where the spray angle widened and this luminosity then rapidly spreads downstream. The delay between the spray angle increase and luminosity increase also decreased with increasing oxygen fraction. In this section, the local equivalence ratio and temperature are estimated to explain these measurements.

The equivalence ratio and temperature were calculated at each radial location by employing the assumed fuel fraction profiles and repeating the calculation procedure as described in Section 5.3.3 where the evaporation rate was calculated. This results directly in the temperature profile in the radial direction. By repeating the procedure for all control volumes and several times after SOI, the development of temperature can be tracked in space and time. The fuel-air ratio is then calculated as:

$$FA = \frac{m_f}{m_a} = \frac{X_{vap}\rho_{vap} + X_{liq}\rho_{liq}}{(1 - X_{vap} - X_{liq})\rho_{am}} \tag{5.20}$$

where X_{liq} is the liquid volume fraction, X_{vap} the vapor volume fraction, ρ_{liq} the liquid density, ρ_{vap} the vapor density and ρ_{am} the ambient

density. The fuel-air ratio is converted to the equivalence ratio by:

$$\Phi = FA/FA_{stoich} \tag{5.21}$$

where FA_{stoich} depends on the initial oxygen concentration.

The simulated sprays are shown for four times after SOI in Figure 5.16 at two different O_2 concentrations. Eight sprays are shown in the figure, where the left column is the 13 % O_2 concentration and the right column is the 21 % O_2 concentration. The top row images show the spray at 0.5 ms after SOI, the second row shows images of the spray at 1.0 ms after SOI, the third row shows images of the spray at 1.5 ms after SOI and the bottom row shows the spray 3.5 ms after SOI. The top half of the spray shows the local temperature of the spray, while the bottom half shows the equivalence ratio.

Overall higher equivalence ratios are visible for the lowest oxygen concentration as can be observed by the larger zone with a very high equivalence ratio ($\Phi > 4$) near the nozzle, and by a moderately higher equivalence ratio downstream of the liquid length. This higher equivalence ratio is caused only by the amount of dilution, which in the lowest oxygen case is higher. The temperature distributions do not change between different oxygen concentrations because the heat capacity and density of the ambient gas was considered to remain constant, just as in the measurements.

To understand the spray angle widening effect and soot luminosity difference between the high and low ambient oxygen concentration, the time development of the chemical reaction proces that was simulated by Musculus in [58] is summarized here, expanded from Section 2.4.3. The simulation uses a set of characteristic chemical reactions and species. Musculus used this chemical reaction scheme to simulate the combustion of n-heptane.

The first simulation that was described in [58] starts with a mixture temperature of 787 K, obtained by adiabatic mixing of an initial gas temperature of 840 K and fuel temperature of 363 K and an oxygen concentration of 12.7 %. The first observation is a two-stage combustion with the stages governed by temperature: a pool of first-stage intermediate species builds during the first-stage ignition delay and when temperature reaches 850 K this pool decomposes rapidly, causing a small amount of heat release and producing second-stage intermediate species. The concentration of these second-stage intermediate species increases until temperature reaches 1000 K. Again, the reaction balance shifts and the second-stage intermediate species are now rapidly converted into OH radicals which are able to accelerate the overall oxidation rate resulting in the second-stage combustion in which most of the chemical energy is released.

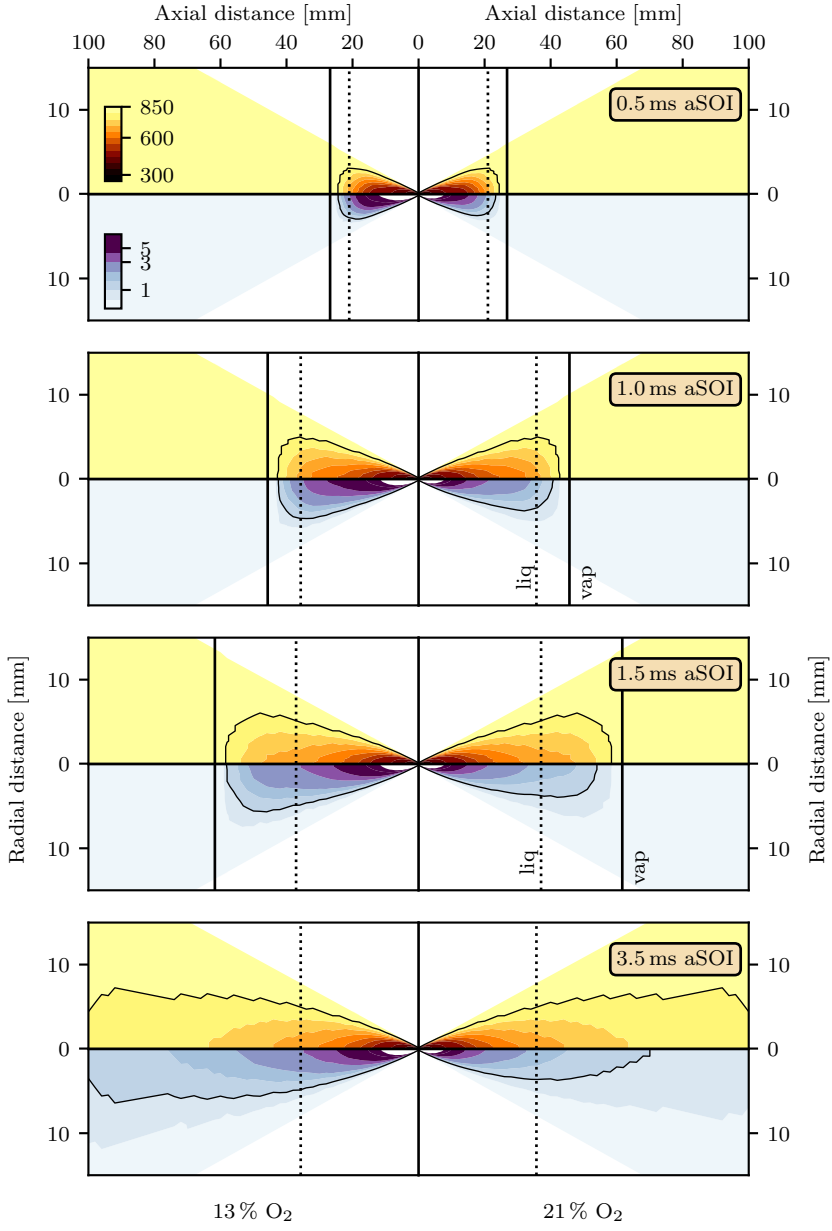

Figure 5.16: Local temperature (top half of the spray) and equivalence ratio (bottom half of the spray) for a spray simulation with 13 % *(left) and* 21 % *(right) ambient* O_2 *for* 0.5 ms, 1.5 ms *and* 3.5 ms *after SOI, timings indicated in box, vapor and liquid penetration indicated with solid and dashed vertical lines.*

When varying the equivalence ratio and while keeping the oxygen concentration constant, it is found that a fuel-lean mixture ($\Phi = 0.7$) causes a faster first-stage ignition, i.e. the pool of first-stage intermediate species is quickly converted to second-stage intermediate species, but then the second-stage ignition takes longer. Richer mixtures ($\Phi = 2$) on the other hand have a longer first-stage ignition that progresses faster into second-stage ignition. The faster first-stage ignition with more fuel-lean mixtures was found to be caused by an increased initial mixture temperature due to the adiabatic mixing assumption. When the initial mixture temperature was kept constant, the first-stage ignition timing showed little difference. The decreased second-stage ignition delay with higher equivalence ratio is explained by the increased temperature rise that occurs during the first-stage ignition of a rich mixture, shortly after first-stage ignition the mixture temperature is already approaching 1000 K and second-stage ignition thus quickly follows.

The spray angle widening, observed in the reacting spray measurements, started around 1.5 ms after SOI for 13 % O_2 and 1 ms after SOI for 21 % O_2. Now, this spray angle widening can be coupled to the equivalence ratio, shown in Figure 5.16. At 1 ms after SOI, equivalence ratio reaches values near stoichiometry in a wide region of the spray while ambient temperature at those equivalence ratios is still high. From the closed reactor simulations, it is known that the first-stage ignition delay mainly depends on mixture temperature. Regions close to the nozzle have a temperature close to the fuel temperature and thus a high first-stage ignition delay. As time progresses and the fuel spray is transported further into the combustion chamber, the mixture temperature increases and the mixture starts to lean out quicker for higher oxygen concentrations.

The comparison between the two oxygen concentrations can only be made by understanding the dilution effect of the oxygen concentration: this is the main difference between the closed reactor simulations, described before, and these simulations. At equal equivalence ratio, the 13 % O_2 case is more diluted than the 21 % case, essentially meaning that the first-stage ignition will result in a lower temperature increase.

For the lowest oxygen concentration, dilution (indicated by higher equivalence ratios) limits the transition from first to second-stage ignition because the temperature increase is limited. On the other hand, for the higher oxygen concentration, the first-stage ignition quickly develops into the second-stage because of low dilution, rapidly releasing energy. This energy release results in the spray angle widening and as a larger fraction of the spray at 21 % O_2 reaches lower equivalence ratios quicker, the spray angle increase happens faster.

For the 13 % O_2 concentration higher equivalence ratios are maintained

for longer which reduces the initial temperature increase, delaying second-stage combustion. On the bottom plots of Figure 5.16 equivalence ratios higher than one can be observed far downstream of the liquid length on the left-hand side, indicating possible sources of rich and incomplete combustion, while this is not the case for a higher O_2 concentration. This is caused by a relatively long injection, decreasing the injection duration will reduce these high equivalence ratios by increased mixing after the end of injection such as in [57] but this reduces the maximum power that can be attained with the engine as well.

5.6 Summary

In Chapter 2, a commercial engine simulation code was employed to predict emissions in a marine engine. While general trends could be reproduced, some deviations between the simulated and measured emission appeared. Clearly, due to the underlying model assumptions, not all physics of the injection process were captured.

Direct comparison of the commercial simulation model to measurements was impossible, because of hidden intermediate results and tuning constants. To improve understanding of the spray measurement results, a 1-D spray simulation model was developed in this Chapter, based on models available in literature that were applied on smaller common rail injection systems.

Despite the strong assumptions of the model, it is able to capture vapor and liquid penetration with varying ambient conditions for this marine PLN injection system. Higher ambient densities showed deviations between simulation and measurement. The measurements were repeated because of this large deviation and the original measurement was found to contain an error. However, measured liquid length remained higher than in the simulation. A sensitivity analysis showed that the most likely explanation for this deviation lies in an imbalance of the nozzle mass flow rate and the momentum flux. Of course, it is possible that some of the model assumptions are too strong for this operating point.

Finally, the spray angle increase observed for reacting sprays was coupled to calculated local equivalence ratio for two ambient oxygen concentrations.

6

Revisit: Death of the Internal Combustion Engine?

'Everything is theoretically impossible, until it is done."

- Robert A. Heinlein -

6.1 Conclusions of the present work

Emissions from a medium-speed marine engine are becoming more and more regulated to improve air quality, reaching levels on par with emission legislation for automotive engines. Marine engines differ from automotive engines in several ways: combustion chambers are much bigger, combustion duration is longer and injection technology can differ as well. With 1-D engine simulations it was shown that ambient conditions in the cylinder are comparable between marine engines and on-road truck applications.

On the other hand, the effect of larger injection equipment and different injection technology on spray development and the following combustion process is currently not well documented. Additionally, combustion timing in a marine diesel engine is currently closely coupled to the SOI timing which results in the well-known high emission of toxic products such as soot and NO_x. By diluting the combustion, it would be possible to achieve lower overall temperatures in the combustion chamber which increases ignition delay. This would result in additional mixing which would decrease both soot and NO_x emissions. This low temperature combustion method is currently under investigation for automotive applications, but it is unknown how the marine injection system interacts with this advanced combustion scheme. This was studied as an example during the measurement campaign.

To understand the process, starting from the liquid fuel in the injection system to a burning spray in the combustion chamber, an existing optically accessible combustion chamber, the GUCCI setup, was further developed. It is now possible to vary the ambient conditions in a repeatable way to obtain specific ambient boundary conditions.

Two optical, high speed measurement techniques were used in the combustion chamber: a schlieren technique to visualize spray vapor boundaries and a Mie scattering technique to visualize liquid spray penetration. The lighting of both these techniques was alternated and by synchronizing the exposure of a a high speed camera to the lighting of each technique both vapor and liquid spray development could be measured in a single experiment. After obtaining a sequence of images a software algorithm was employed to detect spray vapor and liquid penetration.

A database of spray measurements was collected for a range of ambient boundary conditions for two different nozzles. The effect of an ambient density and temperature variation on spray vapor and liquid penetration was studied within current and possible future boundary conditions. Ambient density was varied between $7.6\,\mathrm{kg/m^3}$ and $22.5\,\mathrm{kg/m^3}$, ambient temperature was varied between 700 K and 1000 K and finally oxygen

concentration was varied between 21 % and 13 %.

The obtained vapor and liquid penetration variations were compared for the different tested ambient conditions. The trends were found to be similar to results for automotive applications. Liquid penetration for the highest ambient density was higher than could be expected from available literature.

For the reacting measurements, two distinct combustion stages could be observed for the lowest oxygen concentration. When increasing the oxygen concentration these two stages started to overlap more and more. Both these effects are in line with effects reported in literature.

A commercial, closed-source engine simulation model was unable to reproduce engine performance perfectly. A deviation between low and high engine loads was observed. To identify the cause of this, an in-house 1-D simulation model was employed to describe the spray penetration and evaporation process in more detail. To simplify the calculations, several assumptions were made of which the two most critical ones are repeated here. By the first assumption, fuel volume fraction and velocity distribution are evaluated using radial profiles over the width of the spray. This was based on gas jet theory, and was validated in literature for fuel sprays representative for automotive applications. The second assumption is that evaporation is limited only by the amount of entrained energy by hot ambient air and that inter-phase heat transfer is not the limiting step.

This new simulation model was compared with the spray measurements for the measured ambient density and temperature variation. Simulated vapor and liquid penetration agreed well with the measurements for an ambient temperature variation and for the low and medium ambient density which confirms the validity of the above hypotheses of the radial profiles and the mixing-limited evaporation.

However, for the highest density, the simulated vapor penetration was initially oo fast and steady state liquid penetration was too low compared to the measurements. After repeating the measurement, it was found that the original measurement contained an error and the simulation model allowed to detect this. However, the measured liquid length remained longer than in the simulation. A sensitivity analysis showed that the cause of this deviation could be attributed to a combination of three possibilities: an imbalance of the nozzle mass flow rate and the momentum fluxor a physical process that is not captured in the model.

Finally, a lower oxygen concentration results in a higher dilution ratio at zones with a temperature that is sufficiently high for first-stage ignition of the diesel spray. This results in a lower temperature increase during first-stage ignition and postpones the high temperature heat release as

would happen in a low temperature combustion strategy for automotive applications.

The marine injection system thus does not fundamentally limit obtaining a low temperature combustion strategy by the injection process, but rather by a lack of flexibility. The injection timing of a marine PLN injection system is fixed mechanically over the whole operating range of the engine and cannot be adjusted during engine operation. From on-road applications it is known that this flexibility is necessary during low temperature combustion operation to control combustion timing continuously to account for ambient temperature variations or during a cold-start of the engine. Once the flexibility of a marine injection system can be improved, it would be possible to try implementing new combustion schemes.

6.2 Recommendations

With this optical study of a marine injection system some building blocks for future research were provided. The gaseous boundary conditions can now be controlled very well. A 1-D spray simulation code allowed to identify a measurement error, but combustion could not be implemented during this work.

Some (and new) questions remain though, and this results in the following recommendations:

1. During this work, a common rail design was built by several thesis students. Because the common rail injector was unavailable, the measurement set could not be started. It would be very interesting to add the flexibility of a common rail injector to the current measurement setup. Injection pressures are then independent of injection duration and engine speed which would open the window of new combustion modes further. Last but not least the measurement procedure would be simplified greatly: synchronization could be done directly, without assuming engine speed during the injection as now needs to be done for the PLN injection system.

2. Very small injection quantities were not investigated in this work. These are employed during low load operation, but also as an ignition source for dual-fuel engines. Dual-fuel combustion, where a small amount of direct injected fuel ignites a premixed fuel-air mixture, currently receives much attention in the marine sector. This can replace large fractions of fossil fuel by mixing in an alternative fuel, for example in the intake air, making a gradual

introduction of renewable fuels possible. These small injections suffer from very low injection pressure and, depending on the specific injector, a partial needle lift. It would be interesting to expand the measurement set with this type of injections.

3. This recommendation follows upon the previous one, but is more complicated. During dual-fuel combustion a small conventional spray interacts with a fuel air-mixture: the spray will develop into a propagating flame which compresses end gas that could be prone to knock. The combustion interaction can be studied in the combustion chamber, but would require modifications to obtain a high enough ambient temperature. The pre-combustion technique can then not be used anymore in its current configuration. One option is increasing the electrical heating up to 180 °C and using a fuel with a low ignition temperature, such as diethyl ether.

4. In the path to zero-fossil fuels (Section 1.1.3) explanation, a fuel was looked for that could store energy easily and be transported from locations where abundant renewable energy is available to locations where a large amount of energy is necessary. Now only standard winter diesel and n-dodecane were tested, but other and renewable fuels could be introduced into the setup to understand how fuel properties would influence spray development. As renewable fuels typically have some challenging properties, e.g. corrosive and low viscosity, for the fuel injection system, this will require significant adjustments.

5. A further validation of the injection rate and velocity out of the nozzle hole would be interesting, e.g. by the development of a new hydraulic test rig. This will provide the actual velocity out of the nozzle hole that was identified in the sensitivity analysis to be responsible for the eight hole nozzle stepped vapor penetration. The measurements of velocity and injection rate can be coupled to the GT-Power simulation code, likely improving the prediction of heat release rate over the whole operating range as well.

6. One high ambient density measurement set had to be discarded. This was likely caused by a misalignment of the nozzle hat which isolates one of the sprays from the nozzle. The spray impacted the walls of the nozzle hat and the spray characteristics were changed because of that. To avoid this in the future, the nozzle hats should be adjusted, e.g.: with a mechanical alignment slot. This can also be avoided by employing a common rail system. There, injection pressure is regulated by the pump, so single hole nozzles are no problem. In a PLN system, injection pressure is obtained by flow resistance.

7. A final recommendation is about the simulation code: the application is now limited to liquid and vapor penetration but it would be possible to extend the simulation to reacting conditions as well. It is currently possible to calculate temperature and species concentrations in the whole spray. This could be coupled to a chemical kinetics simulation which would directly provide an estimation of emission production in the spray.

A

Determination of the gaseous fractions

In this appendix, the derivation of the gas partial pressures is given. It starts from the desired ambient properties at the start of injection. The main equation are taken from the thesis of Jonas Galle [67] but were updated for new gaseous fuels and ignition quality. Next, the hardware and software improvements are described.

A.1 Introduction: target condition

The pre-burn or pre-combustion method has been evaluated in the past as a reliable method to create engine-like conditions in a constant volume combustion chamber for optical spray measurements and is widely used [50, 76, 77]. The properties at start of injection are determined by carefully choosing the gas mixture composition prior to ignition. A stirring fan is used continuously during the filling process to avoid any inhomogeneities. Two spark plugs with high capacity coils allow the mixture to ignite. A piezo-electric pressure sensor monitors the cooling down process by measuring the bulk pressure. Five gases are used for the initial gas mixture which allows to define five properties at start of injection. The most important ambient gas properties which will influence the spray (and combustion) are:

- amount of oxygen [vol$\%_{b,O_2}$]: influences the oxidation process
- temperature at SOI: influences the evaporation process
- density [ρ_u] at SOI: influences the spray break-up process
- heat capacity at SOI: influences the evaporation process
- fraction of hydrogen: influences the range of heat capacity that can be achieved by varying the Argon concentration and the ignition quality

A.2 Continuity equations

Gas properties such as heat capacity, enthalpy, and saturation pressure are considered temperature dependent but independent of pressure. Thermodynamic properties are calculated from Nasa's polynomial coefficients [101]. A set of 5 equations and 5 unknowns needs to be resolved:

- (eq. 1) : expression for the fraction of hydrogen (deals with the desired heat capacity)
- (eq. 2) : expression for the total mass (deals with the desired density)
- (eq. 3) : expression for the amount of oxygen
- (eq. 4) : conservation of enthalpy (deals with the desired temperature)

- (eq. 5) : expression for the desired heat capacity

Assumptions for the pre-combustion process are:

- complete combustion (no soot, CO or H_2 in the final products)
- no NO_x or dissociation of N_2 and O_2. The amount of dissociation products is smaller than the experimental error or accuracy
- no dissociation
- $\lambda \geq 1$

The pre-combustion process (without dissociation) can be described by

$$a.C_2H_2+b.H_2+c.O_2+d.N_2+e.Ar \rightarrow f.CO_2+g.H_2O+h.O_2+d.N2+e.Ar \tag{A.1}$$

The coefficients *a*-*h* $[mol]$, need to be determined. In the following, the index $_u$ represents the unburned situation, the index $_b$, the burned situation. The relation between the moles of C_2H_2, H_2, O_2, H_2O and CO_2 are given by the reaction mechanism:

$$C_2H_2 + \frac{5}{2}O_2 \rightarrow 2.CO_2 + H_2O \tag{A.2}$$

$$2.H_2 + O_2 \rightarrow 2.H_2O \tag{A.3}$$

The burned masses of the components written as a function of the mass of C_2H_2 and H_2 become:

$$m_{b,CO_2} = 2.M_{CO_2}\frac{m_{u,C_2H_2}}{M_{C_2H_2}} \tag{A.4}$$

$$m_{b,H_2O} = M_{H_2O}\frac{m_{u,C_2H_2}}{M_{C_2H_2}} + 1.M_{H_2O}\frac{m_{u,H_2}}{M_{H_2}} \tag{A.5}$$

$$m_{b,O_2} = m_{u,O_2} - \frac{5}{2}M_{O_2}\frac{m_{u,C_2H_2}}{M_{C_2H_2}} + \frac{1}{2}.M_{O_2}\frac{m_{u,H_2}}{M_{H_2}} \tag{A.6}$$

Equation 1: fraction of hydrogen

As hydrogen only produces water after combustion it is possible to influence the achievable range of the heat capacity by varying the other gases: this is an input parameter that should be specified by the operator:

$$n_{H_2} = a.n_{C_2H_2} \tag{A.7}$$

$$0 = a.\frac{m_{u,C_2H_2}}{M_{C_2H_2}}.M_{H_2} - m_{H_2}$$

Equation 2: conservation of mass

The conservation of mass equation is used to achieve the target density $\rho_{\mathbf{u}}$:

$$m_{u,C_2H_2} + m_{u,H_2} + m_{u,O_2} + m_{u,N_2} + m_{u,Ar} = m_{tot} = \rho_{\mathbf{u}} V_{chamber} \quad \text{(A.8)}$$

Equation 3: expression for the amount of oxygen after pre-combustion

The volume percentage of oxygen $\text{vol}\%_{b,O_2}$ is equal to the mole fraction of the system:

$$n_{b,O_2} = \mathbf{vol}\%_{\mathbf{b,O_2}}.n_{b,tot} \quad \text{(A.9)}$$

with

$$\begin{aligned} n_{b,tot} &= n_{b,CO_2} + n_{b,H_2O} + n_{b,O_2} + n_{b,N_2} + n_{b,Ar} \\ n_{b,tot} &= (2n_{u,C_2H_2}) + (n_{u,C_2H_2} + n_{u,H_2}) + \\ &\quad (n_{u,O_2} - \frac{5}{2}n_{C_2H_2} - \frac{1}{2}n_{u,H_2}) + \\ &\quad n_{u,N_2} + n_{u,Ar} \end{aligned} \quad \text{(A.10)}$$

Substitution of Eq. A.9 in Eq. A.10 results in:

$$\begin{aligned} [n_{u,O_2} - \frac{5}{2}n_{u,C_2H_2} - \frac{1}{2}n_{u,H_2}] &= vol\%_{b,O_2}.[(2n_{u,C_2H_2}) \\ &\quad +(n_{u,C_2H_2} + n_{u,H_2}) \\ &\quad +(n_{u,O_2} - \frac{5}{2}n_{u,C_2H_2} - \frac{1}{2}n_u H_2) \\ &\quad +n_{u,N_2} + n_{u,Ar}] \end{aligned} \quad \text{(A.11)}$$

Writing Eq. A.11 as a function of the unburned conditions results in $A.12$.

$$\begin{aligned} 0 &= \frac{m_{u,C_2H_2}}{M_{C_2H_2}}\left[\frac{5}{2} + \frac{1}{2}vol\%_{b,O_2}\right] \\ &\quad +\frac{m_{u,H_2}}{M_{H_2}}\left[\frac{1}{2} + \frac{1}{2}vol\%_{b,O_2}\right] \\ &\quad +\frac{m_{u,O_2}}{M_{O_2}}\left[vol\%_{b,O_2} - 1\right] \\ &\quad +\frac{m_{u,N_2}}{M_{N_2}}\left[vol\%_{b,O_2}\right] \\ &\quad +\frac{m_{u,Ar_2}}{M_{Ar}}\left[vol\%_{b,O_2}\right] \end{aligned} \quad \text{(A.12)}$$

Equation 4: conservation of energy

The internal energy of the system before and after combustion is conserved and assuming adiabatic combustion, the conservation of energy can be written as:

$$\begin{aligned} m_{u,C_2H_2}u_{C_2H_2} + m_{u,H_2}u_{H_2} + m_{u,O_2}u_{O_2} + m_{u,N_2}u_{N_2} + m_{u,Ar}u_{Ar} = \\ m_{b,CO_2}u_{CO_2} + m_{b,H_2O}u_{H_2O} + m_{b,O_2}u_{O_2} + m_{b,N_2}u_{N_2} + m_{b,Ar}u_{b,Ar} \\ = \left(2\frac{m_{u,C_2H_2}}{M_{C_2H_2}}\right) M_{CO_2}.u_{u,CO_2}(T_b) + \\ \left(\frac{m_{u,C_2H_2}}{M_{C_2H_2}} + \frac{m_{u,H_2}}{M_{H_2}}\right).M_{H_2O}.u_{u,H_2O}(T_b) + \\ \left[\frac{m_{u,O_2}}{M_{O_2}} - \frac{5}{2}\left(\frac{m_{u,C_2H_2}}{M_{C_2H_2}}\right) - \frac{1}{2}\left(\frac{m_{u,CH_4}}{M_{CH_4}}\right)\right].M_{O_2}.u_{u,O_2}(T_b) + \\ m_{b,N_2}.u_{b,N_2}(T_b) + m_{b,Ar}.u_{b,Ar}(T_b) \end{aligned} \tag{A.13}$$

Writing Eq. A.13 as a function of the masses of the gases before combustion results in Eq. A.15:

$$\begin{aligned} 0 \quad = \quad & \left[u_{u,C_2H_2}(T_u) + \frac{5}{2}\left(\frac{M_{O_2}}{M_{C_2H_2}}\right) u_{b,O_2}(T_b)\right. \\ & \left. -2\left(\frac{M_{CO_2}}{M_{C_2H_2}}\right) u_{b,CO_2}(T_b) - \left(\frac{M_{H_2O}}{M_{C_2H_2}}\right) u_{b,H_2O}(T_b)\right] m_{u,C_2H_2} \\ & + \left[u_{u,H_2}(T_u) + \frac{1}{2}.\left(\frac{M_{O_2}}{M_{H_2}}\right) u_{b,O_2}(T_b) - \left(\frac{M_{H_2O}}{M_{H_2}}\right) u_{b,H_2O}(T_b)\right] \\ & \cdot m_{u,H_2} + \left[u_{u,O_2}(T_u) - u_{u,O_2}(T_b)\right] m_{u,O_2} \\ & + \left[u_{u,N_2}(T_u) - u_{u,N_2}(T_b)\right] m_{u,N_2} + \left[u_{u,Ar}(T_u) - u_{u,Ar}(T_b)\right] m_{u,Ar} \end{aligned} \tag{A.14}$$

Temperature T_b is the peak temperature and is unknown in this equation. Limiting this temperature and correlating this with the temperature at the start of injection allows us to define an extra equation by introducing a factor f defined as

$$T_{SOI} = T_u + f\,(T_b - T_u) \tag{A.15}$$

with $f = 1$: injection at the peak temperature; $f = 0$: injection after complete cooling down. In order to avoid the influence from the pre-combustion on the injection, a heterogeneous temperature and a strong flow field, T_{SOI} should be at least 60% of the peak temperature, which corresponds to a factor f of ∼0.41. The f-factor is taken as small as possible, paying attention that the maximum combustion pressure is not exceeded. For a bursting disk with a bursting pressure of 160 bar (+/-10 bar), an f-factor of 0.37 (maximum theoretical pressure of 145bar) is a good compromise. For high f-factors, the amount of fuel decreases and the mixture was found to be difficult to ignite.

Equation 5: expression for heat capacity

The heat capacity of the mixture at start of injection should be equal to the desired one. The heat capacity of a mixture is the sum of the weighted heat capacities of the single gas components. In this calculation the mass weighted heat capacity is used.

$$\begin{aligned} m_{b,tot}.c_{p,mix}\left(T_{SOI}\right) &= m_{b,CO_2}.c_{p,CO_2}\left(T_{SOI}\right) + m_{b,H_2O}.c_{p,H_2O}\left(T_{SOI}\right) \\ &\quad + m_{b,O_2}.c_{p,O_2}.T_{SOI} + m_{b,N_2}.c_{p,N_2}.T_{SOI} \\ &\quad + m_{b,Ar}.c_{p,Ar}T_{SOI} \\ &= M_{CO_2}\left[2\frac{m_{u,C_2H_2}}{M_{C_2H_2}}\right]c_{p,CO_2}(T_{SOI}) \\ &\quad + M_{H_2O}\left[\frac{m_{u,C_2H_2}}{M_{C_2H_2}} + \frac{m_{u,H_2}}{M_{H_2}}\right]c_{p,H_2O}(T_{SOI}) \\ &\quad + M_{O_2}\left[\frac{m_{u,O_2}}{M_{O_2}} - \frac{5}{2}\frac{m_{u,C_2H_2}}{M_{C_2H_2}} - \frac{1}{2}\frac{m_{u,H_2}}{M_{H_2}}\right] \\ &\quad \cdot c_{p,O_2}(T_{SOI}) \\ &\quad + m_{u,N_2}.c_{p,N_2}(T_{SOI}) + m_{u,Ar}.c_{p,Ar}(T_{SOI}) \end{aligned} \tag{A.16}$$

Writing A.16 as a function of the masses of the gases before combustion results in A.17.

$$\begin{aligned} 0 = &\left[\frac{1}{M_{C_2H_2}}[2.M_{CO_2}.c_{p,CO_2}(T_{SOI}) + M_{H_2O}.c_{p,H_2O}(T_{SOI}) - \right. \\ &\left. \frac{5}{2}.M_{O_2}.c_{p,O_2}(T_{SOI})] - c_{p,mix}(T_{SOI})\right] m_{u,C_2H_2} \\ &+ \left[\frac{1}{M_{H_2}}[M_{H_2O}.c_{p,H_2O}(T_{SOI}) - \frac{1}{2}.M_{O_2}.c_{p,O_2}(T_{SOI})]\right. \\ &\left. - c_{p,mix}(T_{SOI})\right] m_{u,H_2} \\ &+ \left[c_{p,O_2}\left(T_{SOI}\right) - c_{p,mix}\left(T_{SOI}\right)\right] m_{u,O_2} \\ &+ \left[c_{p,N_2}\left(T_{SOI}\right) - c_{p,mix}\left(T_{SOI}\right)\right] m_{u,N_2} \\ &+ \left[c_{p,Ar}\left(T_{SOI}\right) - c_{p,mix}\left(T_{SOI}\right)\right] m_{u,Ar} \end{aligned} \tag{A.17}$$

A.3 Implementation details

A.3.1 Matrix notation

These equations are solved in Octave and the matrix for the set of A.8 - A.17 is of the form

$$[A] \,.\, [x] = [B] \tag{A.18}$$

with

$$
\begin{aligned}
A(1,1) =& a.\frac{M_{H_2}}{M_{C_2H_2}} & A(2,1) =& 1\\
A(1,2) =& -1 & A(2,2) =& 1\\
A(1,3) =& 0 & A(2,3) =& 1\\
A(1,4) =& 0 & A(2,4) =& 1\\
A(1,5) =& 0 & A(2,5) =& 1\\
A(3,1) =& \frac{1}{M_{C_2H_2}}\left[\frac{5}{2}+\frac{1}{2}X_{b,O_2}\right] & A(3,4) =& \frac{1}{M_{N_2}}X_{b,O_2}\\
A(3,2) =& \frac{1}{M_{H_2}}\left[\frac{1}{2}+\frac{1}{2}.X_{b,O_2}\right] & A(3,5) =& \frac{1}{M_{Ar}}X_{b,O_2}\\
A(3,3) =& \frac{1}{M_{O_2}}\left[vol\%_{b,O_2-1}\right] & & \\
A(4,1) =& u_{C_2H_2}(T_u)+\frac{5}{2}\frac{M_{O_2}}{M_{C_2H_2}}u_{O_2}(T_b) & A(4,4) =& u_{N_2}(T_u)\\
& -2\frac{M_{CO_2}}{M_{C_2H_2}}u_{CO_2}(T_b)-\frac{M_{H_2O}}{M_{C_2H_2}}u_{H_2O}(T_b) & & -u_{N_2}(T_b)\\
A(4,2) =& u_{H_2}(T_u)+\frac{1}{2}\frac{M_{O_2}}{M_{H_2}}u_{O_2}(T_b) & A(4,5) =& u_{Ar}(T_u)\\
& -\frac{M_{H_2O}}{M_{H_2}}u_{H_2O}(T_b) & & -u_{Ar}(T_b)\\
A(4,3) =& u_{O_2}(T_u)-u_{O_2}(T_b) & &
\end{aligned}
$$

$$
\begin{aligned}
A(5,1) =& \left[\frac{1}{M_{C_2H_2}}[2.M_{CO_2}.c_{p,CO_2}(T_{SOI})+M_{H_2O}.c_{p,H_2O}(T_{SOI})\right.\\
& \left.-\frac{5}{2}.M_{O_2}.c_{p,O_2}(T_{SOI})]-c_{p,mix}(T_{SOI})\right]\\
A(5,2) =& \left[\frac{1}{M_{H_2}}[M_{H_2O}.c_{p,H_2O}(T_{SOI})\right.\\
& \left.-\frac{1}{2}.M_{O_2}.c_{p,O_2}(T_{SOI})]-c_{p,mix}(T_{SOI})\right]\\
A(5,3) =& c_{p,O_2}(T_{SOI})-c_{p_{mix}}(T_{SOI})\\
A(5,4) =& c_{p,N_2}(T_{SOI})-c_{p_{mix}}(T_{SOI})\\
A(5,5) =& c_{p,Ar}(T_{SOI})-c_{p_{mix}}(T_{SOI})
\end{aligned}
\tag{A.19}
$$

$$x = \begin{bmatrix} m_{u,C_2H_2} \\ m_{u,H_2} \\ m_{u,O_2} \\ m_{u,N_2} \\ m_{u,Ar} \end{bmatrix} \qquad B = \begin{bmatrix} 0 \\ \rho_{inj} V_{chamber} \\ 0 \\ 0 \\ 0 \end{bmatrix} \tag{A.20}$$

A.3.2 Conversion to partial pressure

The partial pressure p_i for each filling gas i is calculated with the ideal gas law with compressibility $Z = 1$:

$$p_i = \frac{m_i}{M_i} \frac{\overline{R} T_u}{V_{chamber}} \tag{A.21}$$

A.3.3 Adiabatic peak pressure

In order to know the maximum combustion pressure the adiabatic flame temperature from the ideal mixture is calculated by assuming complete combustion and no dissociation of the products. The ideal gas law is then used to calculate the pressure. The adiabatic flame temperature is defined as the end temperature of the products of the combustion when heat transfer is neglected. This is clearly an overestimation of the flame temperature and thus peak pressure.

A.4 Filling procedure

A.4.1 Filling equipment

The filling equipment exists of a gas manifold that is connected by a high pressure, high temperature valve to the combustion chamber. This valve is closed during the experiment and has to withstand a combustion pressure of around 150 bar and be tolerant to high gas temperature as well. Furthermore material compatibility had to be checked rigorously: combustion gases from some experiments corroded the original valve heavily, see Figure A.1a. This was attributed to the condensation of water and nitric-oxides in the valve, recombining into nitric acid. The original valve was nickel coated to protect it, but nickel is easily stripped by nitric acid. After the coating was removed by the acid the bare steel of the valve corroded very quickly, eventually jamming the piston.

By replacing this valve with a SAE 316L stainless steel valve the corrosion problem was solved. This valve required compressed air actuation, which

(a) Corrosion in the original valve which was attributed to nitric acid.

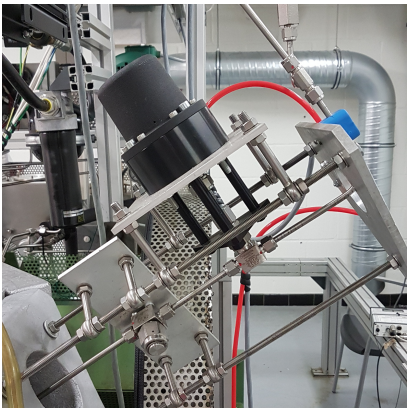

(b) New stainless steel valve mounted on the test bench.

Figure A.1: Old and new valves compared

was added as well. The new valve is shown in Figure A.1b, the actual valve is the small block that connects the stainless steel tubes and the black block on top is the pneumatic actuator. In the Figure, another important component is shown on the bottom left: the gas filter. A metallic sintered filter element with pore size of 15 µm is used to prevent particles entering the filling system. This filter element needs to be replaced after approximately ten measurements and can be re-used after ultrasonic cleaning.

On the gas manifold gas bottles with the filling gases are connected with several proportional valves, shown in Figure A.2 just above the yellow rectangle. The gas pressures are regulated slightly above the calculated gas pressure setpoints by the bottle regulators. The proportional valves are then used to slow the flow rate down to achieve the gas partial pressures as closely as possible. The proportional valves are regulated by an adjustable electrical current and their flow coefficients change proportional to the electrical current. An exhaust valve and a vacuum valve with its vacuum pump are also connected to the manifold.

An additional high pressure valve connected to the compressed air system is mounted on the bottom of the chamber to flush it after an experiment. Compressed air can flow through this valve into the chamber and exit through the manifold and the exhaust valve connected onto the manifold.

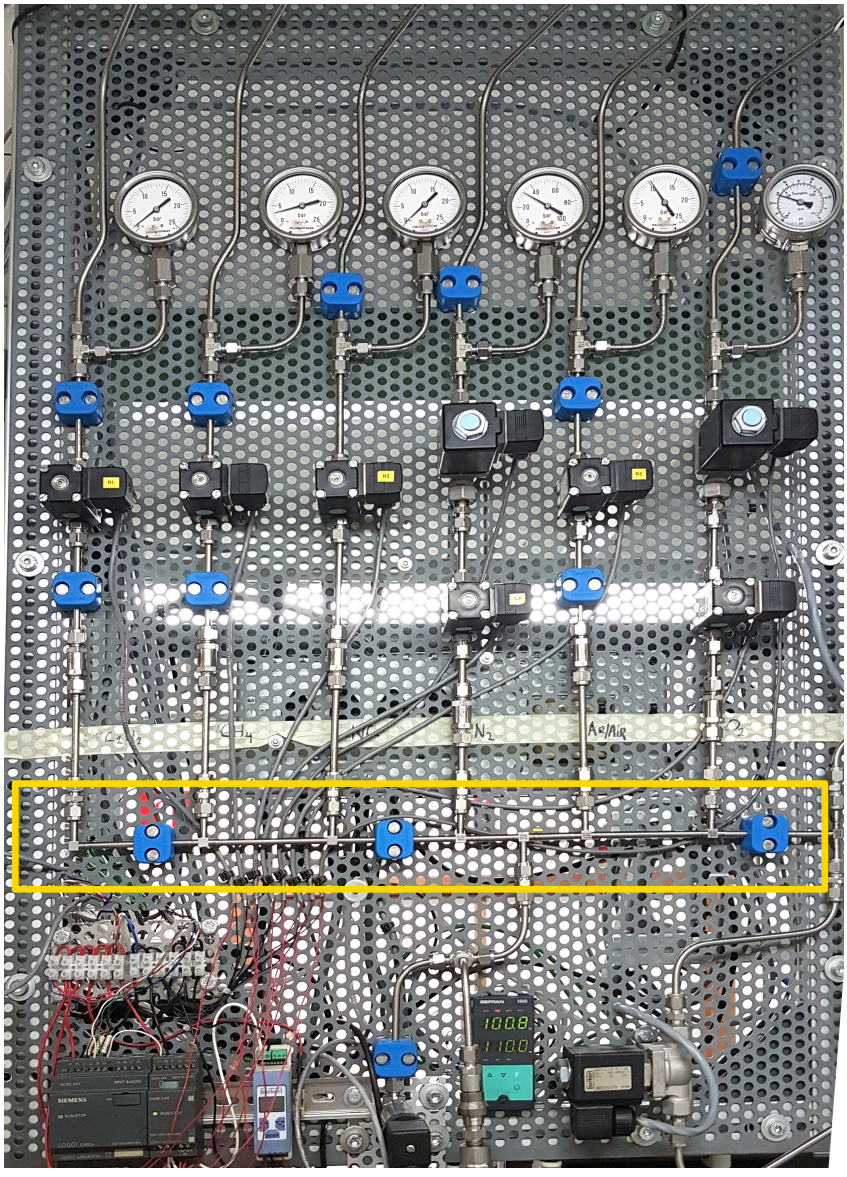

Figure A.2: Gas manifold in yellow rectangle. On the bottom it is connected to the chamber. On the top the proportional valves are visible.

A.4.2 Filling program

The filling process happens sequentially in the following phases:

1. Flush chamber
2. Vacuum chamber
3. Repeat until all gases are filled
   (a) Fill gas nr x
   (b) Vacuum manifold
   (c) Select next gas

In the past the 'Fill gas nr x' step was done by a PID-controller. A setpoint was given and the chamber pressure was used as feedback. The output was adjusted with the error and PID gains. This PID approach was not accurate because the same PID-controller was used for the different gases and it could only contain one set of PID gains. With the proportional valves, the flow coefficients can be adjusted by the PID controller output but this means that filling speed or the flow rate depends not only on the flow coefficient, but also on the bottle pressure. Two different gases with a different bottle pressure could thus result in a different flow rate. Essentially this meant that low pressure setpoints could be filled well but that high pressure setpoints were then problematic due to these identical PID gains and vice-versa.

A new, more flexible filling controller was implemented directly in the controller software of the setup: NI Labview. An overview is shown in Figure A.3. This new controller has a set of calibration constants that are specific for every gas and these constants are automatically tuned during the first part of the filling process. The operator can give a target filling speed, e.g.: 1 mbar/iteration and the controller interpolates linearly from the previous iterations to obtain this filling speed. During the final part of the filling process, the target filling speed is reduced automatically which slows down filling, but improves accuracy as more time is available to stop the filling process.

A.5 Ignition problems

Ignition problems can be caused by number of factors of which the most important were found as spark plug cleanliness, fuel properties such as ignition energy and lower explosion limit and the oxygen concentration.

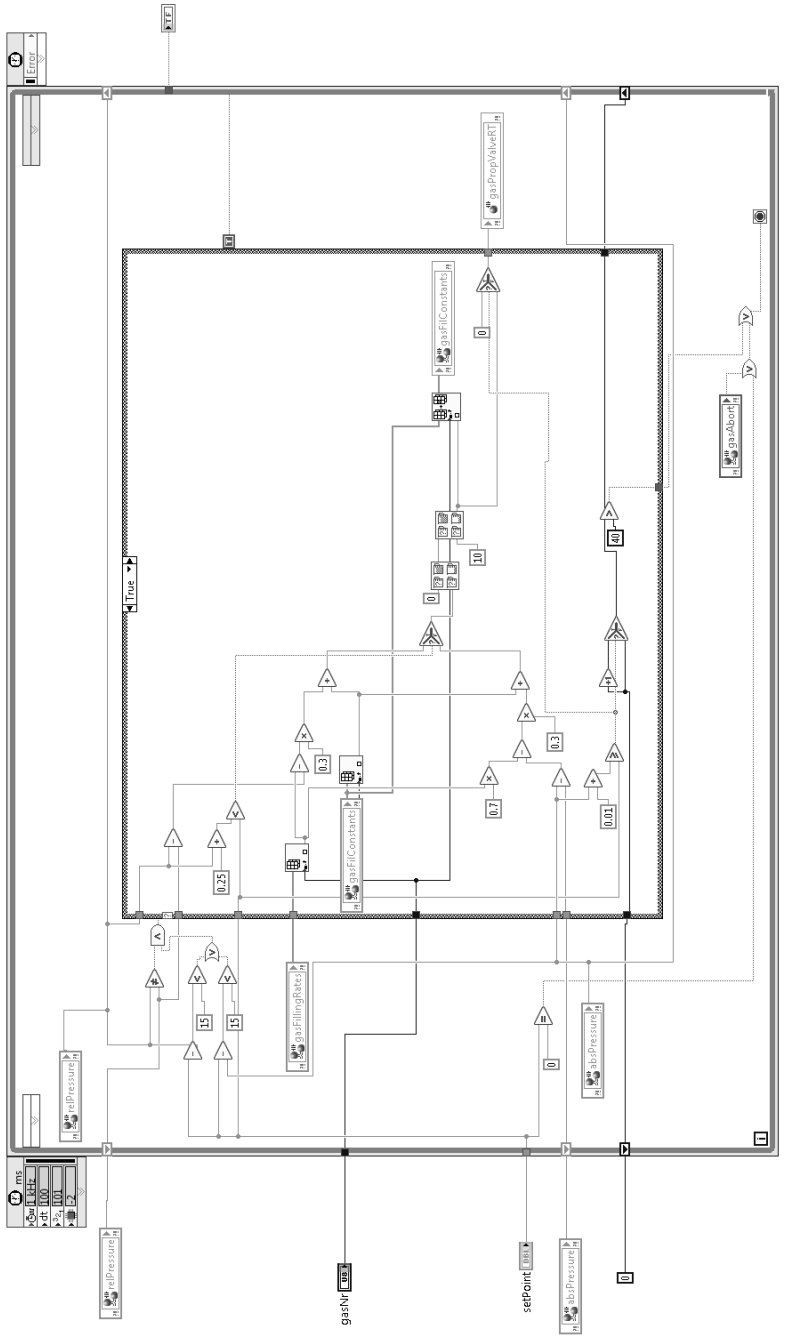

Figure A.3: Overview of the labview filling code.

Because of fuel deposits that originate from the fuel injection during the experiment, the spark plug gets fouled after a certain amount of experiments. The only solution is to stop the experiments and replace the spark plug. After cleaning the dirty spark plugs with an ultrasonic cleaning bath they can be used again in further experiments.

When less and less fuel is mixed in air, it has a typical concentration where it becomes impossible to ignite the mixture: the LEL. No matter how high the ignition energy becomes, the mixture will not burn anymore. On the other hand, there is also a Upper Explosion Limit (UEL) limit which is reached when more and more fuel is mixed in air. This limit is specific for every fuel. Hydrogen has a very wide ignition range (4 %-75 $\%_{vol}$) and acetylene as well (3 %-80 $\%_{vol}$). Mainly the LEL is important in these experiments as the fuel concentrations are always very low. Both acetylene and hydrogen have a very low ignition energy. This is a different fuel property: the amount of energy which must be provided to start the combustion. Experiments with methane were tried because it is very knock resistant, but it proved to be too hard to ignite with its ten-times higher minimum ignition energy and limited ignition range (5 %-15 $\%_{vol}$).

The final property that influences the ignition of the mixture is the oxygen concentration. When decreasing the oxygen concentration, the LOC is defined as the oxygen concentration at which ignition is not possible anymore. Both LEL and UEL are specified in air with 21 $\%_{vol}$ oxygen. This is shown on an ignition diagram in Figure A.4 with the black 'air line' for methane. It shows the ignition region of methane when it is mixed with oxygen and nitrogen. The fraction of methane, oxygen and nitrogen are shown on the edges of the triangle and the air line with 21 % oxygen is shown separately. The line crosses the (shaded) flammable region in the LEL and UEL. When oxygen concentration decreases in the mixture, such as in our conditions, the mixture line moves to the right hand side and it is clear that the flammability range decreases. Now the LOC is more clearly defined as the point where the LEL and UEL become the same on the mixture line. At this oxygen concentration, fuel concentration needs to be higher than the LEL to obtain a flammable mixture.

In this work a mixture of hydrogen and acetylene was used as a fuel because of their low ignition energy and low LOC. Acetylene is very unstable and decomposes violently even without oxygen when subject to shocks, which means it is impossible to define a LOC. In the combustion chamber, this decomposition is highly unwanted. To calculate a mixture LOC the limit for acetylene was artificially set to the LOC for ethylene.

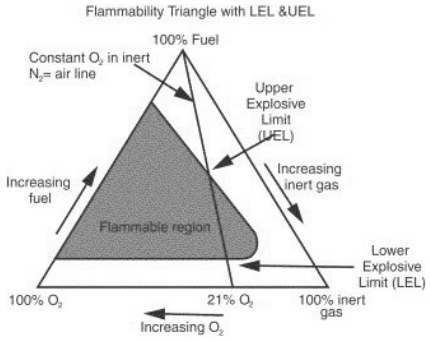

Figure A.4: Ternary diagram showing the flammable region from [102].

The mixture LOC and LEL were then calculated by Le Chatelier mixing:

$$\begin{aligned} LOC_{mix} &= \frac{n_{C_2H_2} + n_{H_2}}{\frac{n_{C_2H_2}}{0.085} + \frac{n_{H_2}}{0.05}} \\ LEL_{mix} &= \frac{n_{C_2H_2} + n_{H_2}}{\frac{n_{C_2H_2}}{0.03} + \frac{n_{H_2}}{0.04}} \end{aligned} \tag{A.22}$$

where n_x is the amount of moles of 'x' in the mixture.

Ignition problems can now be avoided when oxygen and total fuel concentration are slightly larger than LOC_{mix} and LEL_{mix}.

A.6 Target condition and resulting partial pressures

The calculation is done for a range of boundary conditions: gas density and temperature are varied to represent different engine loads. Then, the EGR fraction can be varied by varying the oxygen concentration. These conditions are shown on the left hand side of Table A.1, the resulting gas partial pressures are indicated in the middle and the checks for adiabatic peak pressure, target cool-down time, LEL and LOC are shown on the right hand side. The actual concentration of oxygen is given, next to the limiting oxygen concentration to evaluate if the mixture can react. The LEL is checked in the same way.

Table A.1: Target conditions, calculated target pressures, LEL and LOC

T_{SOI}	O_2	ρ	C_2H_2	H_2	Ar	N_2	O_2	p_{adia}	T_{delay}	X_{fuel}, LEL	X_{O_2}, LOC	D_{mix}
[K]	[-]	kg/m^3	[bar]	[bar]	[bar]	[bar]	[bar]	[bar]	[bar]@[s]	[-,-]	[-,-]	[-]
Evaporating												
850	0	22.8	0.76	0.77	2.04	19.31	2.24	113	54.1@2.5	0.06; 0.034	0.09; 0.063	9.56
1000	0	15.2	0.47	0.52	2.68	11.36	1.42	73	41.7@1.56	0.06; 0.035	0.087; 0.062	10.33
850	0	15.2	0.51	0.52	1.38	13.05	1.52	76	36.6@1.95	0.061; 0.034	0.09; 0.063	9.56
700	0	15.2	0.47	0.52	1.3	13.31	1.43	73	30.2@2.83	0.058; 0.035	0.084; 0.062	10.28
850	0	7.6	0.29	0.26	1.08	5.84	0.85	41	17.9@1.55	0.0656; 0.034	0.102; 0.064	8.62
Reacting												
750	0.13	15.2	0.41	0.51	1.82	10.41	3.37	67	31.5@2.2	0.056; 0.035	0.20; 0.061	11.47
850	0.13	15.2	0.43	0.51	1.1	11.32	3.46	67	36.3@1.76	0.056; 0.035	0.21; 0.062	11.07
750	0.19	15.2	0.38	0.51	1.69	9.64	4.24	76	31.3@2.2	0.054; 0.035	0.26; 0.061	12.37
750	0.21	15.2	0.36	0.51	1.64	9.43	4.50	76	31.3@2.2	0.053; 0.035	0.27; 0.060	12.96

B

Engine Simulation Code

In this appendix, a description of the used 1D engine model will be given and the set-up and calibration procedure will be explained. In an internal combustion engine two flow domains can be distinguished: mainly one-dimensional flow and strong three-dimensional flow. Flow through pipes such as the intake, exhaust and intercooler is considered here to be one-dimensional and 1-D continuity equations are solved in these parts to increase computational speed. Some flow parts such as the compressor and turbine are difficult to model with this approach and to maintain computational speed, performance maps for these parts are used instead. The combination of one-dimensional flow and performance maps is called the gas-dynamics simulation.

The flow in the cylinder is strongly three-dimensional and is modeled separately with a dedicated set of sub-models: heat transfer, combustion and turbulence. To completely separate the combustion from the gas dynamics during calibration of the latter, the combustion rate is measured during preliminary experiments for every operating point. This combustion rate is measured indirectly with a technique called TPA which is explained further in this chapter. The combustion model is then replaced by this perfect, measured combustion rate and is assumed to remain constant during gas dynamics calibration. These simulations were carried out using a commercial code: 'GT-Suite' [29].

B.1 Gas dynamics simulation

The model is built from general flow components such as pipes and bends. These components are discretized into smaller control volumes to solve the continuity equations along the stream lines. Parts with a complex three-dimensional flow, such as compressors and turbines, are measured at the manufacturer and performance maps are used to model these components instead.

To calibrate this model, the engine is measured at several load points: during the measurement campaign a 100%, 75%, 50% and 25% engine loads were measured, once at nominal speed and once at decreasing engine (propeller law) speed. Propeller speed is defined as the speed required for a propeller with constant pitch to draw a certain amount of engine power. These speeds are defined in the 'E3' test-cycle from ISO 8178 as 100%, 91%, 80% and 63% of nominal engine speed. These operating points are also used to obtain cycle values for fuel consumption and emissions of the engine.

Several engine variables are measured, including:

- Crankangle resolved values (high sampling rate, e.g. $[40kHz]$)
  - $p_{cylinder}$
  - p_{intake}
  - $p_{exhaust}$
- Averaged values (low sampling rate, e.g. $[10Hz]$)
  - Power
  - Fuel consumption, air mass flow
  - $T_{turb,in}, T_{turb,out}, T_{comp,in}, T_{comp,out}$
  - $p_{turb,in}, p_{turb,out}, p_{comp,in}, p_{comp,out}$
  - Emission components

The calibration procedure consists of small adjustments of model parameters which can be justified by tolerances of components (e.g., valve lash measured with a cold engine decreases when the engine heats up). Large adjustments are not acceptable, because then the model loses its predictive capability on new operating conditions.

To check the accuracy of the model it was compared to measurements for several parameters:

- Air mass flow

- Fuel consumption
- Temperatures and pressures at several components
- Turbo speeds

Calibration factors include multipliers for compressor and turbine efficiency and mass flow rate; this is justified within certain limits as the maps for the turbocharger were measured on a constant flow test bench and the flow on the engine is highly pulsating. Other calibration factors are valve timing and lash due to tolerances, friction model parameters, heat transfer model and so on. During simulation of new cases all calibration values were left unchanged, and it was assumed that these calibrated models would behave the same under slightly different operating conditions.

B.2 Three pressure analysis

While calibrating the gas dynamics of the model, the combustion rate is fixed. The imposed combustion rate is determined first by a technique called TPA.

TPA is a technique that uses the cylinder, inlet and exhaust measured pressure profiles to obtain the heat release rate and the gas composition in the cylinder during combustion that best reproduces the measured cylinder pressure. The inlet and exhaust pressures are combined with the flow losses over the valves and ports together with the inlet temperature measurement to obtain the trapped mass in the cylinder when the valves close. Then, the combustion rate that would be required to obtain the cylinder pressure at each time step is calculated. The result is an ideal, measured heat release rate for all operating points.

Detailed explanations about possible processing errors are given in the manual [29]:

- Cylinder pressure offset
- Air mass flow deviations
- Lower heating value multiplier

Standard problems will not be discussed here, but some results have to be closely examined: e.g. the offset of the measured cylinder pressure. The cylinder pressure sensor is a piezoelectric sensor that can only measure pressure increase or decrease, relative to its initial value. This means

that it needs to be referenced to an absolute pressure before usage. Typically, the inlet and exhaust absolute pressure signals are used as a reference when the respective valve is open, by assuming no pressure loss over the valve when it is opened. This proved to be impossible on this engine because it is turbocharged and the pressure loss over the valve was always significant. In the end, the pressure reference was done by the compression pegging method described in [103] and used in [24]. In internal combustion engines, the process in the early compression stroke can be assumed to be polytropic. The absolute pressure-volume relation is given by:

$$\log p_{abs} = \gamma \cdot \log V \tag{B.1}$$

where $p_{abs} = p_{measured} + p_{offset}$ and γ is unknown and depends on the heat transfer in the engine. An iterative pegging algorithm was applied to the pressure profiles as follows: two outer bounds for the pressure shift are chosen, Δp_{max} and Δp_{min}. Initially the mean of these pressure shifts is applied as the pressure offset on the measurement data. A second order polynomial regression is fitted on the log(pressure)/log(volume) measurement data:

$$\log p_{measured} + p_{offset} = C_1 \cdot \log V^2 + C_2 \cdot \log V + C_3 \tag{B.2}$$

The sign of C_1 determines whether Δp should be used in the next iteration as the maximum, or the minimum pressure offset. When the pressure offset comes closer to the true necessary pressure offset the equation will take the form of eq. (B.1), C_1 will become zero and C_2 will become the average polytropic exponent.

This proved to be a successful method to reference the cylinder pressure for all but the low load operating points. This was detected as a problem with the TPA peak predicted combustion pressure at low load and was caused by a disturbance in the measurement pressure. At inlet valve closure cylinder pressure oscillates slightly which causes a wrong pressure offset and thus a wrong initial cylinder pressure which is then used during further combustion analysis. During compression, this difference becomes bigger and the resulting end of compression pressure changes very much which results in a failed TPA. This was resolved by manually adjusting the pressure offset for these cases.

B.3 Predictive combustion model

The TPA procedure results in ideal heat release rates which can be used to calibrate the gas dynamics part of the simulation code, but additionally these ideal heat release rates can be employed to calibrate a combustion

model that can predict the heat release rate and the emissions based on the injection characteristics and the combustion chamber conditions.

The DI-Pulse model is the current direct injection combustion model in GT-Power. This model requires accurate injection profiles to achieve meaningful results and these are obtained by a combination of measurements (injection pressure and needle lift) and simulation code (AmeSim): details about this simulation code are described in appendix C. The injection profiles can be entered as injection pressure as a function of time, but also directly as mass flow rate as a function of time. In further engine simulations results from the injector model have been used for the injection rates.

The model is described by GT-Power as follows: cylinder contents are divided over three thermodynamic zones, each with their own temperature and composition: an unburned zone which contains all cylinder mass at inlet valve closure, a spray unburned zone which contains injected fuel and entrained gas and a spray burned zone which contains the combustion products. It contains several submodels to simulate physical processes such as the gas entrainment, evaporation, ignition and finally combustion.

The penetration as a function of time $[t]$ is given as:

$$S = \begin{cases} C_d \left(\dfrac{2\Delta P}{\rho_l}\right)^{0.5} t & t \leq t_b \\ 2.95 \left(\dfrac{2\Delta P}{\rho_a}\right)^{0.25} (d_n t)^{0.5} & t > t_b \end{cases} \tag{B.3}$$

with C_d the discharge coefficient, $\Delta P = P_{inj} - P_{cyl}$, ρ_l the fuel density, ρ_a the ambient density and the breakup time $t_b = 4.351 \dfrac{\rho_l d_n}{C_d^2 (\rho_a \Delta P)^{0.5}}$.

Gas entrainment in a given injection pulse depends on the penetration and speed of that pulse, and these are given by a correlation (eq. (B.4)) from Hiroyasu which has been modified by Jung [104]. This gas entrainment rate is corrected by GT-Power with an entrainment multiplier $[\mathbf{C_{ent}}]$.

$$\frac{dm}{dt} = -\mathbf{C_{ent}} \frac{m_{inj} u_{inj}}{u^2} \frac{du}{dt} \tag{B.4}$$

with $u = \frac{dS}{dt}$.

After the break-up period fuel starts to evaporate and the model describes the liquid fuel into fine droplets with a size equal the Sauter Mean Diameter. These droplets all start to evaporate at a rate that is limited by diffusion of fuel vapor away from the droplet. In [104]

the necessary energy for evaporation of the droplets is provided by convective heat transfer from the gas to the droplets, however in GT-Power this information is unavailable. This strongly disagrees with current assumption of mixing-limited evaporation, where this inter-phase energy transfer is not the rate limiting step section 2.4.2.

Once evaporated fuel is available, the mixture starts to react after a certain ignition delay. Of course, ignition delay is a complicated function of mixture temperature, pressure, equivalence ratio and fuel properties, and these conditions vary greatly in the spray due to compression from the piston and ambient gas entrainment during the ignition delay. The instantaneous ignition delay is given by a simplified Arrhenius expression:

$$\tau_{ign} = \mathbf{C_{ign}} \cdot \rho^{-1.5} \exp \frac{3500}{T} \cdot [O_2]^{0.5} \tag{B.5}$$

as in [105], and an ignition delay multiplier has been added by GT-Power [$\mathbf{C_{ign}}$], together with the oxygen concentration $[O_2]$ and ρ dependence. This expression is then integrated during the ignition delay as follows:

$$\int_{t_0}^{t} \frac{1}{\tau_{ign}} dt \tag{B.6}$$

Once this integral reaches one, the ignition delay time has been reached and reaction starts. After the ignition an air-fuel mixture is present in the unburned zone and this mixture will react during the premixed combustion. The combustion rate is assumed to be kinetically limited and can be tuned by changing the premixed combustion rate multiplier [$\mathbf{C_{pm}}$]. After the premixed combustion, the remaining fuel continues to mix and burns in the diffusion combustion. The rate of this combustion can be modified by the diffusion combustion rate multiplier [$\mathbf{C_{df}}$].

The model is calibrated by searching for the multipliers that result in the lowest sum of errors between the measured, from the TPA, and the predicted heat release rate. The simulation results with the predictive combustion model are reported in Chapter 5.

C

Determination of the Rate of Injection

To start a spray simulation the fuel mass flow rate and velocity at the exit of the nozzle holes during the injection is needed as boundary conditions. First, the simplest flow models, based on Bernoulli's flow rate equation are described and flow coefficients are defined. Then, a more complex, 1D simulation code is proposed to refine results. Possible measurement strategies are explained and because of limitations in our measurement equipment the procedure to define fuel mass flow and velocity from simple line pressure and needle lift measurement is shown. Finally, the effect of cavitation on the injection velocity in a PLN system is explained.

C.1 Nozzle flow models

C.1.1 Bernoulli

The Bernoulli equation can be considered as a conservation of energy principle, applied to flowing liquids. When this principle is applied to flow in the nozzle and by neglecting potential energy due to gravity the equation can be written as:

$$P_{sac} + \frac{1}{2}\rho u_{sac}^2 = P_{chamb} + \frac{1}{2}\rho u_{th}^2 \tag{C.1}$$

where P_{sac} is the pressure in the sac volume, P_{chamb} is the exit pressure and u_{th} the theoretical outlet velocity. The inlet velocity u_{sac} is usually neglected, because this is very small compared to the other terms.

This equation applies to uniform flow over the complete area of the nozzle hole, but the real flow includes cavitation and wall effects and is determined by the velocity and density profiles through the flow area [106]. However, it is possible to simplify the flow to a uniform one with an effective area which is smaller than the geometric one. The effective exit velocity can then be determined by Bernoulli's equation and the velocity coefficient C_v which includes all the flow effects:

$$u_{eff} = C_v \cdot u_{th} = C_v \cdot \sqrt{\frac{2\Delta P}{\rho_f}} \tag{C.2}$$

The velocity coefficient compares the effective velocity to the maximum theoretical velocity by Bernoulli's law which is achieved when all the pressure energy would be converted to kinetic energy without losses. This coefficient captures the flow losses from friction with the wall, and effects of non-uniform flow velocity.

Another flow coefficient is necessary to further define the flow through the nozzle: the area coefficient. When injection pressure is increased more and more, flow separates at the corners of the nozzle hole due to inertia forces and a recirculation zone develops [97]. The presence of this recirculation zone decreases the flow area, causing a velocity increase and pressure decrease. When the pressure drops below the vapor pressure of the liquid, cavitation bubbles occur. This recirculation zone could reattach, depending on the length of the nozzle, the injection pressure and other parameters. The area coefficient describes the relative reduction of the flow area compared to the geometric one due to cavitation inside the nozzle hole:

$$C_a = \frac{A_{eff}}{A_{geom}} \tag{C.3}$$

The discharge coefficient is defined as the ratio of the actual mass flow rate to the theoretical one:

$$C_d = \frac{\dot{m}}{\dot{m}_{th}} = \frac{A_{eff} u_{eff} \rho}{A_{geom} u_{th} \rho} = C_v \cdot C_a \tag{C.4}$$

and can also be written as the product of the area coefficient and the velocity coefficient.

Rewriting allows to calculate the actual mass flow rate from the theoretical one as follows:

$$\dot{m} = C_d \cdot A_{geom} \cdot \sqrt{2 \cdot \rho_l \cdot (P_{inj} - P_{chamb})} \tag{C.5}$$

C.1.2 Nurick

While the theoretical mass flow depends on the pressure drop across the nozzle, the actual mass flow under cavitation conditions does not increase when the pressure difference over the nozzle is raised for a constant injection pressure which means that the nozzle is choked. With some assumptions (summarized in [107]) the one dimensional model of Nurick can be developed:

1. The density of the fluid is constant and there is no mass transfer between the two phases [97]
2. Pressure in the cavitation zone is equal to the vapor pressure [97]
3. Friction with the wall is neglected in presence of vapor bubbles in contact with the wall [97]
4. The contraction coefficient is defined as $C_c = \frac{A_c}{A_{geom}}$ where A_c is the area in the contraction zone [108]

The real mass flow through the contraction area (point c in fig. C.1) can then be written as:

$$\dot{m} = A_{geom} \cdot C_c \cdot \sqrt{2 \cdot \rho_l \cdot (P_{inj} - P_v)} \tag{C.6}$$

Combining eq. (C.6) and eq. (C.5) results in the Nurick [40] model for the discharge coefficient under cavitating conditions:

$$C_d = \frac{A_{geom} \cdot C_c \cdot \sqrt{2 \cdot \rho_l \cdot (P_{inj} - P_v)}}{A_{geom} \cdot \sqrt{2 \cdot \rho_l \cdot (P_{inj} - P_{chamb})}} = C_c \cdot \sqrt{\frac{P_{inj} - P_v}{P_{inj} - P_b}} = C_c \cdot \sqrt{K} \tag{C.7}$$

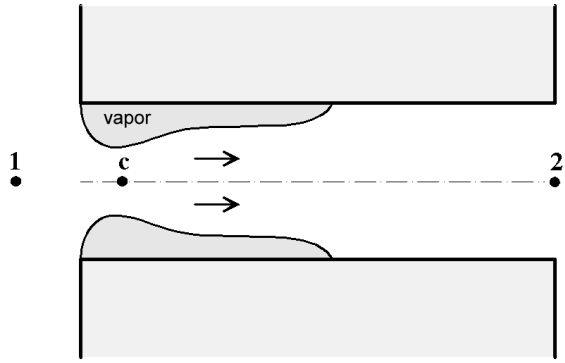

Figure C.1: Schematic view of cavitation in a nozzle hole, taken from [108].

In cavitating conditions the discharge coefficient is thus proportional to $\sqrt{K}$. When the flow in the nozzle is not cavitating, the mass flow depends on the Reynolds number and increases slightly when the discharge pressure is decreased. In fig. C.2 the discharge coefficient is determined by measuring the instantaneous mass flow rate and comparing it to the theoretical one. The discharge coefficient is shown as a function of $\sqrt{K}$: decreasing $\sqrt{K}$ for a constant injection pressure means decreasing the back pressure. The maximum C_d is the critical discharge coefficient and when $K < K_{crit}$ the flow is cavitating and mass flow is limited by injection pressure. When $K > K_{crit}$ the mass flow increases with increasing Reynolds number (e.g. decreasing back pressure).

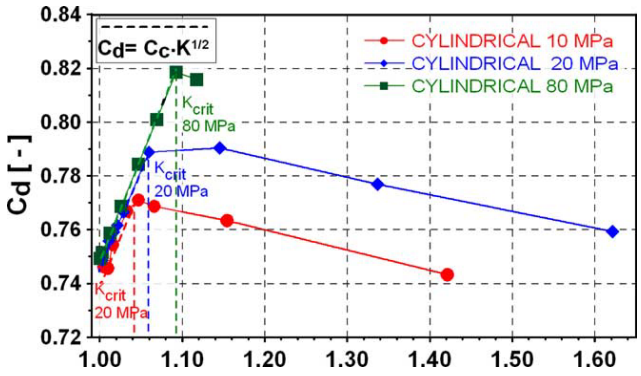

Figure C.2: Discharge coefficient as a function of $\sqrt{K}$ [41].

C.1.3 Cavitation regimes

When cavitation starts, it is known that the mass flow rate stagnates when back pressure is decreased, but it is still unknown why. In [109] cavitation was visualized using high-speed cameras to investigate the effects of cavitation on the liquid jet. Liquid velocity of a water jet in an optical upscaled nozzle was measured using laser doppler velocimetry. Additionally, the cavitation bubbles were visualized as well and based on their measurements the authors were able to distinguish four cavitation regimes and the resulting sprays:

- No cavitation -> Wavy jet
- Developing cavitation -> Wavy jet
- Super cavitation -> Spray
- Hydraulic flip -> Flipping jet

In fig. C.3 the obtained velocity profiles and cavitation images are shown for increasing Reynolds number, in this case equivalent to increasing mean velocity. The first three defined regimes are shown: on the left hand side the no cavitation regime is visible, the velocity is uniform over the complete area and no cavitation bubbles are visible. In the two center images cavitation starts to develop and the velocity in the nozzle hole is not uniform anymore as could be expected from Nurick's model. A recirculation zone develops and when velocity is increased, the reattachment of the zone to the wall happens later. Closer to the hole exit the velocity still approaches the uniform profile quite well. Finally, on the right hand side super cavitation is shown: cavitation extends towards the hole exit and even at the hole exit the velocity is non uniform with a higher velocity at the center than at the edges.

Injection pressure in the nozzle increases quickly, so cavitation is growing shortly after start of injection. The length over diameter ratio of the nozzle hole is typically not very high which increases the likelihood of super cavitation because the recirculation zone does not have much time to reattach. This super cavitation regime is observed in the breakup of the spray exiting the nozzle. The different cavitation regimes and resulting sprays are shown in fig. 2.7. When cavitation bubbles implode directly before the nozzle exit, they provide the necessary energy and turbulence for strong breakup of the liquid fuel, resulting in an atomization of the fuel or spray. This was already observed without the in-depth knowledge of the cavitation phenomenon in [110]: they defined two liquid jet breakup regimes that are directly equivalent to the developing cavitation and super cavitation regime. The onset of these regimes was also found to be

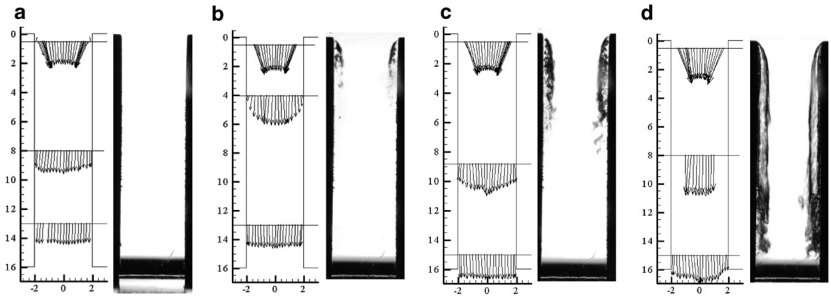

Figure C.3: Distribution of liquid velocity in an optical nozzle for increasing Reynolds number (a) Re = 50000 (b) Re = 58000 (c) Re = 64000 (d) Re = 70000, images show the cavitation zone (adapted from [109]).

dependent on the injection velocity, which is consistent with the latest observations regarding the mean injection velocity such as in fig. C.3.

C.2 Injection flow measurement

To characterize the flow completely, several measurement techniques have been described in literature. By combining these measurement techniques, the respective change in exit velocity and mass flow rate with changing injection and chamber pressures can be captured in the earlier described flow coefficients.

C.2.1 Measurement techniques

Specialized equipment can be used to measure mass flow rate and spray velocity. The mass flow rate can be determined by a Bosch measurement tube [111] or a Zeuch chamber [112]. The Bosch measurement rig exists out of a fuel filled tube and a pressure transducer. Fuel is injected in a predetermined length of tube, and this produces a variable liquid velocity which depends on the injection rate; at the same time a pressure wave is produced in the tube which is measured by the pressure transducer. This provides a measure for the injection rate.

A Zeuch chamber is a chamber which is filled completely with fuel at an initial pressure. Fuel is injected into this chamber and the chamber pressure is recorded. The injection rate is then calculated from the bulk modulus of the fuel and the pressure increase. The last technique was tried in the *GUCCI* setup but after thorough flushing there was still too much air in the chamber sealings which resulted in an air-fuel mixture with an unknown bulk modulus and made the measurement unreliable.

The injection speed can be determined directly from the mass flow rate measurement:

$$u_{eff} = \frac{\dot{m}}{\rho_l A} \tag{C.8}$$

by assuming a uniform exit velocity over the complete hole area. This assumption basically sets the area flow coefficient C_A to one and attributes all losses to the velocity coefficient C_v. However, the uniform velocity is a rather crude assumption when considering the previous results about cavitation and its effect on velocity distribution in the nozzle hole.

Another technique to determine the injection velocity was developed [108, 113, 114]: it is measured indirectly with a combination of the momentum flux and mass flow measurement. The momentum flux can be measured by a different setup: the impact force of a spray is measured by a piezoelectric force sensor which is placed close to the nozzle hole such that the frontal area of the sensor catches all the spray's momentum. Due to conservation of momentum the measured force is then equivalent to the momentum flux. The effective injection velocity can then be determined by combining with the mass flow rate:

$$u_{eff} = \frac{\dot{M}_f}{\dot{m}_f} \tag{C.9}$$

C.2.2 Determination of the flow coefficients

The effective outlet velocity that results from the momentum flux measurements was found to be higher than the one calculated by the uniform exit velocity assumption in [113]. This can be explained by a decreasing effective flow area that is caused by increasing cavitation. Two different nozzles were measured using the momentum flux methodology in [113]: a convergent and a cylindrical nozzle. The flow coefficients C_A, C_v and C_d were calculated from the measurements and are reproduced in fig. C.4 as a function of the cavitation number. On the right hand side, the convergent nozzle is shown. This nozzle does not show cavitation behavior because of its geometry: the inlet section has a larger diameter than the outlet section which suppresses the recirculation zone. On the left hand side the results for the cylindrical nozzle are shown, this nozzle shows cavitation when $K < K_{crit}$. When decreasing chamber pressure even more the C_d coefficient decreases, as expected from Nurick's model, but equally important: the C_A coefficient starts to decrease as well.

Because the vapor from the super cavitation separates the nozzle's wall and liquid the friction is reduced and as a result of this the wall shear could be expected to be near zero [97]. Using conservation of momentum

on a control volume from the cavitation area to the exit of the nozzle hole the effective velocity can then be computed with a smaller effective section A_{eff} as:

$$u_{eff} = \frac{2C_c P_{inj} - P_{chamb} + (1 - 2C_c)P_v}{C_c\sqrt{2\rho_f(P_{inj} - P_v)}} \tag{C.10}$$

This results in an area coefficient of:

$$C_A = \frac{A_{eff}}{A_{geom}} = \frac{2C_c^2(P_{inj} - P_v)}{2C_c P_{inj} - P_{chamb} + (1 - 2C_c)P_v} \tag{C.11}$$

Compared to the uniform exit velocity assumption, this zero wall shear assumption will produce the highest possible velocity for the given injection conditions. Based on the observations from momentum measurements and optical studies of cavitating flow in nozzles this method proves to be the best possible option when cavitation is present.

C.3 Amesim

C.3.1 Motivation

Both the mass flow rate and momentum measurement require new or updated test benches as described above which are currently not available in the lab. However, in the current setup needle lift and injection pressure in the high pressure line are measured. The pressure measurement is certainly not equal to the pressure in the injector because there are flow losses from the measurement location to the sac volume of the injector. By combining these limited measurements with a simulation model better boundary conditions can be achieved for the mass flow rate.

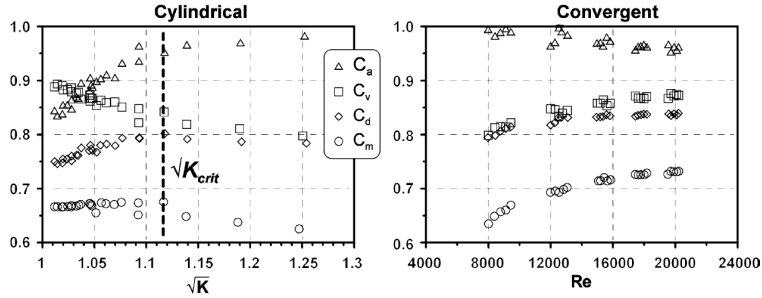

Figure C.4: Flow coefficients C_A, C_v and C_d, taken from [113].

Furthermore, the time frame of one injection is very short and pressure wave propagation from the pump to the injector and vice-versa will cause a pressure wave delay from the measurement location to the injector. To capture these effects a hydraulic simulation model is built with Simcenter Amesim software: this software package provides libraries that contain basic physical components, such as pistons, springs, pipes, etc. By means of these components different systems of varying complexity, e.g. a PLN injection system, can be built. After the system is assembled each component needs a submodel (an implementation of the underlying physics) and in the final step the parameters of the submodels are determined.

C.3.2 Model description

The hydraulic simulation model of the high pressure fuel circuit was first designed and validated by groups of master thesis students: Nathan De Kerpel and Korneel Vermeyen [115] and expanded by Alexander-Jan De Santis and Thibo Moerman [116], supervised by the author of this work. The general lay-out of the developed model is shown in fig. C.5: the pump is shown on the left and is driven by a camshaft. The pump outlet is connected to the delivery valve and a high pressure line then connects to the injector on the left.

In fig. C.6 a detailed view on the injector model is shown. The injector exists out of a sac type nozzle with a spring loaded needle that closes off the nozzle holes. Several channels connect the high pressure line to a chamber under the needle. The pressure increase under the needle will then lift the needle and open the sac volume to the fuel pressure. Here the model types are clearly visible: flow models are shown in blue and force models are shown in brown. On the left side the flow losses are modeled with hydraulic tubes, and on the right side the force balance is calculated: the needle is spring loaded on top, generating a closing force, and sac pressure pushes onto the needle area on the bottom, generating a lifting force. The needle is modeled by several pistons with variable diameters, as was measured on the needle, that are connected to the high pressure line through the hydraulic tubes on the left. Finally, the nozzle hole configuration is shown in the bottom: only one nozzle hole is visible as the simulation allows configuration for multiple holes in the submodel. The submodel for the flow through the nozzle takes a flow coefficient, but this is the C_d coefficient. The fuel's exit velocity is estimated by assuming a uniform velocity profile, which is not justified in a cavitating nozzle. The submodels that were available did not include any cavitation parameters, so manual correction based on the mass flow rate and pressure in the sac volume will be necessary.

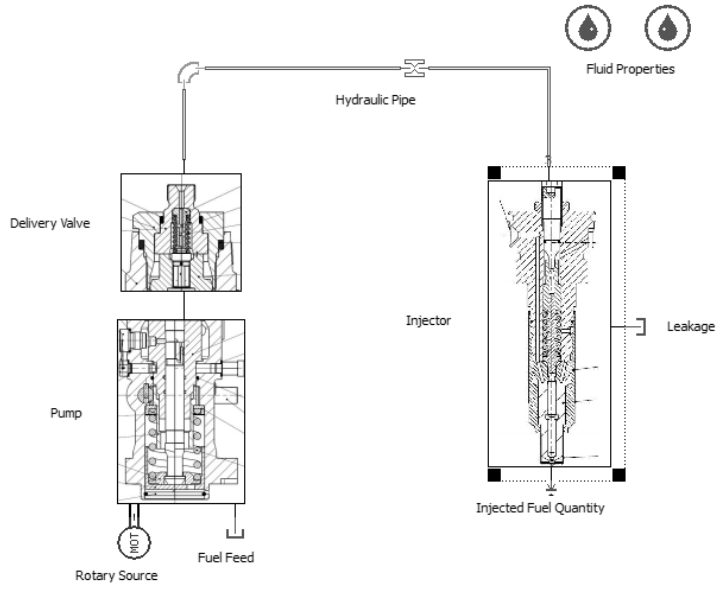

Figure C.5: Overview of the Amesim simulation model: adapted from [116].

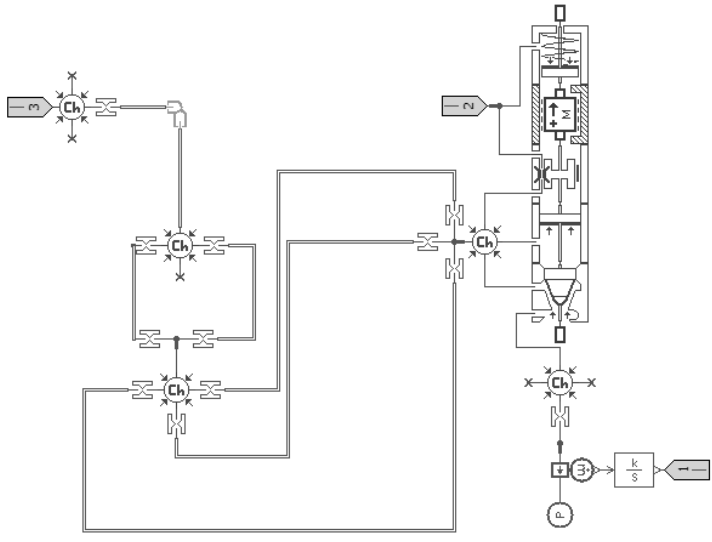

Figure C.6: A detailed view on the injector model: adapted from [116].

C.3.3 Matching the Amesim flow model to measurements

The model of [116] was developed for a dual fuel injection system and in this work a larger pump is used together with different nozzles which means that several adjustments needed to be done. In these paragraphs the main adjustments are discussed, but these should be read alongside the initial documentation of De Santis and Moerman.

Geometrical parameters were measured from the injection pump and nozzles and updated in the simulation code: the helix profile from the injection pump was scanned by rolling it on a piece of paper, the inlet and outlet diameters of the chamber were updated and the diameter of the piston was updated as well. The nozzle was replaced by an eight-hole nozzle and the dimensions of the needle were measured and updated as this affects the lifting speed and acceleration of the needle. The diameter of the nozzle hole was taken from the manufacturer and the flow coefficient was used as a calibration parameter. Other improvements were still needed:

- In the pump, the volume of the chamber needed to be decreased: the piston part already includes its volume, no there is no need to add an additional volume on top of it. Now, the volume correctly represents the clearance volume at top dead center of the pump.

- The flow areas of the pump were adjusted: in our experiments we used a 20mm diameter pump, and the helix profile was different as well. The areas and hydraulic diameter of the intake, spill port and helix were recalculated for the new dimensions.

- A lower flow coefficient in the helix port was tested, but only minimally decreases the pressure decrease rate.

- In the delivery valve additional flow losses were introduced to better reflect reality. When fluid enters the delivery valve it first has to pass four small orifices to get to the first flow component of the simulation part. Now, these orifices are included in the simulation. The effect of this improvement is rather limited, because the pressure in the line is determined upstream, at the injector side. If more losses are introduced at the pump side, the pump pressure is simply going up. While the simulation is more accurate now, the net effect on the measured pressure during compression is zero. When the flow reverses, e.g. during the pressure decrease a slight influence is seen, motivating to keep the change.

- In the injector, the volumes of the chambers between different flow lines are reduced to reflect reality better. The needle diameter is adjusted for a new nozzle with 10 holes and 0.38mm diameter.
- The spring in the injector was adjusted both for the pre-compression force and the spring stiffness. The pre-compression force changes for every nozzle because the length of the needle changes slightly between nozzles. This means with the rest of the configuration being equal, that the spring compression at zero needle lift changes when a different nozzle is mounted. The spring stiffness was changed because this was the only parameter that would bring down the simulated opening pressure to the measured level. This only influences the start of injection, and has a negligible effect on the pressure in the sac volume during the rest of the injection.
- Finally, the fuel properties were adjusted. The model was calibrated with diesel nr2 properties, but during the last measurements n-dodecane was injected which has a different viscosity, density and bulk modulus. Properties from [117] and [118] were used.

The final validation of the Amesim model is shown in fig. C.7: needle lift and pressure at the measurement location are compared between the measurement and the simulation, on the left hand side results for the ten hole nozzle are shown and on the right hand side the eight hole nozzle. Note that the needle lift for the ten hole nozzle is lower than for the eight hole nozzle. This results in a different opening pressure behavior,

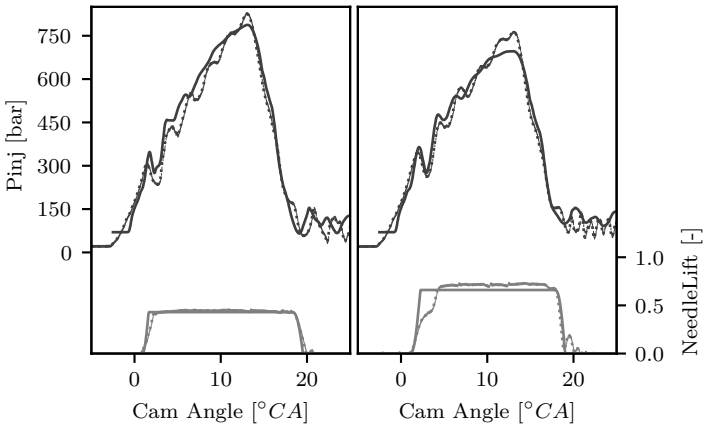

Figure C.7: Amesim results (solid line) compared to measurements (dotted line): needle lift (green) and injection pressure (orange). The ten hole nozzle is shown on the left and eight hole on the right plot.

although the rest of the injector assembly is the same. For the eight hole nozzle, there is a disagreement for the initial needle lift which likely is caused by the internals of the nozzle: the needle is shaped in several stages that lift the needle. For the ten hole nozzle all these stages are connected immediately with the injection pressure and contribute to needle lift. However, for the eight hole nozzle it is suspected that an additional stage only connects to the injection pressure after an initial lift which would explain the stepped needle lift. This was not implemented in the simulation model because these internal dimensions of the nozzle could currently not be measured more accurately and because the influence on sac pressure is rather limited, as can be seen from fig. C.8. Here, the sac pressure from the two nozzles is compared and even with different nozzles no real pressure difference can be seen during the lifting phase (0 until $5°CA$). An influence on spray penetration is however found in the spray measurements (see Chapter 4), indicating that the simulation code does not capture the sac pressure perfectly during the needle lift phase for the eight hole nozzle.

Only nozzle related parameter have been changed in the simulation model to replace the nozzle and the agreement between simulation and measurement for both nozzles is satisfactory which means that flow losses from the measurement location to the sac volume are reasonably well captured by the model.

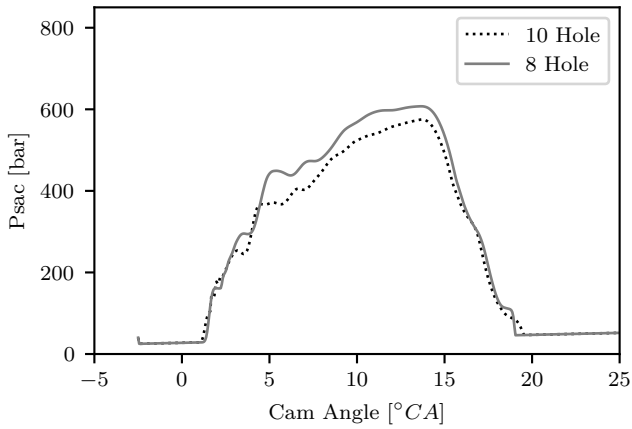

Figure C.8: Simulated sac pressure.

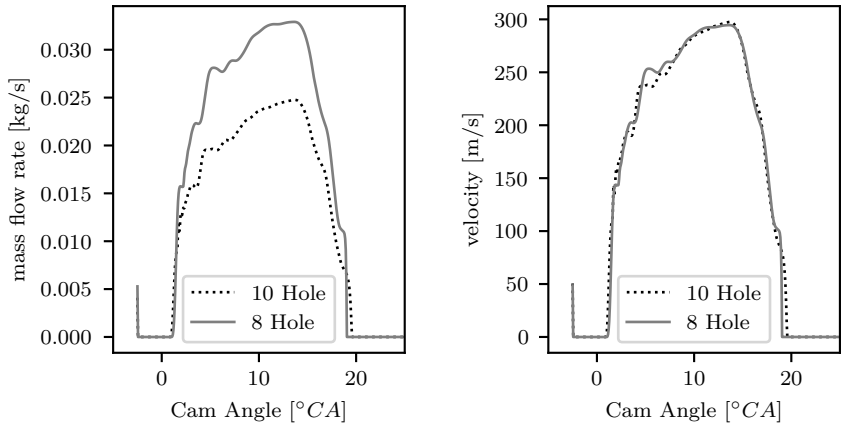

Figure C.9: Simulated mass flow rate and velocity for one hole of the eight (green) and ten (orange) hole nozzles.

C.3.4 Results

The mass flow rate for one nozzle hole is shown on the left hand side of fig. C.9 for the eight (green) and ten (orange) hole nozzle and the velocity is shown on the right. The injection velocity for the two nozzles is almost identical: this is influenced by three factors: the sac pressure, the total flow area and the area coefficient. The nozzles have been designed with a similar flow area to achieve equal peak injection pressures: the total flow areas of the ten and eight hole nozzle are respectively $1.134mm^2$ and $1.216mm^2$. The small difference in flow area is made up by a necessary change in the flow coefficient of the nozzle. This change was necessary in the simulation to come up with the correct peak pressure at the measurement location. The mass flow rate per nozzle hole differs more, but this is mainly caused by the amount of nozzle holes: the mass flow through one hole of the eight hole nozzle is higher than through one hole of the ten hole nozzle by a factor of approximately 10/8s. The total mass flow rate is shown in fig. C.10 and shows little difference between the two nozzles.

The sac pressure is shown in fig. C.8, the pressure for the eight hole nozzle is slightly higher than for the ten hole nozzle. This is remarkable, as the total flow area for the eight hole nozzle is bigger than for the ten hole nozzle. The discharge coefficient for the eight hole nozzle was set lower than for the ten hole nozzle, because of the peak injection pressure in the line. This results in a higher sac pressure for the eight hole nozzle.

Finally, it is interesting to see that using the Bernoulli flow rate from the

pressure measurement location to the nozzle hole gives quite good results for the mass flow rate when it can be calibrated with the total amount of injected mass. The discharge coefficient can be calculated by matching the simulated amount of fuel and the amount of fuel that results from integrating the mass flow rate by Bernoulli's law from start of needle lift until end of needle lift, based on the injection pressure measurement in the line.

A comparison for the ten hole nozzle is shown in fig. C.11. Some pressure waves are not captured perfectly and the peak mass flow rate is slightly overpredicted but this essentially means that when Bernoulli is applied when the needle is lifted, together with a calibrated C_d value, the mass flow rate as a function of time is quite well captured by this simple relation.

C.3.5 Zero wall shear velocity correction

In the investigated PLN injection system the initial line pressure is around $100bar$ and during every injection the line pressure goes up to $1000bar$: flow in the nozzle thus transitions quickly from non-cavitating to cavitating and as the discharge coefficient decreases when the flow chokes, the injection pressure goes up rapidly because the piston pump is still compressing fuel. This eventually results in a super cavitation regime which has a higher injection velocity than could be obtained by assuming a uniform injection velocity as is done in the output of the Amesim simulation code.

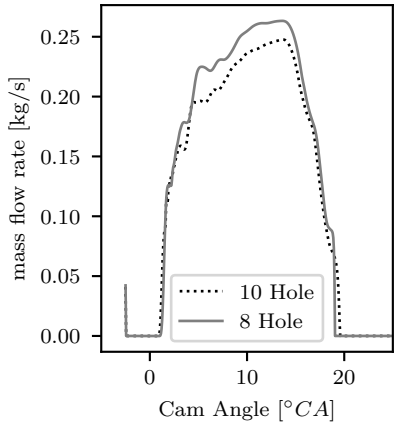

Figure C.10: Total mass flow rate for eight (green) and ten (orange) hole nozzles.

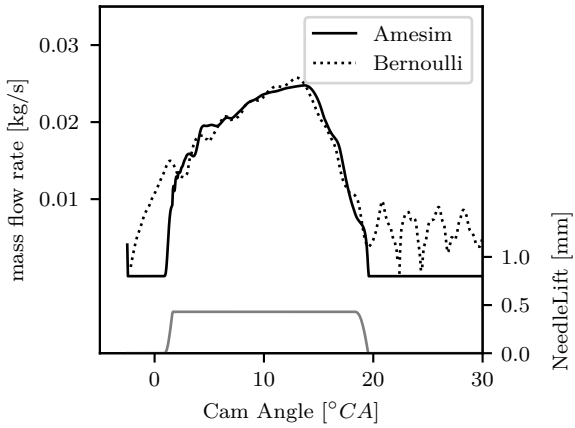

Figure C.11: Mass flow rate from the Amesim simulation compared to Bernoulli resulting from Bernoulli for the ten hole nozzle.

Additionally, in the Amesim simulation the discharge coefficient, C_d, is assumed to be constant during the injection. From Nurick's model, it is known that this is not the case in the nozzle holes. However, it is difficult to come up with the K_{crit} for this injection system. On the other hand, the range of the cavitation number in this injection system is limited because the range of injection pressures is rather small ($\sqrt{K} = [\sqrt{\frac{100}{100-50}}; \sqrt{\frac{400}{400-50}}] = [1.414; 1.068]$ which means that the discharge coefficient does not change much during the injection. This can be observed in measurements from other nozzles such as in fig. C.4: the C_d coefficient changes linearly, explained by eq. (C.7), but because the C_v starts to increase and C_A coefficient start to decrease they partially compensate each other. This means that C_A changes much more than the C_d coefficient when cavitation starts which shows the importance to correct for this coefficient.

This correction is done by neglecting the momentum transfer from the fluid to the wall as described in the previous section as 'zero wall shear', eq. (C.11). The start of cavitation is unknown for this injection system and can currently not be measured so a range of critical $\sqrt{K}$'s is investigated.

The correction is applied to the original uniform velocity from Amesim as follows:

$$v_{corr} = \frac{v_{uniform}}{C_A} \tag{C.12}$$

where C_A is calculated by eq. (C.11). The critical flow coefficient C_c in eq. (C.11) is calculated by applying Nurick's model for cavitating

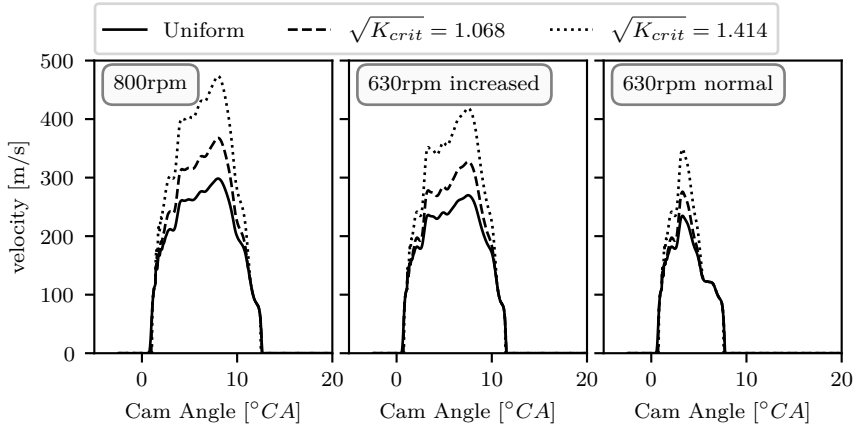

Figure C.12: Velocity correction applied to the velocity profile for different K_{crit}.

conditions (eq. (C.7)) and the injection pressure is taken as the sac pressure that resulted from the Amesim simulation.

The velocity resulting from the correction is shown in fig. C.12: a medium speed operating point ($800rpm$) is compared to a low speed operating point ($630rpm$). The low speed operating point is shown twice: once for a fuel injection setpoint that is similar to the medium speed operating point (higher than normal) and once with a normal low speed fuel injection setpoint.

When the nozzle is assumed to be relatively cavitation resistant ($\sqrt{K_{crit}} = 1.068$) the effect of this correction is already quite profound on the medium speed and low speed case with a higher fuel injection setpoint. Cavitation with this K_{crit} starts at $400bar$ and when the sac volume approaches this pressure, velocity starts to increase faster than expected from the uniform velocity assumption. When using a normal injection setpoint on the low speed case, the influence of this correction is limited which was expected from the lower sac pressure.

Even when the nozzle is assumed to be extremely sensitive for cavitation ($\sqrt{K_{crit}} = 1.4148$, or start of cavitation at $100bar$), the conclusion remains roughly same. For the medium speed case, the corrected velocity increases over the whole injection period while for the low speed case the velocity only increases significantly for a very brief period. This might not be realistic and the real cavitation number will likely lie in between these extremes.

References

[1] M. Allen, O. P. Dube, W. Solecki, F. Aragón–Durand, W. Cramer, S. Humphreys, M. Kainuma, J. Kala, N. Mahowald, Y. Mulugetta, R. Perez, M. Wairiu, K. Zickfeld. *Framing and Context.* In Global warming of 1.5°C. An IPCC Special Report on the impacts of global warming of 1.5°C above pre-industrial levels and related global greenhouse gas emission pathways, in the context of strengthening the global response to the threat of climate change. 2018.

[2] J. Rogelj, D. Shindell, K. Jiang, S. Fifita, P. Forster, V. Ginzburg, C. Handa, H. Kheshgi, S. Kobayashi, E. Kriegler, L. Mundaca, R. Séférian, M. V. Vilariño. *Mitigation Pathways Compatible with 1.5°C in the Context of Sustainable Development.* In Global warming of 1.5°C. An IPCC Special Report on the impacts of global warming of 1.5°C above pre-industrial levels and related global greenhouse gas emission pathways, in the context of strengthening the global response to the threat of climate change. 2018.

[3] IEA. *World Energy Outlook 2015.* Technical report, IEA, 2015.

[4] T. C. Bond, S. J. Doherty, D. W. Fahey, P. M. Forster, T. Berntsen, B. J. DeAngelo, M. G. Flanner, S. Ghan, B. Kärcher, D. Koch, S. Kinne, Y. Kondo, P. K. Quinn, M. C. Sarofim, M. G. Schultz, M. Schulz, C. Venkataraman, H. Zhang, S. Zhang, N. Bellouin, S. K. Guttikunda, P. K. Hopke, M. Z. Jacobson, J. W. Kaiser, Z. Klimont, U. Lohmann, J. P. Schwarz, D. Shindell, T. Storelvmo, S. G. Warren, C. S. Zender. *Bounding the role of black carbon in the climate system: A scientific assessment.* Journal of Geophysical Research: Atmospheres, 118(11):5380–5552, 2013.

[5] WHO Regional Office for Europe. *Evolution of WHO air quality guidelines: past, present and future.* Technical report, World Health Organization, Copenhagen, 2017.

[6] BP Energy Economics. *2018 BP Energy Outlook 2018 BP Energy Outlook.* Technical report, BP, 2018.

[7] EIA. *International Energy Outlook 2017 Overview.* U.S. Energy Information Administration, 2017.

[8] Statoil. *Long-term macro and market outlook 2017.* Technical report, Statoil, 2017.

[9] F. Rodríguez, O. Delgado, R. Muncrief. *Fuel consumption testing of tractor-trailers in the European Union and the United States.* The ICCT Briefing Paper, 2018.

[10] FOD Mobiliteit en Vervoer. *Kilometers afgelegd door Belgische voertuigen in het jaar 2017.* Technical report, FOD Mobiliteit en Vervoer, 2018.

[11] C. De Cauwer, M. Messagie, S. Heyvaert, T. Coosemans, J. Van Mierlo. *Electric vehicle use and energy consumption based on real world electric vehicle fleet trip and charge data its impact on existing EV research models.* World Electric Vehicle Journal, 7(3):436–446, 2015.

[12] D. J. MacKay. *Sustainable Energy — without the hot air.* UIT Cambridge Ltd., 2009.

[13] C. Bae, J. Kim. *Alternative fuels for internal combustion engines.* Proceedings of the Combustion Institute, 36(3):3389–3413, 2017.

[14] S. Verhelst, J. W. Turner, L. Sileghem, J. Vancoillie. *Methanol as a fuel for internal combustion engines.* Progress in Energy and Combustion Science, 70:43–88, 2019.

[15] EU Commission. *Regulation (EU) No 715/2007.* Official Journal of the European Union, 2007.

[16] EU Commission. *Regulation (EU) No 595/2009.* Official Journal of the European Union, 2009.

[17] EU Commission. *Regulation (EU) 2016/1628.* Official Journal of the European Union, 2016.

[18] S. P. S. Badwal, S. S. Giddey, C. Munnings, A. I. Bhatt, A. F. Hollenkamp. *Emerging electrochemical energy conversion and storage technologies.* Frontiers in Chemistry, 2:79, 2014.

[19] S. Badwal, S. Giddey, A. Kulkarni, J. Goel, S. Basu. *Direct ethanol fuel cells for transport and stationary applications – A comprehensive review.* Applied Energy, 145:80–103, 2015.

[20] J. E. Dec. *A conceptual model of DI diesel combustion based on laser sheet imaging.* SAE Technical Paper 970873, 1997.

[21] J. O'Connor, M. Musculus. *Post Injections for Soot Reduction in Diesel Engines: A Review of Current Understanding.* SAE International Journal of Engines, 6(1):400–421, 2013.

[22] J. E. Dec. *Advanced compression-ignition engines—understanding the in-cylinder processes.* Proceedings of the Combustion Institute, 32(2):2727–2742, 2009.

[23] M. Imperato, O. Kaario, T. Sarjovaara, M. Larmi. *Split fuel injection and Miller cycle in a large-bore engine.* Applied Energy, 162:289–297, 2016.

[24] R. Verschaeren, W. Schaepdryver, T. Serruys, M. Bastiaen, L. Vervaeke, S. Verhelst. *Experimental study of NOx reduction on a medium speed heavy duty diesel engine by the application of EGR (exhaust gas recirculation) and Miller timing.* Energy, 76:614–621, 2014.

[25] J. Benajes, S. Molina, R. Novella, E. Belarte. *Evaluation of massive exhaust gas recirculation and Miller cycle strategies for mixing-controlled low temperature combustion in a heavy duty diesel engine.* Energy, 71:355–366, 2014.

[26] MAN. *Project Guide: Electronically Controlled Two-Stroke Engines.* Technical report, MAN Diesel & Turbo, 2014.

[27] S. Brynolf, E. Fridell, K. Andersson. *Environmental assessment of marine fuels: liquefied natural gas, liquefied biogas, methanol and bio-methanol.* Journal of Cleaner Production, 74:86–95, 2014.

[28] G. A. Karim. *Combustion in Gas Fueled Compression: Ignition Engines of the Dual Fuel Type.* Journal of Engineering for Gas Turbines and Power, 125(3):827, 2003.

[29] Gamma-Technologies. *GT-Suite*, 2018.

[30] *Engine Combustion Network: https://ecn.sandia.gov/.*

[31] S. Saxena, I. D. Bedoya. *Fundamental phenomena affecting low temperature combustion and HCCI engines, high load limits and strategies for extending these limits.* Progress in Energy and Combustion Science, 39(5):457–488, 2013.

[32] F. Boecking. *Patent: Common rail fuel injector for internal combustion engines, as well as a fuel system and an internal combustion engine incorporating the injector*, 2004.

[33] F. J. Salvador, J. Martínez-López, M. Caballer, C. De Alfonso. *Study of the influence of the needle lift on the internal flow and cavitation phenomenon in diesel injector nozzles by CFD using RANS methods.* Energy Conversion and Management, 66:246–256, 2013.

[34] Y. Jung, J. Manin, S. Skeen, L. M. Pickett. *Measurement of Liquid and Vapor Penetration of Diesel Sprays with a Variation in Spreading Angle.* SAE Technical Paper 2015-01-0946, 2015.

[35] M. Blessing, G. König, C. Krüger, U. Michels, V. Schwarz. *Analysis of Flow and Cavitation Phenomena in Diesel Injection Nozzles and Its Effects on Spray and Mixture Formation.* SAE Technical Paper 2003-01-1358, 2003.

[36] E. J. Hayes Jr. *Patent: Piezoelectric controlled common rail injector with hydraulic amplification of piezoelectric stroke*, 1998.

[37] F. J. Salvador, A. H. Plazas, J. Gimeno, M. Carreres. *Complete modelling of a piezo actuator last-generation injector for diesel injection systems.* International Journal of Engine Research, 15(1):3–19, 2014.

[38] R. Ochoterena, P. Li. *Influence of cavitation on atomisation at low pressures using up-scaled and transparent nozzles.* In 23rd Annual ILASS-Europe Conference on Liquid Atomization and Spray Systems, 2010.

[39] A. Sou, R. H. Pratama, T. Tomisaka, Y. Kibayashi. *Cavitation Flow in Nozzle of Liquid Injector.* In International Conference on Liquid Atomization and Spray Systems (ICLASS 2012), 2012.

[40] W. H. Nurick. *Orifice Cavitation and Its Effect on Spray Mixing.* Journal of Fluids Engineering, 98(4):681, 1976.

[41] F. Payri, V. Bermúdez, R. Payri, F. J. Salvador. *The influence of cavitation on the internal flow and the spray characteristics in diesel injection nozzles.* Fuel, 83(4-5):419–431, 2004.

[42] S. Matlok, J. Hult, P. Simmank, S. Mayer. *Investigation of cavitation in injection nozzles for two-stroke Diesel engines.* In 28th CIMAC World Congress, 2016.

[43] D. L. Siebers. *Scaling Liquid-Phase Fuel Penetration in Diesel Sprays Based on Mixing-Limited Vaporization.* SAE Technical Paper 1999-01-0528, 1999.

[44] R. Payri, G. Bracho, P. Marti-Aldaravi, A. Viera. *Near Field Visualization of Diesel Spray for Different Nozzle Inclination Angles in Non-Vaporizing Conditions.* Atomization and Sprays, 27(3):251–267, 2017.

[45] R. Rotondi, G. Bella, C. Grimaldi, L. Postrioti. *Atomization of High-Pressure Diesel Spray: Experimental Validation of a New Breakup Model.* SAE Technical Paper 2001-01-1070, 2001.

[46] R. Payri, F. J. Salvador, J. Gimeno, J. de la Morena. *Study of cavitation phenomena based on a technique for visualizing bubbles in a liquid pressurized chamber.* International Journal of Heat and Fluid Flow, 30(4):768–777, 2009.

[47] J. D. Naber, D. L. Siebers. *Effects of Gas Density and Vaporization on Penetration and Dispersion of Diesel Sprays.* SAE Technical Paper 960034, 1996.

[48] F. Payri, R. Payri, F. J. Salvador, M. Bardi. *Effect of gas properties on Diesel spray penetration and spreading angle for the ECN injectors.* ICLASS 2012, 12th Triennial International Conference on Liquid Atomization and Spray Systems, pages 1–8, 2012.

[49] D. L. Siebers. *Liquid-Phase Fuel Penetration in Diesel Sprays.* SAE Technical Paper 980809, 1998.

[50] N. Maes, N. Dam, B. Somers, T. Lucchini, G. D'Errico, G. Hardy. *Experimental and Numerical Analyses of Liquid and Spray Penetration under Heavy-Duty Diesel Engine Conditions.* SAE International Journal of Fuels and Lubricants, 9(1):108–124, 2016.

[51] R. Payri, J. Gimeno, G. Bracho, D. Vaquerizo. *Study of liquid and vapor phase behavior on Diesel sprays for heavy duty engine nozzles.* Applied Thermal Engineering, 107:365–378, 2016.

[52] J. Gimeno, G. Bracho, P. Martí-Aldaraví, J. E. Peraza. *Experimental study of the injection conditions influence over n-dodecane and diesel sprays with two ECN single-hole nozzles. Part I: Inert atmosphere.* Energy Conversion and Management, 126:1146–1156, 2016.

[53] M. Arai, M. Tabata, H. Hiroyasu, M. Shimizu. *Disintegrating Process and Spray Characterization of Fuel Jet Injected by a Diesel Nozzle.* SAE Technical Paper 840275, 1984.

[54] M. P. B. Musculus, K. Kattke. *Entrainment Waves in Diesel Jets.* SAE International Journal of Engines, 2(1):1170–1193, 2009.

[55] S. Kook, L. M. Pickett, M. P. Musculus. *Influence of Diesel Injection Parameters on End-of-Injection Liquid Length Recession.* SAE International Journal of Engines, 2(1):1194–1210, 2009.

[56] M. P. B. Musculus, T. Lachaux, L. M. Pickett, C. A. Idicheria. *End-of-Injection Over-Mixing and Unburned Hydrocarbon Emissions in Low-Temperature-Combustion Diesel Engines.* SAE Technical Paper 2007-01-0907, 2007.

[57] L. M. Pickett, S. Kook, T. C. Williams. *Transient Liquid Penetration of Early-Injection Diesel Sprays.* SAE International Journal of Engines, 2(1):785–804, 2009.

[58] M. P. Musculus, P. C. Miles, L. M. Pickett. *Conceptual models for partially premixed low-temperature diesel combustion.* Progress in Energy and Combustion Science, 39(2-3):246–283, 2013.

[59] W. J. Pitz, C. J. Mueller. *Recent progress in the development of diesel surrogate fuels.* Progress in Energy and Combustion Science, 37(3):330–350, 2011.

[60] H. P. S. Shen, J. Steinberg, J. Vanderover, M. A. Oehlschlaeger. *A Shock tube study of the ignition of n-heptane, n-decane, n-dodecane, and n-tetradecane at elevated pressures.* Energy and Fuels, 23(5):2482–2489, 2009.

[61] K. Narayanaswamy, P. Pepiot, H. Pitsch. *A chemical mechanism for low to high temperature oxidation of n-dodecane as a component of transportation fuel surrogates.* Combustion and Flame, 161(4):866–884, 2014.

[62] Z. Luo, S. Som, S. M. Sarathy, M. Plomer, W. J. Pitz, D. E. Longman, T. Lu. *Development and validation of an n-dodecane skeletal mechanism for spray combustion applications.* Combustion Theory and Modelling, 18(2):187–203, 2014.

[63] G. Bruneaux. *Combustion structure of free and wall-impinging diesel jets by simultaneous laser-induced fluorescence of formaldehyde, poly-aromatic hydrocarbons, and hydroxides.* International Journal of Engine Research, 9(3):249–265, 2008.

[64] C. L. Genzale, R. D. Reitz, M. P. B. Musculus. *Effects of Piston Bowl Geometry on Mixture Development and Late-Injection Low-Temperature Combustion in a Heavy-Duty Diesel Engine.* SAE International Journal of Engines, 1(1):913–937, 2009.

[65] S. Moerman. *Onderzoek naar alternatieve brandstoffen : Ontwerp van een constant volume verbrandingskamer en studie van synthesegas.* Master's thesis, Ghent University, 2008.

[66] M. Lagast, J. Galle. *Ontwerp van de GUCCI-opstelling en studie naar het gebruik van biobrandstoffen.* Master's thesis, Ghent University, 2009.

[67] J. Galle. *Spray Atomization of Alternative Fuels in Medium Speed Diesel Engines.* PhD thesis, Ghent University, 2014.

[68] R. S. G. Baert, P. J. M. Frijters, B. Somers, C. C. M. Luijten, W. de Boer. *Design and Operation of a High Pressure, High Temperature Cell for HD Diesel Spray Diagnostics: Guidelines and Results.* SAE Technical Paper 2009-01-0649, 2009.

[69] K. Herrmann, B. V. Rotz, R. Schulz, G. Weisser, K. Boulouchos, B. Schneider, C. Winterthur, C. Zürich. *Reference Data Generation of Spray Characteristics in Relation to Large 2-Stroke Marine Diesel Engines Using a Novel Spray Combustion Chamber Concept Wärtsilä Switzerland Ltd , PO Box 414 ETH Zürich , Aerothermochemistry and Combustion Systems Laboratory.* Fluid Dynamics, (September):1–9, 2010.

[70] R. S. G. Baert. *Autoignition of Heavy Fuel Oil Sprays at High Pressures and Temperatures.* 112(July 1990), 2014.

[71] M. Meijer, J. Galle, L. Somers, J. Griensven, S. Verhelst. *High-Speed Characterization of ECN Spray A Using Various Diagnostic Techniques.* SAE International Journal of Engines, 6(2):1238–1248, 2013.

[72] A. Schmid, N. Yamada. *Spray Combustion Chamber: History and Future of a Unique Test Facility.* (September):6–8, 2017.

[73] A. Fedorov, R. Beichel, J. Kalpathy-Cramer, J. Finet, J. C. Fillion-Robin, S. Pujol, C. Bauer, D. Jennings, F. Fennessy, M. Sonka, J. Buatti, S. Aylward, J. V. Miller, S. Pieper, R. Kikinis. *3D Slicer as an image computing platform for the Quantitative Imaging Network.* Magnetic Resonance Imaging, 30(9):1323–1341, 2012.

[74] R. Benoot. *Ontwikkeling van een common rail brandstofinjectiesysteem voor een constant volume verbrandingskamer.* Master's thesis, Ghent University, 2016.

[75] C. Segaert, T. Pollet. *Realisatie van een common rail brandstofinjectiesysteem op een constant volume verbrandingskamer.* Vives Hogeschool, 2017.

[76] M. Meijer, B. Somers, J. Johnson, J. Naber, S.-Y. Lee, L. M. Malbec, G. Bruneaux, L. M. Pickett, M. Bardi, R. Payri, T. Bazyn. *Engine Combustion Network (Ecn): Characterization and Comparison of Boundary Conditions for Different Combustion Vessels.* Atomization and Sprays, 22(9):777–806, 2012.

[77] L. M. Pickett, D. L. Siebers, C. A. Idicheria. *Relationship between ignition processes and the lift-off length of diesel fuel jets.* SAE Technical Paper 2005-01-3843, 2005.

[78] B. Galmiche, F. Halter, F. Foucher, P. Dagaut. *Effects of dilution on laminar burning velocity of premixed methane/air flames.* Energy and Fuels, 25(3):948–954, 2011.

[79] R. Shang, Y. Zhang, M. Zhu, Z. Zhang, D. Zhang, G. Li. *Laminar flame speed of CO2 and N2 diluted H2/CO/air flames.* International Journal of Hydrogen Energy, 41(33):15056–15067, 2016.

[80] R. Fournet, J. C. Bauge, F. Battin-Leclerc. *Experimental and modeling of oxidation of acetylene, propyne, allene and 1,3-butadiene.* International Journal of Chemical Kinetics, 31(5):361–379, 1999.

[81] Z. Wang, H. Liu, R. D. Reitz. *Knocking combustion in spark-ignition engines.* Progress in Energy and Combustion Science, 61:78–112, 2017.

[82] T. D. Fansler, S. E. Parrish. *Spray measurement technology: A review.* Measurement Science and Technology, 26(1):012002, 2015.

[83] J. H. Gladstone, T. P. Dale. *Researches on the Refraction , Dispersion , and Sensitiveness of Liquids.* Philosophical Transactions of the Royal Society of London, 12(1863):317–453, 1863.

[84] J. Benajes, R. Payri, M. Bardi, P. Martí-Aldaraví. *Experimental characterization of diesel ignition and lift-off length using a single-hole ECN injector.* Applied Thermal Engineering, 58(1-2):554–563, 2013.

[85] L. M. Pickett, S. Kook, T. C. Williams. *Visualization of Diesel Spray Penetration, Cool-Flame, Ignition, High-Temperature Combustion, and Soot Formation Using High-Speed Imaging.* SAE International Journal of Engines, 2(1):439–459, 2009.

[86] A. Montanaro, M. Migliaccio, L. Allocca, V. Fraioli. *Schlieren and Mie Scattering Visualization for Single-Hole Diesel Injector under Vaporizing Conditions with Numerical Validation.* SAE Technical Paper 2014-01-1406, 2014.

[87] L. M. Pickett, C. L. Genzale, J. Manin, L.-M. Malbec, L. Hermant. *Measurement Uncertainty of Liquid Penetration in Evaporating Diesel Sprays.* In ILASS Americas, volume 35, 2011.

[88] R. Ryser, T. Gerber, T. Dreier. *Soot particle sizing during high-pressure Diesel spray combustion via time-resolved laser-induced incandescence.* Combustion and Flame, 156(1):120–129, 2009.

[89] N. Otsu. *A threshold selection method from gray level histograms.* IEEE Trans. Systems, Man and Cybernetics, 9(1):62–66, 1979.

[90] R. Payri, F. Salvador, G. Bracho, A. Viera. *Differences between single and double-pass schlieren imaging on diesel vapor spray characteristics*. Applied Thermal Engineering, 125:220–231, 2017.

[91] L. M. Pickett, J. Manin, C. L. Genzale, D. L. Siebers, M. P. B. Musculus, C. A. Idicheria. *Relationship Between Diesel Fuel Spray Vapor Penetration/Dispersion and Local Fuel Mixture Fraction*. SAE International Journal of Engines, 4(1):764–799, 2011.

[92] R. Payri, J. M. García-Oliver, T. Xuan, M. Bardi. *A study on diesel spray tip penetration and radial expansion under reacting conditions*. Applied Thermal Engineering, 90:619–629, 2015.

[93] R. Payri, F. J. Salvador, J. Gimeno, J. E. Peraza. *Experimental study of the injection conditions influence over n-dodecane and diesel sprays with two ECN single-hole nozzles. Part II: Reactive atmosphere*. Energy Conversion and Management, 126:1157–1167, 2016.

[94] L. M. Peter, L. M. Pickett, S. Kook, H. Persson, Ö. Andersson. *Diesel Spray Ignition Detection and Spatial / Temporal Correction*. SAE Int. J. Engines, 5(3):1330–1346, 2012.

[95] B. L. Smith, L. S. Ott, T. J. Bruno. *Composition-explicit distillation curves of diesel fuel with glycol ether and glycol ester oxygenates: Fuel analysis metrology to enable decreased particulate emissions*. Environmental Science and Technology, 42(20):7682–7689, 2008.

[96] Siemens PLM software. *Simcenter Amesim 16*, 2018.

[97] D. P. Schmidt. *Cavitation in Diesel Fuel Injector Nozzles*. PhD thesis, University of Wisconsin - Madison, 1997.

[98] R. Payri, F. J. Salvador, J. Gimeno, G. Bracho. *A new methodology for correcting the signal cumulative phenomenon on injection rate measurements*. Experimental Techniques, 32(1):46–49, 2008.

[99] A. Doudou. *Turbulent flow study of an isothermal diesel spray injected by a common rail system*. Fuel, 84(2-3):287–298, 2005.

[100] G. Ma, X. Tauzia, A. Maiboom. *One-dimensional combustion model with detailed chemistry for transient diesel sprays*. Proceedings of the Institution of Mechanical Engineers, Part D: Journal of Automobile Engineering, 228(4):457–476, 2014.

[101] B. J. McBride, S. Gordon, M. Reno. *Coefficients for Calculating Thermodynamic and Transport Properties of Individual Species*. Nasa Technical Memorandum, 4513(NASA-TM-4513):98, 1993.

[102] S. Bruce. *Best practice for pumping flammable gas mixtures outside the flammable gas range.* World Pumps, 2005(464):30–33, 2005.

[103] K. Lee, M. Yoon, M. Sunwoo. *A study on pegging methods for noisy cylinder pressure signal.* Control Engineering Practice, 16(8):922–929, 2008.

[104] D. Jung, D. N. Assanis. *Multi-Zone DI Diesel Spray Combustion Model for Cycle Simulation Studies of Engine Performance and Emissions.* SAE Technical Paper 2001-01-1246, 2001.

[105] J. Livengood, P. Wu. *Correlation of autoignition phenomena in internal combustion engines and rapid compression machines.* Symposium (International) on Combustion, 5(1):347–356, 1955.

[106] J. M. Desantes, J. J. López, M. Carreres, D. López-Pintor. *Characterization and prediction of the discharge coefficient of non-cavitating diesel injection nozzles.* Fuel, 184:371–381, 2016.

[107] S. Defruyt, C. Van de Maele. *A study of the atomization of biofuels in medium-speed diesel engines.* Master's thesis, Ghent University, 2012.

[108] J. M. Desantes, R. Payri, F. J. Salvador, J. Gimeno. *Measurements of spray momentum for the study of cavitation in diesel injection nozzles.* SAE Technical Paper 2003-01-0703, 2003.

[109] A. Sou, S. Hosokawa, A. Tomiyama. *Effects of cavitation in a nozzle on liquid jet atomization.* International Journal of Heat and Mass Transfer, 50(17-18):3575–3582, 2007.

[110] R. D. Reitz, F. B. Bracco. *On the Dependence of Spray Angle and Other Spray Parameters on Nozzle Design and Operating Conditions.* SAE Technical Paper 790494, 1979.

[111] W. Bosch. *The Fuel Rate Indicator: A New Measuring Instrument For Display of the Characteristics of Individual Injection.* SAE Technical Paper 660749, 1966.

[112] M. Marcic. *Sensor for injection rate measurements.* Sensors, 6(10):1367–1382, 2006.

[113] R. Payri, J. M. García, F. J. Salvador, J. Gimeno. *Using spray momentum flux measurements to understand the influence of diesel nozzle geometry on spray characteristics.* Fuel, 84(5):551–561, 2005.

[114] F. Payri, R. Payri, F. J. Salvador, J. Martínez-López. *A contribution to the understanding of cavitation effects in Diesel injector nozzles through a combined experimental and computational investigation.* Computers and Fluids, 58:88–101, 2012.

[115] N. De Kerpel, K. Vermeyen. *Optimizing the pilot injection of a medium speed dual fuel engine to achieve future emission standards.* Master's thesis, Ghent University, 2016.

[116] A. J. De Santis, T. Moerman. *Development of an injection system model for the optimization of a dual fuel engine.* Master's thesis, Ghent University, 2017.

[117] M. E. Tat, J. H. Van Gerpen. *Speed of Sound and Isentropic Bulk Modulus of Alkyl Monoesters at Elevated Temperatures and Pressures.* JAOCS, Journal of the American Oil Chemists' Society, 80(12):1249–1256, 2003.

[118] D. R. Caudwell, J. P. M. Trusler, V. Vesovic, W. A. Wakeham. *The Viscosity and Density of n-Dodecane and n-Octadecane at Pressures up to 200MPa and Temperatures up to 473 K.* International Journal of Thermophysics, 25(5):1339–1352, 2004.